

On patient-specific wall stress analysis in abdominal aortic aneurysms

Citation for published version (APA):

Putter, de, S. (2006). *On patient-specific wall stress analysis in abdominal aortic aneurysms*. [Phd Thesis 1 (Research TU/e / Graduation TU/e), Biomedical Engineering]. Technische Universiteit Eindhoven.
<https://doi.org/10.6100/IR606961>

DOI:

[10.6100/IR606961](https://doi.org/10.6100/IR606961)

Document status and date:

Published: 01/01/2006

Document Version:

Publisher's PDF, also known as Version of Record (includes final page, issue and volume numbers)

Please check the document version of this publication:

- A submitted manuscript is the version of the article upon submission and before peer-review. There can be important differences between the submitted version and the official published version of record. People interested in the research are advised to contact the author for the final version of the publication, or visit the DOI to the publisher's website.
- The final author version and the galley proof are versions of the publication after peer review.
- The final published version features the final layout of the paper including the volume, issue and page numbers.

[Link to publication](#)

General rights

Copyright and moral rights for the publications made accessible in the public portal are retained by the authors and/or other copyright owners and it is a condition of accessing publications that users recognise and abide by the legal requirements associated with these rights.

- Users may download and print one copy of any publication from the public portal for the purpose of private study or research.
- You may not further distribute the material or use it for any profit-making activity or commercial gain
- You may freely distribute the URL identifying the publication in the public portal.

If the publication is distributed under the terms of Article 25fa of the Dutch Copyright Act, indicated by the "Taverne" license above, please follow below link for the End User Agreement:

www.tue.nl/taverne

Take down policy

If you believe that this document breaches copyright please contact us at:

openaccess@tue.nl

providing details and we will investigate your claim.

On patient-specific wall stress
analysis in
abdominal aortic aneurysms

A catalogue record is available from the library of the Eindhoven University of Technology.

ISBN-10: 90-386-2578-2

ISBN-13: 978-90-386-2578-2

Printed by Febodruk BV, Enschede.

This research was performed in the scope of the Hemodyn project, a cooperation between Philips Medical Systems (Healthcare IT - Advanced Development), Best, the Technische Universiteit Eindhoven (Biomedical Engineering department), Eindhoven and the Erasmus University (Thoraxcenter, Biomedical Engineering), Rotterdam, The Netherlands. The Hemodyn project is partly funded by SenterNovem (Dutch Ministry of Economic Affairs).

Financial support for the publication of this thesis was kindly provided by Philips Medical Systems Nederland B.V. (Healthcare IT - Advanced Development).

On patient-specific wall stress analysis in abdominal aortic aneurysms

PROEFSCHRIFT

ter verkrijging van de graad van doctor aan de
Technische Universiteit Eindhoven, op gezag van de
Rector Magnificus, prof.dr.ir. C.J. van Duijn, voor een
commissie aangewezen door het College voor
Promoties in het openbaar te verdedigen
op woensdag 19 april 2006 om 16.00 uur

door

Sander de Putter

geboren te Velden

Dit proefschrift is goedgekeurd door de promotoren:

prof.dr.ir. F.A. Gerritsen

en

prof.dr.ir. F.N. van de Vosse

Copromotor:

dr.ir. M. Breeuwer

Contents

| | | |
|----------|--|-----------|
| 1 | Introduction | 1 |
| 1.1 | Abdominal aortic aneurysm | 1 |
| 1.2 | Imaging | 3 |
| 1.3 | Image segmentation | 5 |
| 1.4 | Computational models | 6 |
| 1.5 | Motivation and outline | 7 |
| | | |
| 2 | Automatic segmentation and tracking of abdominal aortic aneurysm from MR with 3D active objects | 9 |
| 2.1 | Introduction | 10 |
| 2.2 | Materials and methods | 12 |
| 2.3 | Validation procedure | 16 |
| 2.4 | Results | 19 |
| 2.5 | Discussion | 23 |
| 2.6 | Conclusions | 26 |
| | | |
| 3 | Image-based mesh generation with deformable surfaces | 27 |
| 3.1 | Introduction | 27 |
| 3.2 | Materials and methods | 29 |
| 3.3 | Results | 39 |
| 3.4 | Discussion | 42 |
| | | |
| 4 | Patient-specific initial wall stress in abdominal aortic aneurysms with a backward incremental method | 47 |
| 4.1 | Introduction | 47 |
| 4.2 | Methods | 49 |
| 4.3 | Results | 56 |
| 4.4 | Discussion | 58 |

| | |
|---|------------|
| 5 Sensitivity of peak wall stress in abdominal aortic aneurysm to geometrical variations | 61 |
| 5.1 Introduction | 62 |
| 5.2 Methods | 63 |
| 5.3 Results | 74 |
| 5.4 Discussion and Conclusions | 83 |
| 6 Models for local wall stress analysis in the calcified abdominal aortic aneurysm wall | 89 |
| 6.1 Introduction | 90 |
| 6.2 Materials and methods | 91 |
| 6.3 Results | 96 |
| 6.4 Discussion | 102 |
| 6.5 Conclusion | 104 |
| 7 Summary and discussion | 105 |
| 7.1 Summary | 105 |
| 7.2 Possible improvements | 106 |
| 7.3 Future prospects | 108 |
| Bibliography | 111 |
| Summary (in Dutch) | 121 |
| Samenvatting | 121 |
| Acknowledgements (in Dutch) | 125 |
| Dankwoord | 125 |
| Curriculum vitae | 127 |

CHAPTER 1

Introduction

Computational simulations of blood flow and vessel wall mechanics for vascular structures are currently mainly used as a research tool to study vascular diseases. In the near future, however, these methods may find their way into hospitals and clinics to aid the medical experts with deciding when to intervene, with planning the surgical procedure and with predicting the outcome of the procedure. The application area in this thesis is abdominal aortic aneurysm (AAA). The main focus is the patient-specific modelling of the wall mechanics of these pathologies. This introductory chapter provides an overview of the relevant background information on the nature of AAAs, their development, intervention criteria and the currently available methods for treatment. Also, a brief discussion of the available literature on image processing and wall mechanics modelling for AAAs is presented. In the concluding section of this chapter, a more detailed motivation and outline is provided.

1.1 Abdominal aortic aneurysm

An AAA is a dilatation of the human abdominal aorta situated between the branching with the renal arteries (leading to the kidneys) and the bifurcation to the iliac arteries (leading into the legs). Figure 1.1 shows a schematic overview of the structure of an AAA. In many AAAs, part of the aneurysm sac is filled with clotted blood, called the *thrombus*. The part of the aneurysm available for blood flow is called the aneurysm *lumen*.

The aorta is classified as aneurysmal if the diameter is approximately two times the normal aorta diameter of 15 mm. In a population based study of 6.386 men and women aged from 25 to 84 years the prevalence of the disease among men was estimated at 9%, while the estimated prevalence among women in the same age group was only 2% [99]. The main risk associated with AAA is that of a rupture, which leads to death before reaching the operating theatre in 75% of the cases [116]. For the remaining 25% of rupture cases, about half of the patients die during or shortly after surgery [6]. The disease mainly occurs in older people and rupture seldom occurs before the age of 65 [116]. In the last decades, the incidence has been

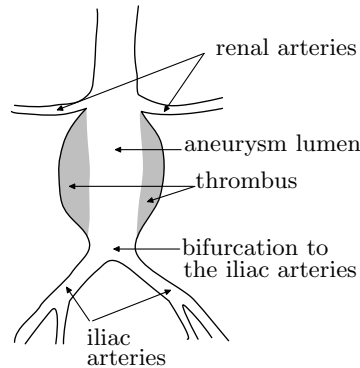


Figure 1.1: *Schematic overview of an abdominal aortic aneurysm.*

increasing at a rate that is higher than can be explained solely by the aging of the population [116].

The exact mechanism of AAA formation is not fully understood. Influences that play a role in the pathogenesis are degradation of the extracellular matrix, inflammation of the vessel wall, wall stress distribution, and genetic influences [9, 92]. Recognised risk factors for development and progression of AAA are its size, abnormal growth rates of the aneurysm, hypertension, smoking, chronic pulmonary disease and familial AAA [92, 116]. The patient-specific blood flow, and especially the wall shear stress on the vessel wall is believed to have a significant influence on the remodelling of the vessel wall and specifically on the size of the AAA [76, 103]. The wall of the AAA is often heterogeneous with lipid, fibrous and calcified regions [4, 111]. Aneurysm progression is highly variable. The majority of the aneurysms grow in a discontinuous way, with distinct periods without significant growth and periods with stronger growth [60].

Since AAA is usually an asymptomatic disease, detection happens mostly by chance [56]. Treatment of AAAs is performed through the placement of a stent-graft which acts to relieve the AAA wall of the systemic pressure. The placement of the stent-graft is either performed through open surgery, or via endovascular AAA repair (EVAR). With EVAR, a stent-graft is delivered to the AAA via a guide wire which is inserted through the femoral artery. The first successful EVAR procedure has been reported by Parodi et al. [82] in 1991. Because of the limited surgical trauma, the mortality rates with EVAR are much lower than with open surgery [42, 89]. However, EVAR may have some long term complications. Endoleak, which means incomplete occlusion of the aneurysmal sac, may be caused by leakage at the connection of the stent-graft with the vessel wall but also by non-ligated branch vessels, which may continue to put systemic pressure onto the aneurysmal sac [3]. Initial endoleak does, however, not significantly predict lack of sack regression [89]. Other reported complications are stent migration, limb thrombosis and even

AAA rupture [7]. These complications cause some surgeons to favour open surgery especially for younger, otherwise healthy patients. Because of the complications with EVAR, follow-up scans are usually performed every three to six months for the remainder of the patient's life [34].

Because of the mortality and other risks associated with both intervention procedures the selection of patients for surgery is critical. Performing surgery on patients who do not run a serious risk of a rupture may cost lives, as does withholding treatment from patients for whom there is a significant rupture risk. Straightforward rupture risk predictors include the ratio of length and diameter, the blood pressure, and the aneurysm expansion rate [48]. Still, the current intervention criterion is only based on the maximum diameter and the growth rate of the aneurysm. If the maximum aneurysm diameter at detection exceeds a preset threshold, usually 55 mm, the patient is scheduled for repair. Otherwise, the patient is followed with ultrasound imaging to monitor the progression of the AAA until the maximum transverse diameter has grown above this threshold, or until the growth rate increases to a value above a certain threshold [65, 127]. Change of AAA volume is an important factor in assessing rupture risk after endovascular repair [59, 126, 131].

1.2 Imaging

Currently, the main objectives of medical imaging of AAAs are monitoring, surgical planning and EVAR follow-up. For these purposes, visualisation of the aneurysm lumen, outer wall contours, calcifications and endoleaks are the main issues. For analysis of wall stress and hemodynamics, an ideal data set of images would also include information on the local wall thickness, the local wall composition, the detailed structure of the thrombus and the flow at several locations in the aneurysm. Not all of this information can, however, currently be acquired with standard clinical patient scanners.

Conventional freehand ultrasound imaging is a common imaging modality for AAA because of its use in monitoring. Its use is, however, limited for very obese patients and for patients with excessive bowel gas [127]. Intravascular ultrasound (IVUS) is currently the only modality which can provide some detail of the patient-specific AAA wall composition. Also, it is the best modality for detecting subtle endoleaks [127]. The main drawback of IVUS is its invasive nature, which makes this modality less attractive in clinical practice.

The most common imaging modality for surgical planning and EVAR follow-up is computed tomography angiography (CTA) [7]. The main advantages of CTA are the wide availability, the high resolution, the limited scan time and the excellent contrast between the vessel lumen and soft tissues. However, the contrast between thrombus and surrounding structures is very limited and the detailed structure of the thrombus cannot be visualised with CT. Not all serious endoleaks are visible on CT [3]. The greatest disadvantage is the ionising radiation, which limits the use for screening purposes. Furthermore, cardiac triggered CT is not yet widely

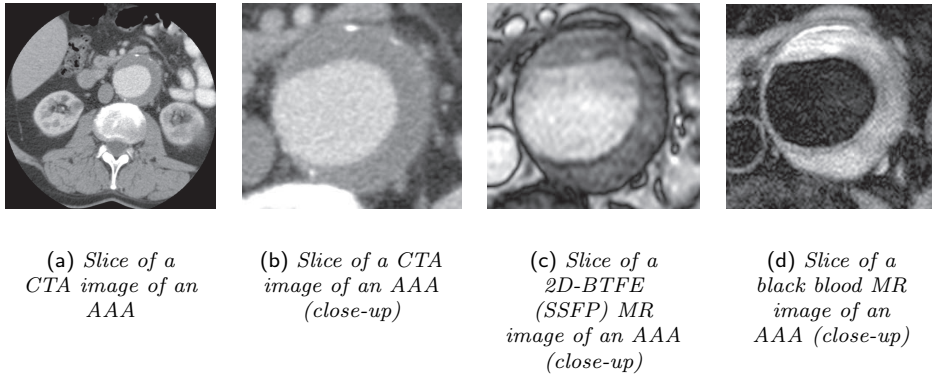


Figure 1.2: CTA and non-contrast enhanced MR images of abdominal aortic aneurysm. CTA gives very good contrast for the AAA lumen and has superior resolution. MR offers a better visualisation of the outer vessel wall and it provides better contrast for the different structures inside the thrombus.

available, so that dynamic or gated imaging is not yet possible on a large scale. Hall et al. [44] have performed wall thickness measurements on CT, but they did not show combined images of the wall and the measurements. In general, accurate local wall thickness reconstruction from CT is still very difficult, if not impossible. An example of a typical CT image of AAA is depicted in figures 1.2(a) and 1.2(b).

Magnetic resonance angiography (MRA) is less common for surgical planning and follow-up than CTA, mainly because of the poor visibility of calcifications and because of the common presence of ferromagnetic materials in endografts [127]. However, it has been reported that MR provides better information for follow-up than CT [33]. The flow sensitivity of magnetic resonance imaging makes it possible to measure blood flow and to visualise the lumen without the use of contrast agents with the steady state free precession (SSFP) protocol, as is shown in figure 1.2(c). Black blood imaging methods may be used to visualise the composition of the thrombus, plaques and fibrous caps [58]. Figure 1.2(d) shows an example of a black blood image in which several regions with different intensity can be distinguished within the thrombus. The same techniques have been used for wall thickness measurements in other parts of the body [61]. However, for AAA accurate reconstruction of the wall thickness with black blood techniques is not yet feasible. The required slice thickness for this protocol is large and the AAA wall is generally not perpendicular to the imaging plane, resulting in an overestimation of the wall thickness. Kramer et al. [58] used 7 mm thick slices, and in our own studies we used 6 mm thick slices. Furthermore, there is very little contrast between the thrombotic sediments and the vessel wall, as can also be observed in figure 1.2(d).

Some disadvantages of MR imaging, such as the contrast differences caused by RF field inhomogeneities and the limited coverage of the receiver coils have been at least partly resolved by some manufacturers in the past few years. The resolution may improve in future with the introduction of a new generation of higher field strength scanners, which may provide a better signal-to-noise ratio, at the possible cost of increased artifacts and less contrast [35].

1.3 Image segmentation

The majority of segmentation methods for AAA described in literature aim at segmentation of the vessel lumen and the outer wall of the aneurysm and are based on CTA. Segmentation of the AAA lumen in CTA images is fairly easy because of the use of contrast agent, leading to high contrast between the vessel lumen and the surrounding tissue. Segmentation of the outer vessel wall is more challenging because of the limited contrast with surrounding anatomical structures.

A large contribution concerning CTA based segmentation methods for the AAA outer wall has been made by de Bruijne, who has dedicated her PhD work to this subject [16]. The approach followed in her PhD work is to optimise the 2D active shape and appearance modelling method [15] for AAA segmentation. The optimisation is achieved by using slice similarity, a dedicated active appearance model for tubular structures, a non-linear appearance model and user interaction [17, 19, 20, 21]. De Bruijne also worked on segmentation of AAA from MR images [18]. The accuracies reported for this method are good. The main disadvantages of this approach for wall stress modelling are that the method is based on a time-consuming training with expert contours and that the model is still based on a set of 2D geometrical primitives and not on a true surface description, implying that further processing steps will be necessary to come to a finite element mesh, which is a prerequisite for the simulations.

Another approach used for segmentation of AAA in CTA images is based on the combination of deformable surfaces [25] and the level set method [80]. The accuracy and robustness of the implementation of this approach by Subasic et al. [104] is not good enough for employment in a clinical environment. Magee et al. [68] have also followed this approach and they report very high accuracies. However, the methods used for the validation remain unclear. The extension of deformable surfaces with level sets appears to be aimed at segmenting fine details such as small branching vessels. However, for AAA wall stress modelling, these details are currently not a major concern.

The segmentation method for the vessel wall location on CTA proposed by Olabariaga et al. [79] is also based on 3D deformable surfaces. In this work the training approach and the segmentation method with the non-linear appearance model from [16] have been used as an external force for a deformable surface. The accuracy that is achieved with this method is comparable to that of de Bruijne. The full 3D nature of this approach makes it an attractive method for AAA modelling for finite element applications.

1.4 Computational models

The mechanical argument that correlates the maximum aneurysm diameter with the maximum wall stress is based on the law of Laplace [29, 55]. Hall et al. [44] have estimated the wall tension for AAA by application of Laplace's law. Even this simplified predictor, that does not take into account patient-specific material properties or measured dynamics, proved to be a predictor of AAA rupture. Elger et al. [32] used axisymmetric AAA models based on meridional curves to show that the shape of the AAA has a substantial influence on the local wall stress, implying that Laplace's law is too simple a predictor. Sacks et al. [91] used patient-specific models of AAA to derive the local principal curvatures and they concluded that an axisymmetric model is also incapable of capturing the shape variations relevant for the rupture prediction in AAA. The same conclusion was drawn by Vorp et al. [123] who investigated the influence of asymmetry on the computed wall stress. In another study [86] patient-specific shape models were build for six patients. The results indicated a complex wall stress distribution in comparison to the healthy aorta. Fillinger et al. [38] showed that the peak wall stress can outperform the maximum transverse diameter with an ROC analysis based on a study with 103 patients, 14 of whom experienced a rupture. Comparison of the simulated wall stress in ruptured and non-ruptured AAAs showed that the maximum stress in the ruptured AAAs was significantly higher than for the non-ruptured AAAs [120]. In this study, the authors also demonstrated a positive correlation between the site of maximum wall stress and the rupture site. Li and Kleinstreuer [63] have used simulation results to derive an empirical wall stress equation based on an extension of Laplace's law and they found good agreement. This approach may provide a way to circumvent lengthy patient-specific simulations. However, as mentioned by the authors, it cannot provide accurate predictions for seriously distorted geometries. Although these studies all indicate that wall stress is an important influence for AAA rupture risk prediction, the clinical significance of patient-specific wall stress has so far only been tested in a single study based on a limited number of patients.

The question of what is the correct approach for modelling the influence of intraluminal thrombus (ILT) is still controversial. Vorp et al. [124] suggested that ILT has an important influence on the weakening of the vessel wall because it hampers the oxygen diffusion to the vessel wall. The first mechanical studies into ILT were based on elastic ILT and lead to the conclusion that thrombus would reduce the

stress exerted on the AAA wall [26, 27, 74, 125]. However, experimental studies indicate that the full systemic pressure is transduced to the AAA wall, even in the presence of ILT [95]. Thubrikar et al. [110] showed that even though thrombus does not influence the pressure at the AAA wall, it may provide structural integrity to the AAA wall and decrease dilatations. Medical images and postmortem studies indicate that there are several kinds of thrombus, which may be visualised in-vivo with black blood MR. Presence and configuration of these thrombus constituents may vary largely between patients.

The importance of the local wall composition and thickness for the computed wall stress has been widely recognised. However, the current limitation of imaging techniques limit the patient-specific modelling of these variations in AAA to the modelling of the influence of calcifications [69, 100].

1.5 Motivation and outline

In current clinical practice, diagnosis and treatment for complex diseases of the vascular system highly depend on advanced 3D medical imaging techniques and analysis of the resulting images by radiologists. Algorithms for image analysis and computer aided diagnosis provide an important aid to the radiologists to cope with the vast amount of data and to relieve them of tedious, time-consuming tasks.

Computer simulations of hemodynamics and vessel wall mechanics in the human vascular system may be used to provide information that is not directly visible on medical images. With image registration, segmentation and quantification and computer aided diagnosis, the ground truth is often provided by the radiologist. For simulations based on medical images the performance evaluation is more complicated. The raw output of patient-specific simulations of complex blood flow patterns, wall motion and wall stress is difficult to interpret even for experts. Therefore, for clinical use of blood flow and wall mechanics simulations, derivation of relevant but simple, preferably even one-dimensional indices is essential.

The focus of this thesis is patient-specific finite element modelling of AAA. Although Fillinger et al. [38] have shown that patient-specific peak vessel wall stress may outperform the currently used maximum vessel diameter as an AAA rupture predictor, this method has not yet been introduced into the clinical practice. Apart from FDA approval, the main bottlenecks for clinical acceptance of this approach will probably be the level of automation, the speed and the accuracy and robustness of the method. Furthermore, the clinical sensitivity and specificity of this predictor can possibly be improved further by using more patient-specific input, such as local material properties, global compliance, initial wall stress and the influence of thrombotic sediments.

Patient-specific modelling of the wall mechanics requires reconstruction of the geometry from medical images, construction of a computational mesh and a model for simulating the wall stress resulting from the pressure load on the inner aneurysmal vessel wall. These three sequential steps are described in chapters 2-4. In the second

chapter a segmentation algorithm to reconstruct the dynamic AAA geometry from dedicated MR images is presented. In the third chapter the chain of algorithms leading from the segmentation result to the finite element mesh, which serves as input for the simulation, is described. In the fourth chapter a backward incremental method is introduced, which allows wall stress assessment in the systolic AAA based on the measured diastolic geometry. In the fifth chapter, the sensitivity of the model is evaluated both for MR and CT using several independent manual delineations of the vessel wall contours. In chapter six the influence of calcifications in the AAA vessel wall on the computed wall stress is investigated. Finally, the concluding chapter provides a summary of and a discussion on the results of the preceding chapters.

Automatic segmentation and tracking of abdominal aortic aneurysm from MR with 3D active objects

Abstract

The current criterion for surgical intervention for abdominal aortic aneurysms is based on the maximum transverse diameter of the aorta. Recent research indicates that a better rupture predictor may be derived from the wall stress. A major influence for the wall stress in the aneurysm is the patient-specific shape of the aneurysm. We have developed an automatic method to derive the dynamic patient-specific aneurysm geometry from 2D and 3D non contrast-enhanced MR steady-state free precession (SSFP) images. The individual slices of the 2D-scanned volumes are registered onto the 3D-scanned volumes via a normalised mutual information similarity measure to restore spatial coherence. The resulting images are anisotropically filtered to reduce the image noise and to enhance the specific image features used for the segmentation. The lumen and the outer wall boundary of the aneurysm are constructed from the end-diastolic 2D SSFP images by using 3D active objects (3DAO, also known as deformable surfaces). The resulting end-diastolic geometrical model is propagated over the remaining dynamic acquisitions by deforming with an external force based on the correlation between grey value profiles sampled at subsequent phases on the mesh nodes of the 3DAO. The resulting segmentations were evaluated with respect to manual image segmentations produced by three expert users for four patients. The resulting accuracy is shown to be comparable to the accuracy that is being reported in literature for CT and MR based methods.

2.1 Introduction

An abdominal aortic aneurysm (AAA) is a permanent dilation of the human aorta which is life-threatening due to the potential event of a rupture. In current clinical practice, surgical intervention is considered once the maximum transverse diameter exceeds 55 mm. It has been shown that other geometry related quantities such as aneurysmal volume, the ratio between diameter and length and the largest cross-sectional area can provide better rupture risk predictors [48].

Recent advances in research on AAA intervention criteria have focussed on finite element method (FEM) based wall stress simulations for AAA [28, 37, 38, 86, 120, 123]. The patient-specific shape of abdominal aortic aneurysms is one of the major influences on the stress in the vessel wall [32, 123]. Accurate patient-specific modelling of wall stress in AAA would require detailed input such as material properties and the precise configuration of thrombus and atherosclerotic plaques [27, 53, 95, 112, 125]. However, Fillinger et al. [38] have shown that even a simplified model with constant wall thickness and constant material properties significantly outperforms the maximum transverse diameter as an intervention criterion. For possible future large scale clinical use of a wall stress based rupture risk predictor automated methods to segment the medical images and obtain a patient-specific finite element mesh are important prerequisites.

With contrast enhanced CT the vessel lumen geometry, the calcified plaque and the outer vessel wall location may be visualised. With MR, the AAA lumen and thrombus can be visualised as well. Although large calcified plaques can sometimes be distinguished on MR images as signal voids, the visibility of these calcifications is worse than with CT. However, MR can provide additional important hemodynamical and mechanical information such as the patient-specific blood flow and the pulsating motion of the aneurysm. The MR images of AAA have a more limited spatial resolution, possibly some geometrical distortion, and less contrast between the lumen and the thrombus and the vessel wall in comparison with the CT images.

A number of automatic and semi-automatic segmentation methods for AAA from CTA have been reported in literature. Olabarriaga et al. [79] have used a deformable model in combination with a training via a k-nearest neighbours classification method. A similar classification method has been used by de Bruijne et al. [20, 21] in combination with a 2D statistical shape modelling approach. Another approach that has been followed for segmentation of AAA is the combination of deformable models and level sets [68, 104]. Imaging of AAA with MR is not yet a generally accepted routine in clinical practice. In [18] segmentation of AAA from MRA images was performed with a 2D statistical shape model with multi-spectral image features. Apart from this work, there is very little literature on segmentation of AAA from MR.

For our application it is essential to employ a segmentation method that leads to an object representation that allows robust and accurate translation to a finite element model. The main disadvantage of segmentation methods based on training is that they require large training sets and that the resulting algorithm may require

full retraining when adjustments in the imaging method are made. We do not yet have enough patient data with our novel MR acquisition method to allow for such an extensive training. The main disadvantages of the statistical shape modelling approach in [20, 21] is that this method is based on a set of 2D geometrical primitives and not on a true surface description like the deformable model, implying that further processing steps will be necessary to come to a finite element mesh, which is a prerequisite for the simulations. The 2-simplex based deformable model approach has some advantages for finite element applications since it allows control over smoothness and topology and it can be transformed to high quality surface triangulations quite easily [2]. The extension of deformable models with level set methods appears to be aimed at segmentation of fine details, which are not a major concern for our application, since these fine details cannot yet be taken into account in the wall stress simulations due to resolution limitations. For these reasons, the standard deformable model approach suits our needs best.

Comparison of segmentation results for medical images is a difficult task. A variety of different performance characterisation methods has been proposed and evaluated [57, 78]. Even for similar segmentation tasks different evaluation approaches are being followed to compute the performance and the exact method is not always presented, as may become clear from the following examples. The segmentation method proposed in [79] has been evaluated with respect to a single expert segmentation. The distance measure used in this work is the distance from the vertices of the 3DAO surface to a reconstructed triangular mesh based on the manual contours. However, the method used to reconstruct the mesh from the manual contours is not reported. In [18, 21] the in-slice root mean squared error between the manual segmentation and the automatic result is reported. In [104] the relative differences of the number of pixels included in the segmentation in each slice between automatic segmentation results and manually corrected semi-automatic segmentation results is reported. In [68] the automatic segmentation results are compared with interactive results by measuring the maximum differences for each data set. No information is provided on the distance measure that is used in this work.

In this chapter we present a method to reconstruct the dynamic lumen and vessel surface of the AAA from non contrast enhanced MRA images with 3D active objects (3DAO) [25, 24]. The method has been applied on data from six AAA patients. For four patients, the segmentation results have been validated by comparison with manual contours from three experts. The validation method that we used is the contour averaging method by [13] which assures transitivity between a number of similar contours and simultaneously supplies a golden standard contour for manual segmentations supplied by a number of users. Based on this method we have computed several common error measures, to allow for a broad comparison to the previous methods. For the remaining two patients, a visual inspection was performed. The results of the evaluation indicate that the accuracy of the automatic segmentations based on MRA is similar to the accuracies reported for segmentation of AAA from CTA.

2.2 Materials and methods

2.2.1 Imaging

2D balanced turbo field echo (B-TFE, steady state free precession protocol) [107] images have been acquired on a Philips Gyroscan Intera 1.5T MR scanner (Rel. 10.4) for six male AAA patients that were scheduled for surgery (age: min. 60, max. 77, av. 69, max. transverse diameter: min. 58 mm, max. 73 mm, av. 63 mm) for 25 slices and 12 cardiac phases (SENSE cardiac coil, TE/TR=2.14/4.28 ms, flip angle 50 degrees, FOV=300 mm, matrix scan 224, voxel dimensions $1.2 \times 1.2 \times 6 \text{ mm}^3$, slice gap 0 mm, no breath-holding, non contrast-enhanced). 3D B-TFE images were acquired with similar parameters for 50 slices with an overlap of 3 mm. For both these imaging protocols, there is considerable anisotropy in the image sampling. Patient motion (movement and respiration) may cause the slices in the 2D protocol to be dislocated with respect to each other. However, the 2D imaging protocol is more sensitive to flow and gives better contrast between the AAA lumen and thrombus than the 3D B-TFE protocol. However, since the whole volume of interest is acquired simultaneously in the 3D protocol, there is no dislocation between the slices.

2.2.2 Image registration

Between the acquisition of the 3D B-TFE and the 2D B-TFE images, the patient may have moved. Furthermore, the 2D B-TFE images are acquired slice by slice in an interleaved manner, which means that within a single volume these slices may also be slightly dislocated with respect to each other due to patient motion and respiration. For these reasons, it may be necessary to realign the images and the individual slices. This realignment is achieved with image registration techniques.

As a first step, we register the 2D and 3D B-TFE volumes by using a rigid body motion model (rotations and translations with respect to the three principal axes) using normalised mutual information as a similarity measure.

$$I(A, B) = \frac{H(A) + H(B)}{H(A, B)}, \quad (2.1)$$

with I the computed similarity between the two images, $H(\cdot)$ the Shannon-Wiener entropy and $H(\cdot, \cdot)$ the joint entropy of the two images [43].

The optimisation method for finding the optimal transformation is based on a steepest gradient descent method in the transformation parameter space. The optimisation is performed at three resolution levels for which every next level uses half the sampling step used in the previous level. The initial resolution in the registration process is 2 mm.

We have assumed that further transformations of the individual slices of the 2D B-TFE scan can be well described with an in-slice translation and a rotation around the patient's transversal axis. This approach should account for most of the dislocations resulting from small patient movements in the scanner. With this model

we registered the individual 2D B-TFE slices onto the 3D B-TFE volume, again with the normalised mutual similarity measure and a steepest gradient descent optimisation procedure, to further refine the registration. Reconstruction of the final registered image slices is then performed with an in-slice interpolation.

2.2.3 Segmentation initialisation

First, the 2D B-TFE images are locally anisotropically filtered, tangentially to edges with the method by Jago et al. [54], in order to reduce noise without affecting the edge location. To delineate the AAA region of interest, the user selects a point in the AAA lumen below the renal arteries and a second point above the bifurcation to the iliac arteries. Based on these user-defined points a wave-front propagation is performed on the in-slice gradient magnitude of the image intensity [130]. At every iteration step the voxels neighbouring the current wave front are added to the front and for each new voxel a cost is determined via

$$C = \begin{cases} C_o + 1, & i < s, \\ C_o + 1000, & i > s, \end{cases} \quad (2.2)$$

with C_o the cost in the voxel from which the new voxel was reached, i the image intensity at the new voxel and s a predefined threshold. When the end point is reached by the wave front, the lumen centreline is constructed by back tracing the minimal cost path of the wave front cost. From the centreline an initial 3DAO is created [25].

2.2.4 3D active objects model

A 3DAO is a collection of connected non-planar simplex faces in which every 3DAO simplex node has exactly three neighbour vertices. The surface can be iteratively deformed based on forces computed from the image features and shape regularisation forces. In the case of the AAA application, the initial 3DAO is a tubular object, centred around the lumen centreline. The new position for a node is determined at every iteration from the current position via a time-discretised second-order Newtonian-evolution equation

$$\mathbf{P}_i^{t+1} = \mathbf{P}_i^t + (1 - \gamma) (\mathbf{P}_i^t - \mathbf{P}_i^{t-1}) + \alpha \mathbf{F}_{int} + \beta \mathbf{F}_{ext}, \quad (2.3)$$

where \mathbf{P}_i^t denotes the position of the i -th simplex node at iteration t . With \mathbf{F}_{int} and \mathbf{F}_{ext} we denote the internal force (ensuring smoothness) and the external force (fitting the node to image features) respectively. The parameters α and β denote the respective weighting coefficients of these forces and γ is a damping coefficient used to stabilise the deformation process.

The internal forces we used for the segmentation are based on a regularisation approach that is aimed at making the estimated local surface curvature at a vertex equal to the curvatures of the three neighbouring vertices [24]. A more detailed description is provided in section 5.2.3. The image-based external forces are different for the lumen segmentation and the outer vessel wall boundary segmentation and will be presented in the next subsection.

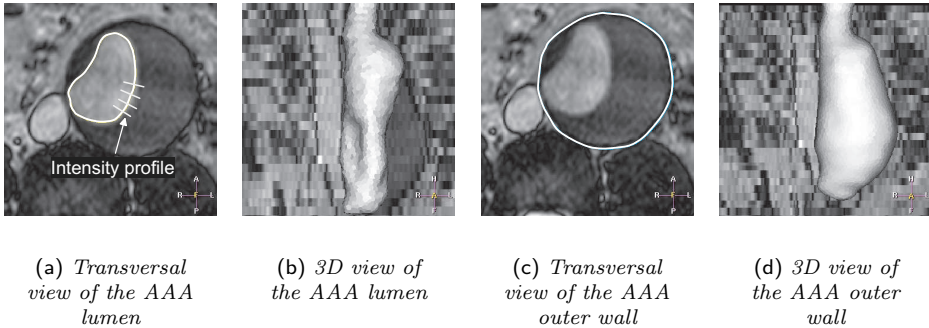


Figure 2.1: Segmentation results for aneurysm 1.

2.2.5 External force calculation procedure

The external forces for the segmentation procedure are computed by sampling inslice intensity profiles at simplex surface nodes in the feature images, perpendicular to the intersection contour between the image plane and the 3DAO surface, as depicted in figure 2.1(a). To account for the high anisotropy in the data, the external forces are only imposed on vertices that are within a user defined distance of an imaging plane. The position of the remaining nodes is determined by the internal forces only. For the segmentations presented in this chapter the distance criterion was set to 0.25 times the slice distance.

The segmentation of the AAA lumen is based on the gradient magnitude of the 2D B-TFE images, which is usually high at the outer contours of the lumen. First a threshold t is automatically derived from the histogram H of the 2D Gaussian gradient magnitude $L_w = \sqrt{L_x^2 + L_y^2}$ of the portion of the image within the interior of the initial 3DAO surface. The blurring factor τ for the Gaussian derivatives used to compute L_w was taken as three pixels. For all the segmentations in this chapter we used a value of $t = \overline{H} + 3\sigma$, where σ denotes the standard deviation in the histogram. At every iteration, intensity profiles with a total length of 6 mm are sampled, centred at the simplex nodes and the maximum gradient magnitude value on this profile is determined. If this maximum gradient magnitude on the sampled profile is higher than t , we deform towards the location of this maximum. Otherwise, the external force is set to move outwards with a constant weight.

For the segmentation of the outer wall of the AAA, we take advantage of the boundary effect at the outer vessel wall caused by an MR phenomenon called the chemical shift of the second kind [46], which leads to a local intensity dip (valley) at the location of the outer vessel wall. Segmentation of the vessel wall is based on this valley and on knowledge of the lumen intensity. Although unlike for CT, there are strong variations between patients in the intensity with which the thrombus appears on the 2D B-TFE images, we can use the assumption that the thrombus intensity

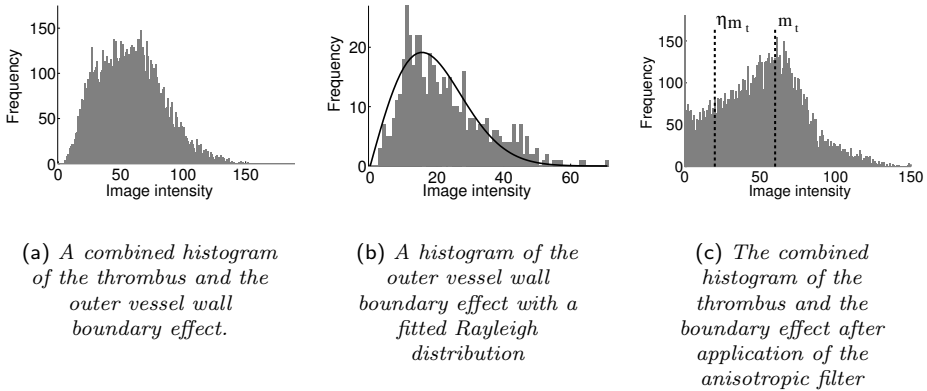


Figure 2.2: The effect of application of the anisotropic filter on the 2D B-TFE images for the outer AAA wall segmentation. Before the application of the filter, the grey values of thrombus and the boundary effect cannot be well distinguished (a). The grey value distribution of the outer wall boundary effect is well approximated by a Rayleigh distribution, indicating that this distribution is dominated by noise (b). The fit of the Rayleigh distribution in this middle figure is based on a least squares estimate for θ^2 . Application of the anisotropic filter diminishes this noise, causing the grey values corresponding to the valley to shift to the left. In figure (c) we have indicated the derivation method for the threshold used in the segmentation process.

is lower than the lumen intensity. Because of the image noise, the intensities of the valley feature can generally not be distinguished as a separate mode in the grey value histogram, as depicted in figure 2.2(a). The noise distribution for low intensity structures in MR images, such as the valley at the outer wall, is often approximated with a Rayleigh probability density function [1, 47] which reads

$$p(x) = \frac{x}{\theta^2} e^{-\frac{x^2}{2\theta^2}}. \quad (2.4)$$

Figure 2.2(b) shows a fit of a Rayleigh distribution on a typical histogram of the valley feature. The noise model fits the intensity distribution very well. After application of the anisotropic filter, the valleys in the image are deepened, resulting in a shift of these grey values in the histogram to the left, as depicted in figure 2.2(c). To obtain a patient-specific threshold during the segmentation process, we shoot outward intensity profiles with a length of 2 mm in every vertex of the lumen 3DAO to construct a new grey value histogram. A lower threshold t_l is derived by taking a fixed fraction of η times the grey value m_t , corresponding to the maximum of the histogram for the thrombus. For the segmentations we used a fixed value of $\eta = 0.3$. A higher threshold t_u is derived by taking the intensity level halfway between the mean lumen intensity and m_t .

For the calculation of the external forces, we sample intensity profiles of 40 mm

in the 2D B-TFE images, from which the minimum is used to deform towards the valley, and the maximum is used to prevent growing into the vena cava, which has a high intensity similar to that of the AAA lumen. To speed up the process and to avoid a vertex from moving past a previously detected incomplete feature, we shorten the sampling profiles at every iteration with respect to the distance to the last encountered positive feature. With this approach, the deformation process may halt before the 3DAO surface has reached the actual vessel wall location when vertices do not follow the shortest path to a feature. In our implementation this problem is overcome by automatically resetting the search depths at regular intervals of 20 iterations.

2.2.6 Propagation of the AAA geometry over time

The segmentation process described in subsections 2.2.3 - 2.2.5 is performed for the end-diastolic phase only. To propagate the resulting 3DAOs over the other cardiac phases, we use the correlation between in-slice intensity profiles at subsequent phases. First, the optimal position for a simplex node is determined once by optimising the correlation coefficient c_i between the two sampled profiles l_t and l_{t-1} of length n for this node when shifting one profile along the other one. The formula for a shift in the outward direction with i steps is given by

$$c_i = \frac{\sum_{j=0}^{n-i} (l_t(j) - \bar{l}_t) (l_{t-1}(j+i) - \bar{l}_{t-1})}{\sqrt{\sum_{j=0}^{n-i} (l_t(j) - \bar{l}_t)^2 \sum_{j=0}^{n-i} (l_{t-1}(j+i) - \bar{l}_{t-1})^2}}. \quad (2.5)$$

The formula for a shift in the opposite direction is similar, with the indices of l_t and l_{t-1} interchanged. Next, we iteratively deform the 3DAO to the computed optimal position by using the distance to this position as an external force for the 3DAO. Because the convolution domain in (2.5) is dependent on the shift i , the profile length must be long in relation to the computed shifts. For the experiments we used symmetric profiles with a total length of 10 mm. A similar approach based on 2D active contours has been followed for segmentation of MR cardiac images by Ranganath [88]. Our approach does not require adapting the dynamic segmentations to specific image features as is done in the approach of Gérard et al. [41].

2.3 Validation procedure

For the validation of the segmentation result, the automatically segmented surfaces were compared to manual segmentation contours for four patients. Three expert users were asked to draw closed polybezier curves on the 2D B-TFE images for the first four patients in our database, indicating the position of the vessel lumen and of the outer AAA wall. The selection criterion for the slices used for this validation procedure was that the slice should be located above the bifurcation of the aorta into the iliac arteries, and below the renal arteries.

The three observers were asked to draw the contours twice, in two separate sessions, resulting in six manual contours for the lumen and six manual contours for the vessel wall location on every selected slice. Since the manual contours have been drawn on the original image data, we transformed the contour coordinates with the transformations computed in the registration process.

2.3.1 Validation methodology

Since we only had two contours per user, we did not compute the intra-observer variability based on these four patients. Instead we put the six manual contours in a single validation set and computed the performance of the algorithm with respect to the average and the variability within this validation set. In order to provide a broad overview of the performance of our segmentation scheme, we have computed the segmentation accuracy both in 3D and for the separate image slices employing the contour averaging method and the 3D distance between the point cloud of the discretised expert contours and the 3DAO surface. This last measure allows through plane distance estimates as is the case in the work by Olabbarriaga et al. [79]. We have applied and evaluated the propagation algorithm for all four patients, even though only two of the four AAAs showed a large amount of motion over the cardiac cycle. However, even when there is only limited motion, the grey profile matching is still influenced by noise and artifacts which may cause the grey value appearance in the region of interest to vary on the images for different cardiac phases. Therefore, it is still useful to apply the algorithm for these patients to evaluate the performance and to establish that the algorithm can be applied without having to preselect the data.

2.3.2 Measuring the distance to a 3DAO surface

The vertices of the simplices forming the 3DAO surface are not required to be positioned within the same 2D plane. Therefore, the distance of a point \mathbf{x} in 3D to a 3DAO surface \mathcal{S} can only be defined by assuming a model for the geometry of the 3DAO's faces. For the computation of this distance the approximation depicted in figure 2.3 has been employed. First, we find the mesh node closest to \mathbf{x} , which shall be denoted by $\tilde{\mathbf{v}}$. Let \mathbf{v}_i , $1 \leq i \leq 3$ denote the three neighbouring vertices of $\tilde{\mathbf{v}}$. With \mathbf{m}_i , $1 \leq i \leq 3$, we denote the centres of mass of the neighbouring simplex faces. Six triangles are constructed by connecting $\tilde{\mathbf{v}}$ with the pairs $(\mathbf{m}_i, \mathbf{v}_i)$, $1 \leq i \leq 3$, $(\mathbf{m}_i, \mathbf{v}_{i-1})$, $2 \leq i \leq 3$ and $(\mathbf{m}_1, \mathbf{v}_3)$. The distance is computed by taking the shortest perpendicular distance to the six thus constructed triangles. This measure leads to a continuous, but not differentiable approximation of the distance to the 3DAO surface. For this reason, this approximation is called the C^0 distance measure throughout the remainder of this text.

2.3.3 Contour averaging method

Let the set of user contours be given by \mathcal{X}_i , $1 \leq i \leq n$. In the contour averaging method, first an initial correspondence between \mathcal{X}_1 and all other contours is estab-

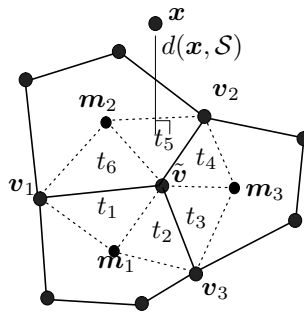


Figure 2.3: Approximation of the distance from a point to a 3DAO surface.

lished for an arbitrary resampling of \mathcal{X}_1 denoted by $x_{1,k}$, $1 \leq k \leq m$, by finding the closest points $x_{j,k}$ on \mathcal{X}_j , $j > 1$. The first estimate for the points on the average contour \mathcal{Y} is computed from

$$y_i = \frac{1}{n} \sum_{j=1}^n x_{j,i}. \quad (2.6)$$

Next, the sampling of the input contours \mathcal{X}_j is updated by computing the intersection points of the lines normal on \mathcal{Y} at each of the y_i with the contours \mathcal{X}_j . The newly established sampling is then used to update \mathcal{Y} . This procedure is iteratively repeated until the variation of the average contour at each iteration becomes negligible. To establish the variations between the contours \mathcal{X}_j , the distances are measured between the corresponding points $x_{j,k}$ resulting from the averaging procedure. For the validation we have used a discretisation with 60 points on each contour. The number of averaging steps performed was 5.

We used the average contouring method to generate an averaged golden standard contour based on the six manual contours. We measured the average deviations of the user contours from this golden standard contour to evaluate the variability in the validation set. Next we performed the contour averaging method once more on the intersection contour of the automatically segmented surface and the golden standard contour to measure the errors between the average of the manual contours and the automatic segmentation result. Also, we computed the distances between the sample points on the golden standard contour to the 3DAO surface, employing the distance measure presented in section 2.3.2.

2.3.4 Statistical evaluation

For the statistical evaluation of the performance we used the extension of the index from Williams [128] for multivariate data as proposed in [13]. This index lets us compare the performance of the algorithm to the performance of the users, providing an index that normalises the error estimates for the algorithm with respect to the quality and the equivocality of the features. Let the n users be indexed from 1 to n and let the index 0 refer to the automatically derived segmentation. Let $v_{i,k}$ denote

a vector of m observations for user i , $0 \leq i \leq n$, $0 \leq k < m$. And let $e = e(\mathbf{v}, \mathbf{v}')$ be the function that measures the variation between two observations. The average disagreement between two users i and j is computed from

$$D_{i,j} = \frac{1}{m} \sum_{k=1}^m e(\mathbf{v}_{i,k}, \mathbf{v}_{j,k}). \quad (2.7)$$

This leads to the following formula for the modified Williams index

$$I' = \frac{\frac{1}{n} \sum_{j=1}^n \frac{1}{D_{o,j}}}{\frac{1}{n(n-1)} \sum_j \sum_{k:k \neq j} \frac{1}{D_{j,k}}}. \quad (2.8)$$

Please note the difference with the original formulation in [13], which has an extra factor 2 in the denominator, which is incorrect with respect to the summation domain.

For the application at hand, the observations are the individual contours on the image slices. In our approach we used both the maximum difference and the root mean squared (RMS) error to measure the disagreement between the observers. To compute the 95% confidence interval of this index we use the jackknife parametric sampling approach followed in the original article [13]. The performance of the automatic segmentation method is considered to be as good as the performance of the observers if the confidence interval contains the value 1.0.

2.4 Results

The image registration always resulted in a good visual match between the 2D B-TFE and the 3D B-TFE volumes. For one patient we observed a major improvement in the initial 3D rigid match from the slice-by-slice refinement (see figure 2.4). The maximum difference in the translations between two slices for this patient was 2.1 mm. For the other patients, the initial match of the rigid registration was already good. Application of the registration method resulted in maximum translations of less than half the in-plane voxel size and only minimal rotations.

Figure 2.1 shows segmentation examples of the lumen and the outer vessel wall both in 3D projection view and as an intersection contour with a transversal imaging plane. Visual inspection of the segmentation results for six patients showed good correspondence between the reconstructed surfaces and the image features for all patients. In one case, an automatic threshold had to be overruled because of a bad surface initialisation. For all other patients, the automatically determined parameters could be used. For two patients significant motion was observed that could be replicated with the dynamic propagation technique. For the other patients, the aorta deformations were too small to capture within the image resolution.

Tables 2.1 and 2.2 list the variability in the validation set for the lumen and the outer vessel contours respectively. There is one major outlier (aneurysm 3, lumen).

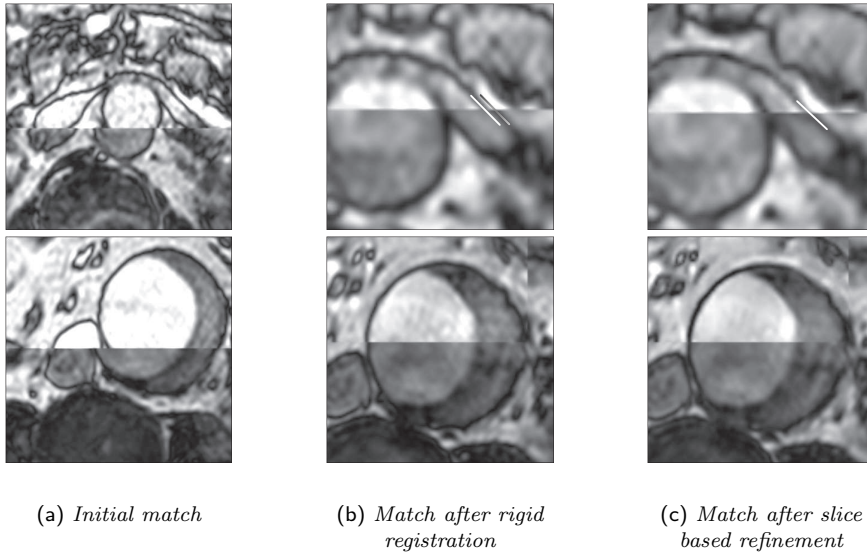


Figure 2.4: The effect of the registration procedure for two slices. The top halve of the overlay images shows the 2D B-TFE image and the bottom halve shows the 3D B-TFE image. The lines in figures (b) and (c) indicate a position where the 2D refinement results in an improved match.

| Data set | Max. | Average \pm stdev | RMS | 0.95 percentile |
|----------|------|---------------------|-----|-----------------|
| 1 | 2.1 | 0.5 ± 0.3 | 0.6 | 0.9 |
| 2 | 1.9 | 0.6 ± 0.3 | 0.7 | 1.1 |
| 3 | 8.3 | 1.0 ± 1.2 | 1.6 | 3.9 |
| 4 | 2.0 | 0.6 ± 0.3 | 0.6 | 1.0 |

Table 2.1: Average deviation of the manual contours from the averaged golden standard contours for the aneurysm lumens.

Even with this outlier removed, the maximum deviation from the average golden standard contour is considerable, up to 4 mm. The maximum distances between pairs of observers are 7 mm, 6 mm, 21 mm and 6 mm for the lumen contours and 6 mm, 11 mm, 10 mm and 7 mm for the outer vessel contours of the respective AAAs.

Even though these variations may be considerable, these severe disagreements are generally very local, as can be observed in the 0.95 percentiles of the errors and the RMS error, which are both very close to the pixel size for all data sets, except for the lumen of aneurysm 3.

| Data set | Max. | Average \pm stdev | RMS | 0.95 percentile |
|----------|------|---------------------|-----|-----------------|
| 1 | 2.2 | 0.5 ± 0.2 | 0.5 | 0.9 |
| 2 | 3.0 | 0.6 ± 0.4 | 0.7 | 1.6 |
| 3 | 4.0 | 0.7 ± 0.5 | 0.9 | 1.8 |
| 4 | 2.5 | 0.5 ± 0.4 | 0.6 | 1.2 |

Table 2.2: Average deviation of the manual contours from the averaged golden standard contours for the aneurysm vessel walls.

In figure 2.5 we have plotted the segmentation errors with respect to the average golden standard contour. The in-slice maximum errors are considerable, especially for aneurysm 3. However, the 0.95 percentiles of the distances are generally below 5 mm and the RMS errors are around 2 mm. The maximum C^o distances from the contour points to the 3DAO surface are lower than the in-slice distances, always below 5 mm. The RMS errors are again around 2 mm. The propagation algorithm clearly causes the errors to increase. However, this increase is generally not very large with respect to the original errors.

In figure 2.6 we have plotted the 0.95 confidence intervals of the modified Williams index (2.8) using both the maximum error and the RMS error per slice as a disagreement measure. In all but two cases, the algorithm is outperformed by the observers. It is noteworthy that a larger segmentation error does not necessarily lead to a lower modified Williams index (cf. aneurysm 1 and aneurysm 3) since the performance of the algorithm is now normalised with respect to the user variability. The modified Williams index also shows that the segmentation performance decreases with application of the propagation technique as the modified Williams index is always slightly lower for the 12th phase than for the first phase. For this statistics both the maximum error and the RMS error lead to a similar performance estimate.

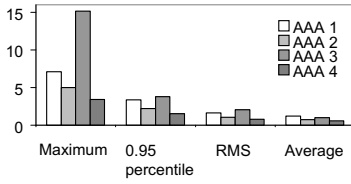
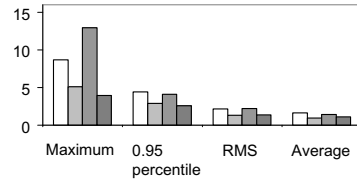
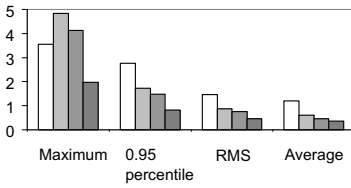
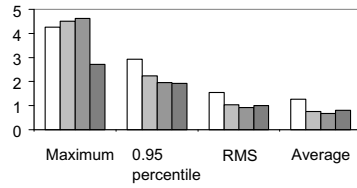
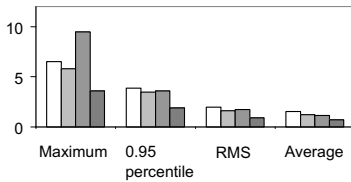
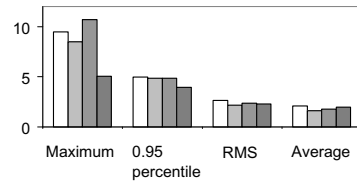
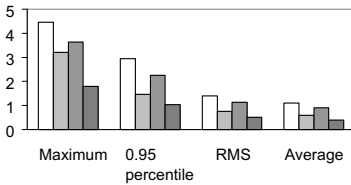
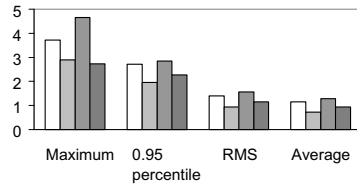
(a) *Lumen, phase 1, in-slice error*(b) *Lumen, phase 12, in-slice error*(c) *Lumen, phase 1, C⁰-distance based error*(d) *Lumen, phase 12, C⁰-distance based error*(e) *Vessel, phase 1, in-slice error*(f) *Vessel, phase 12, in-slice error*(g) *Vessel, phase 1, C⁰-distance based error*(h) *Vessel, phase 12, C⁰-distance based error*

Figure 2.5: Segmentation errors for the first and the last dynamic phase for the segmentations of the four aneurysms.

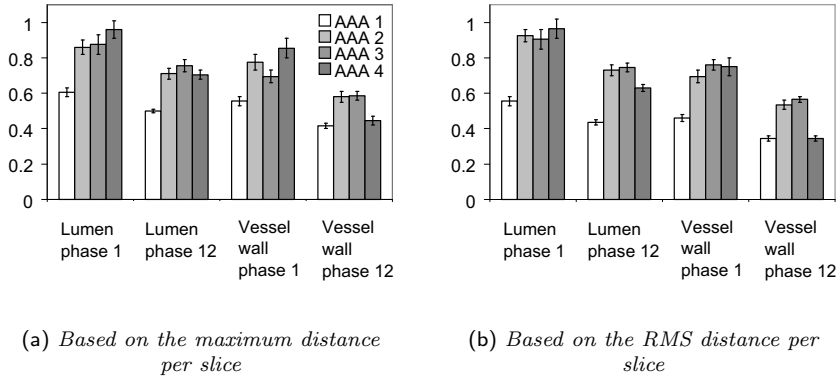


Figure 2.6: Modified Williams index (with 0.95 confidence interval) for the lumens and the vessel walls for the four aneurysm segmentations at the first and the last dynamic phase for the maximum error and the RMS error per slice.

Figure 2.7 shows the volume of the lumen and the vessel of aneurysm 1 over the cardiac phases as computed with the propagation algorithm and figure 2.8 shows the end-diastolic volume of the automatic segmentation result in relation to the variability within the validation set. Once more, the automatic estimate is mostly not within the variability bounds. However, the errors with respect to the volume estimate based on the average golden standard contours are very small, below 7%.

2.5 Discussion

The image registration method proved capable of correcting the motion present in the images in our data set. Moreover, a good initial match is left intact by the algorithm, indicating that this approach may be applied as a pre-processing step without having to preselect the images.

The highest error in the segmentation occurred for the lumen of AAA3. In figure 2.9 we have plotted the user contours for the corresponding slice and the automatic segmentation result. The angle between the lumen surface and the imaging plane is rather small, resulting in an unclear transition between lumen and thrombus because of the partial volume effect. One of the experts has chosen to follow a dip in the high intensity area in the vessel. Another expert has delineated the entire high intensity area as the vessel lumen. The automatic segmentation partly follows both features. The in-slice variations between the several manual segmentations and the automatic segmentation is very high because of this unclear feature. The C^o distance from the contours to the 3DAO surface, however, is no more than 4 mm.

In general, the errors based on the 3-dimensional distances are considerably

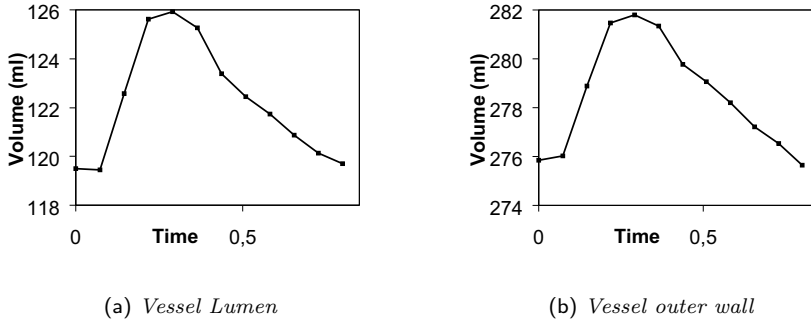


Figure 2.7: The dynamic volume of aneurysm 1 measured on the twelve subsequent imaging phases.

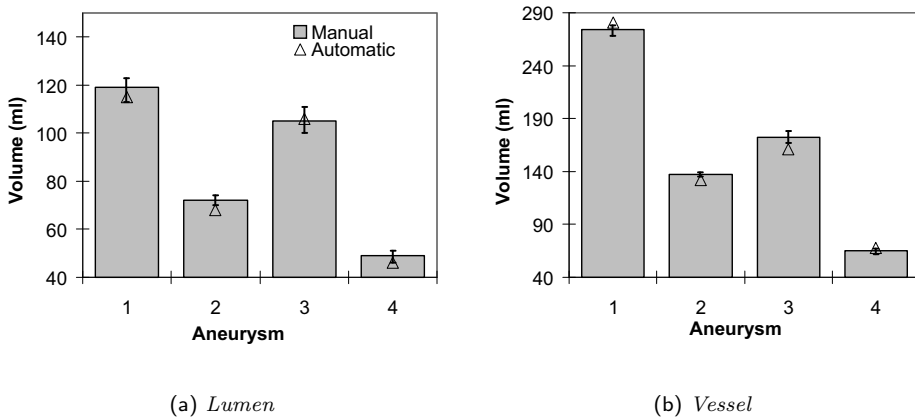


Figure 2.8: End-diastolic volumes of the four aneurysm lumens and the complete vessels, based on the average golden standard contours. The whiskers indicate the variations in the validation set. The open triangular mark indicates the end-diastolic volume based on the automatic segmentation. Although the automatically determined volumes are not always within the bounds of the variation in the validations set, the errors are small, below 7%.

smaller than errors based on the in-slice distances. For the manual segmentations, it is possible to draw contours that do not match a consistent smooth 3D surface. The deformable model has an extra, highly desirable, smoothness constriction which can cause the segmentation to deviate from the contours, even when the image features are very good. Therefore it is not unlikely that the maximum in-slice distance gives a too negative impression of the algorithms performance. On the other hand, the

orientations of the normals of the contours at the sample points are not taken into account when computing the distance between the contours and the 3DAO surface. Therefore, this 3D distance measure may give a too optimistic impression of the segmentation performance.

When not taking into account a small number of outliers the RMS error reported for MR by de Bruijne et al. is approximately 2 mm for the MR based segmentation method. For her CT based segmentations, the errors are slightly smaller, around 1.5 mm. The in-slice RMS errors for our segmentations were close to 2 mm, so our performance appears to be similar.

Olabarriaga et al. [79] employ a distance measure that allows through-slice shortest distances for their CTA based segmentation method. Therefore, the distance between the contour points and the 3DAO surface is probably the best measure to use when comparing our results to theirs. The maximum segmentation errors reported by Olabarriaga are around 5 mm, which compares well to the maximum errors we observed.

Comparison of our results with those from Subasic et al. [104] is somewhat hard since we did not compute any performance measure based on pixel-wise overlap. However the results reported in that publication were not very good. Although it appears that our results are slightly worse than those reported by Magee et al. [68] for CTA, a true comparison is not possible because we do not know how the errors were computed in that study.

One clear limitation of this work is the small number of data sets used for the validation. In [20, 21, 79, 104] a higher number of data sets is used in the validation. However, those validations were based on the manual segmentations of a single user. The high variability between users in our trial indicates the importance of having several expert segmentations for data with unclear or even confusing features like the MR data used in this trial. Accurate manual segmentation of this data is time consuming and therefore it is difficult to obtain large numbers of manually segmented data from an adequate number of expert users. The relatively large variation between the expert users indicated that the quality of the data may be an important limiting factor for computing rupture risk criteria both with automatic segmentation and with manual interaction.

The features used for our segmentation are strikingly simple compared to the more advanced training and classification techniques used by others. The fact that we have obtained quite good results with a rather basic approach for these novel data sets is encouraging.

The propagation method that we developed allows automatic computation of the dynamic volume of the vessel. The combination of the patient's blood pressure and the dynamic volume may be used to estimate the vessel wall compliance, which is both an important clinical parameter and a potentially important input for numerical simulations of the vessel wall motion since it is directly related to the wall's material properties.

In this study, we have observed considerable variations in the manual segmentations of the expert users with respect to the maximum error. In chapter 5 of this

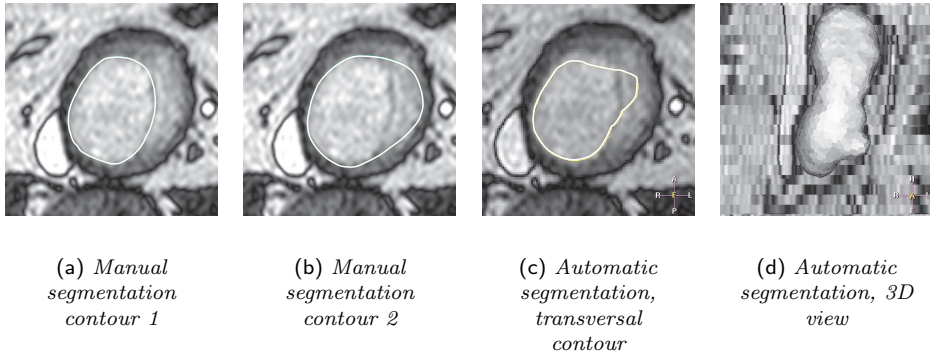


Figure 2.9: Largest user variation for the lumen of AAA3. Two users have put the manual segmentation at separate features (a,b). The automatic segmentation partly follows each feature (c). The shortest 3D path from the average user contour to the segmentation surface is through-plane (d).

thesis the sensitivity of the wall stress we compute with the finite element method for these variations is investigated. Our other future research is aimed at improving our segmentation method by using multi-spectral MR data with a larger set of image features.

2.6 Conclusions

We have developed and implemented a highly automated registration and segmentation method for AAA based on novel non contrast-enhanced combined 2D and 3D MR data sets. A validation study with multiple observers has provided objective numbers for the quality and the ambiguity of the image features in these data sets. Our results indicate that MR may provide automatic segmentations with an accuracy similar to the values reported for other CTA and MRA based methods. The dynamic propagation technique that we have developed has the potential to give more insight to the patient-specific material properties of AAA.

Computational Mesh Generation for Vascular Structures with Deformable Surfaces

Abstract

Computational blood flow and vessel wall mechanics simulations for vascular structures are becoming an important research tool for patient-specific surgical planning and intervention. An important step in the modelling process for patient-specific simulations is the creation of the computational mesh based on the segmented geometry. Most known solutions either require a large amount of manual processing or lead to a substantial difference between the segmented object and the actual computational domain. We have developed a chain of algorithms that lead to a combined implementation of image segmentation with deformable models and 3D mesh generation. The resulting processing chain is very robust and leads both to an accurate geometrical representation of the vascular structure as well as high quality computational meshes. The chain of algorithms has been tested on a wide variety of shapes. A benchmark comparison of our mesh generation application with five other available meshing applications clearly indicates that the new approach outperforms the existing methods in the majority of cases.

3.1 Introduction

Atherosclerotic disease is an important cause of death in a large portion of the world. Computational simulations of hemodynamics and vessel wall mechanics in atherosclerotic vascular pathologies such as aneurysms and stenoses have proven to be an important research tool. Hemodynamical simulations have been performed for cerebral aneurysms [12, 102], abdominal aortic aneurysms (AAA) [28, 37, 132] the carotid arteries [11, 101] and the coronary arteries [75, 83]. These simulations may be used to study the development of the pathologies, the risk factors associated

The development and implementation of the 3D meshing prototype Mesh Machine was performed at Medisys, Philips Medical Systems Research Laboratory in Paris.

with the specific nature of the pathology, and the expected outcome of surgical intervention.

An essential step to derive a well-defined model for computational fluid dynamics or solid mechanics simulations from a medical image is the discretisation of the three-dimensional domain which is called mesh generation. For patient-specific computational modelling the pipeline leading from the image to the computational mesh usually comprises

- segmentation of the medical image,
- modelling of other structures that are not visible in the image,
- generation of a surface mesh,
- creation of planar regions for boundary conditions,
- volume mesh generation,
- optimisation of the mesh.

The main criteria for this pipeline are

- generality,
- robustness,
- geometrical accuracy,
- smoothness control,
- resolution control,
- speed,
- quality and validity of the mesh.

A variety of automatic approaches for mesh generation from segmented medical structures has been proposed in literature. A classic approach to build meshes from medical images is based on surface interpolation between a set of contours describing the segmented shape [37, 84, 94]. The main problem with this approach is that the contours are delineated in 2D, without taking into account 3D smoothness constraints, and this generally leads to a set of contours that do not necessarily describe any sufficiently smooth surface. The smoothing or fitting operations needed to obtain a useful surface representation can lead to a reduction of geometrical accuracy. Some authors have proposed meshing methods that are essentially based on subdividing the image voxels themselves [10, 114], or a collection of cubes cast over the domain [36, 45, 70, 105], into elements. These methods impose no direct constraints on the topology or the connectedness of the domain. Furthermore, the domain that is obtained this way will have jagged edges, so that further optimisation and smoothing are needed.

A popular method for tessellating iso-intensity surfaces is the marching cubes method [66] which generates accurate but low-quality triangulations of the isophote surface. Many authors use mesh improvement methods or remeshing strategies to generate a high quality triangulation from initial low quality surface meshes such as the ones resulting from the marching cubes algorithm [49, 64, 114]. The main disadvantage is that the success of these methods still depends on the quality of the input surfaces. Furthermore, the assumption that the geometry boundary is

described by an image isophote only holds for quantitative imaging methods and even then only if the boundary transition is similar over the entire boundary of the object.

In spite of the automated 3D based solutions described above, meshing based on manually segmented 2D contours is still popular. One possible explanation for this is that none of the available image segmentation methods are fail-safe. Manual correction of automatic segmentation results is often a difficult and time-consuming process. A second explanation is that for many of the methods described above, a good segmentation does not guarantee the successful generation of a computational mesh. The deformable model method as used by Audette et al. [2] does not suffer from this limitation. In this approach, a successful image segmentation guarantees a high quality finite element surface mesh, because the criteria for the deformable model and the computational mesh are similar.

In this chapter we present a combined implementation of deformable models and mesh generation which is especially well suited for cardiovascular applications. We have made a number of important extensions and improvements with respect to Audette et al. [2] concerning mesh accuracy, resolution control, boundary plane creation and quality control. We also present two examples of applications of this method for vascular structures in different regions of the body.

3.2 Materials and methods

In this section we present the specific implementation of the pipeline described in the introduction. For the image segmentation we use the deformable surface model, or 3D active object (3DAO) model [2, 25, 41], which will be briefly discussed. Next, we give a detailed description of the algorithms used to generate the vessel wall and to obtain an accurate, high quality surface mesh. Finally, we will discuss the implementation and evaluation of the mesh generation and optimisation algorithms.

3.2.1 Deformable surface model

The 3DAO is a collection of connected non-planar simplex faces with connectivity number 2, which means that every 3DAO simplex node has exactly three neighbour vertices, as depicted in figure 3.1. The 3DAO can be iteratively deformed to fit the shape to image features. During segmentation of anatomical structures with 3DAO, the new position for a node is determined at every iteration from the current position via a time-discretised second order Newtonian-evolution equation

$$\mathbf{P}_i^{t+1} = \mathbf{P}_i^t + (1 - \gamma) (\mathbf{P}_i^t - \mathbf{P}_i^{t-1}) + \alpha \mathbf{F}_{int} + \beta \mathbf{F}_{ext}, \quad (3.1)$$

where \mathbf{P}_i^t denotes the position of the i -th simplex node at iteration t . With \mathbf{F}_{int} and \mathbf{F}_{ext} we denote the internal force (ensuring smoothness) and the external force (fitting the node to image features). The parameters α and β denote the respective weighting coefficients of these forces and γ is a damping coefficient used to stabilise the deformation process.

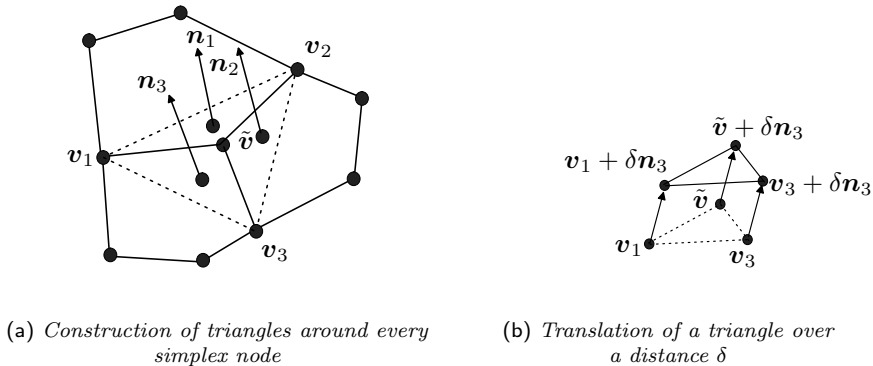


Figure 3.1: Creating an offset on a vertex node of a 3DAO.

3.2.2 Generation of thin-walled structures

For hemodynamical simulation in vascular geometries it is often necessary to accurately model thin structures such as the vessel wall. This requires the generation of an offset surface, i.e. a surface with a prescribed small distance to the original surface. The distance between surfaces consisting of basic facets such as triangles or (generalised) simplices locally varies. Given a closed surface consisting of planar regions it is impossible to create a new surface with a similar description with a constant euclidian offset distance, because the true offset surface is not piecewise planar. One of the advantages of using the 2-simplex structure is that it allows for a fairly easy and accurate offset procedure which provides a one-to-one correspondence between the facets on the two surfaces, and a constant gap between the corresponding simplices. To achieve this, we shift all of the facets outwards and recompute the vertex positions. This approach can only work for a model in which every vertex is described as the intersection of exactly three planes, such as the 2-simplex structure.

For every node \tilde{v} in the simplex mesh, three triangles are created from the vertex and its three neighbours v_i , $1 \leq i \leq 3$, with normals \mathbf{n}_i , as depicted in figure 3.1(a). The points of the three triangles uniquely define three planes, which may be described by their support points and normals through $p_i = (v_i, \mathbf{n}_i)$. From these planes we create three offset planes $\hat{p}_i = (v_i + \delta \mathbf{n}_i, \mathbf{n}_i)$. The new position of the node \tilde{v} in the offset mesh is the intersection point of \hat{p}_1 , \hat{p}_2 and \hat{p}_3 . Theoretically, it is possible that the intersection point is not defined. However, in our numerical implementation this does not provide any problems, since the triangles never lie exactly in the same plane. By applying this procedure for every node in the simplex mesh, the entire surface is shifted over the distance δ . In the applications presented in this work, we have only modelled structures with an assumed, constant wall thickness. However, if additional wall thickness information is available, the offset

distance could be allowed to vary locally.

Since the method for offsetting a discrete surface aims at creating a prescribed gap between the corresponding simplices in the original and the transformed mesh, the distance between corresponding mesh nodes will generally be higher than the requested offset, depending on the local surface curvature. Evaluating the result of the offset procedure is therefore somewhat difficult. Employing stringent distance metrics such as the symmetrical Hausdorff distance will result in a very high error estimate, in our case actually related to the distance between the mesh points. To evaluate the offset procedure, we computed the maximum distance from the collection of centres of gravity of the facets of the offset 3DAO, to the original 3DAO and the maximum distance from the collection of centres of gravity of the facets of the original 3DAO to the offset 3DAO. The maximum distance is now computed as

$$d_{\max}^c(S, T) = \max(\max(d(m \in M(S), T)), \max d(S, m \in M(T))), \quad (3.2)$$

where $M(\cdot)$ denotes the collection of centres of gravity of the facets of the 3DAO surface. We also computed the maximum of the average distances between the surfaces as

$$d_{\text{av}}^c(S, T) = \max\left(\frac{1}{n} \sum_{i=1}^n d(m_i \in M(S), T), \frac{1}{n} \sum_{i=1}^n d(S, m_i \in M(T))\right), \quad (3.3)$$

with n the number of facets in the simplex mesh. The offset method has been tested on three outer wall surfaces of AAAs segmented from MR with an average face area of 18 mm² for an inward offset of 2 mm.

3.2.3 Conversion of generalised simplex surfaces to triangulated surfaces

In order to generate triangular surface representations that can be used as input for a 3D tetrahedral mesh generation algorithm, the simplex surface needs to be transformed to a high quality surface triangulation. Audette et al. [2] have employed a method in which the centers of gravity of all of the generalised simplices are connected over exactly one simplex edge to obtain a triangulation which they call the dual triangulation, analogue to the duality between planar Voronoi subdivisions and Delaunay triangulations. For areas with high curvature, the triangulation that is derived from the simplex mesh in this manner will be completely located on one side of the simplex surface, thus providing a wrong local curvature estimate and, for closed surfaces, an underestimation of the enclosed volume. To solve this problem, we have constructed an iterative curvature correction method that provides a better geometrical estimate of the segmented surface without affecting the quality of the triangulation.

First we create the analogy of the standard dual triangulation similar to [2]. Let $F = \{f_i\}$, $1 \leq i \leq k$ be the collection of generalised simplex faces in arbitrary order with centres of gravity \mathbf{m}_i and let the number of vertices of face f_i be equal to c_i . In

```

u = 1
while (  $\tilde{d} > \varepsilon$  )
  i = 1
  while (  $i \leq k$  )
     $d_i = \frac{1}{c_i} \sum_{j=1}^{c_i} \mathbf{d}_{i,j} \cdot \mathbf{n}_i - \| \mathbf{m}_i^{u-1} - \mathbf{m}_i \|$ 
     $\mathbf{m}_i^u = \mathbf{m}_i^{u-1} + \lambda d_i \mathbf{n}_i$ 
    i = i + 1
  end while
   $\tilde{d} = \max_{1 \leq j \leq k} d_j$ 
  u = u + 1
end while

```

Figure 3.2: Curvature correction algorithm for the dual triangulation of a 2-simplex mesh in pseudo-code.

the algorithm the mesh vertices are initialised at the centers of gravity \mathbf{m}_i and then iteratively displaced. We will denote the position of these vertices at the j -th step with \mathbf{m}_i^j , with $\mathbf{m}_i^0 = \mathbf{m}_i$. The outward normal of face f_i is denoted with \mathbf{n}_i . The triangles connected to \mathbf{m}_i will be denoted with $t_{i,j}$ and the corresponding vertices of the f_i with $\mathbf{v}_{i,j}$, $1 \leq j \leq n_i$. Furthermore, with $\mathbf{d}_{i,j}$ we denote the perpendicular vector from $\mathbf{v}_{i,j}$ onto $t_{i,j}$. We choose a parameter λ between 0 and 1 and a convergence criterion $\varepsilon = \eta h_{\max}$, with h_{\max} the maximum of the initial distances between the triangle node and the simplex faces and $\eta \ll 1$. The initial value of the test parameter \tilde{d} is set to h_{\max} . The iterative procedure for the curvature correction method proceeds as indicated in figure 3.2. The geometrical interpretation of this algorithm is that we compute the shift of the triangle nodes along the outward normals that balances the distance between the triangle nodes and the simplex faces and the distances between the simplex nodes and the triangles, thus obtaining a more equal distribution of the errors between the two surfaces. Since directly shifting a single node to its optimal position would result in a suboptimal positioning of the remaining nodes of the connected triangles, we only shift the node in the direction of its optimal position proportional to λ . The effect of the procedure on the location of the triangles with respect to the simplex faces is depicted in figure 3.3.

We have evaluated the conversion method for a variety of ideal shapes and realistic medical structures. To investigate the sensitivity of the method for λ , we have varied this parameter along the range (0.02, 1.5) for a number of shapes, with a fixed convergence criterium $\eta = 10^{-14}$. To evaluate the influence of the resolution of the initial simplex mesh on the optimal choice of λ , we have applied the method for a range of values for λ for a simplex description of a sphere with a radius of 10 mm at several mesh resolutions.

3.2.4 Creation of planar regions for boundary conditions

For vascular structures, it is usually necessary to provide the boundary conditions for the system of differential equations being solved on cross-sectional planes through the vessel. These particular regions of the model have to be perfectly planar and should not have a too small angle with any part of the adjacent vessel wall, to avoid numerical problems when normal flow is prescribed. We create planar mesh regions by imposing cut-planes placed before and after the part of interest of the vascular structure (e.g. the aneurysm) and oriented perpendicularly to the centre line of the vascular system. This is done in three distinct phases. The first phase is performed in the simplex mesh domain and the other two are performed in the triangulated mesh domain.

The first step of the method is cutting the segmentation mesh with a plane. The intersection between a plane and the mesh consists of a piece-wise linear contour formed by the intersection locations between the edges of the mesh and the plane. At intersection locations, we insert new vertices and connect them by marching along the contour. At the end, the complete intersection contour is retrieved; this has the effect of creating a separation between parts of the mesh located below and above the cut plane. Only the part that contains the object of interest is kept and the resulting mesh is closed with one single simplex face, this face being composed of vertices that lie within the plane. The process is repeated for each required input or output region of the model.

The second step is performed after the mesh has been converted to a triangle mesh using the method introduced in section 3.2.3. The dual triangulation curvature correction process that transforms a simplex mesh to its triangular form does not

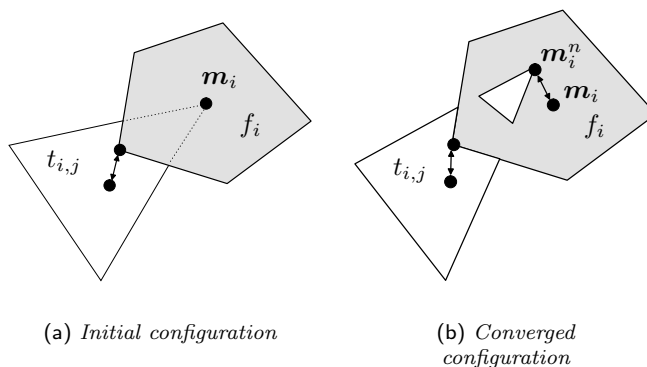


Figure 3.3: Curvature correction procedure. In the dual triangulation the triangle node is the center of gravity of the simplex causing a large distance between the simplex and the triangle. After application of the algorithm, the distances between the triangle node and the simplex and the simplex node and the triangle are well balanced.

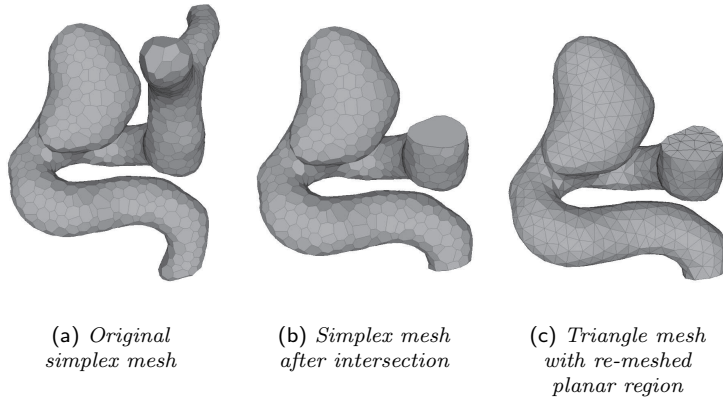


Figure 3.4: *Creation of planar regions for boundary conditions. On the left, the original mesh obtained from the segmentation of the patient-specific image is shown. In the middle, two cross sections have been created by cutting the vessel with a plane and the mesh is closed with a single face per section. On the right, the mesh has been converted to a triangulation and the planar cross sections have been re-meshed.*

keep the planar regions invariant. We need to recreate them: the vertices that belong to the inflow and outflow regions are simply projected to the same planes as the previous ones.

The last step consists of improving the quality of the triangulation located at the planar regions. The input and output regions of the model are now perfectly flat but may contain poor quality triangles (i.e. oversized and/or very elongated), which do not satisfy the mesh quality required for a good computational fluid mechanics (CFD) modelling. Therefore, the planar regions inside the intersection contour are re-meshed with the standard 2D Delaunay technique. Figure 3.4 shows the result of the method on the mesh of an intra-cranial aneurysm.

3.2.5 Quadratic tetrahedrons and surface interpolation

The accuracy of the CFD solution does not only depend on the quality and the number of mesh elements, but also on the order of the basis functions used for the approximation of the physical solution. For our simulations we use a $Q_2^+P_1$ tetrahedral Crouzeix-Raviart element with 15 nodes, providing a quadratic approximation of the unknown solution. To obtain the 15-node tetrahedral elements, the initial 4-node tetrahedrons are extended with one additional node on each edge, one additional node on each face, and one additional node in the element center.

Inside the volume mesh, the extra vertices are placed in the center of gravity of the defining entity. At the structure's surface, however, the additional vertices are used to obtain a more realistic approximation of the object's surface, by taking

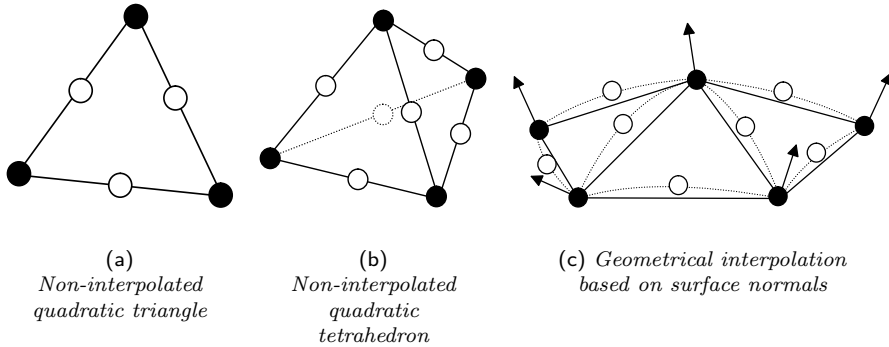


Figure 3.5: In figures (a) and (b) a quadratic triangle and a quadratic tetrahedron are shown respectively. Dark nodes represent mesh vertices while light nodes are additional vertices located at middle edge position. In figure (c) the interpolation is illustrated on a part of a triangle mesh. The additional vertices are also used to interpolate the surface. They are moved to a certain height relative to the edge they belong to by using an interpolating spline that is defined by the surface normals at the edge's vertices.

into account the local curvature of the surface. For this purpose we have adapted the curved PN triangles technique by Vlachos et al. [122], which was originally proposed to improve the visual quality of triangle-based surface tessellations for our purposes. Figure 3.5 illustrates the principle of curvature interpolation using the additional vertices of quadratic triangles. The vertex normal vectors are computed by averaging the normal orientations of adjacent triangles. Let \mathbf{n}_a and \mathbf{n}_b be the normal vectors associated to two vertices a and b with coordinates \mathbf{a} and \mathbf{b} defining a single edge. The normal vector \mathbf{n} associated to the edge is calculated as $\mathbf{n} = (\mathbf{n}_a + \mathbf{n}_b) / \|\mathbf{n}_a + \mathbf{n}_b\|$. To interpolate the curvature, we use a third degree polynomial approximation, which is the lowest order polynomial that satisfies the boundary conditions given by the position of the edge vertices and the corresponding normal vectors. The polynomial approximation is the parametric cubic spline

$$\mathbf{x}(t) = \sum_{i=0}^3 \mathbf{c}_i t^i, \quad (3.4)$$

where $t \in [0, 1]$ is the parameter defined along the curve. Let

$$\mathbf{t}_a := \left. \frac{d\mathbf{x}(t)}{dt} \right|_{t=0} = \mathbf{n}_a \times ((\mathbf{b} - \mathbf{a}) \times \mathbf{n}), \quad (3.5)$$

and

$$\mathbf{t}_b := \left. \frac{d\mathbf{x}(t)}{dt} \right|_{t=1} = \mathbf{n}_b \times ((\mathbf{b} - \mathbf{a}) \times \mathbf{n}), \quad (3.6)$$

where \times denotes the standard three dimensional cross-product. The coefficient vectors \mathbf{c}_i are computed as follows:

$$\mathbf{c}_o = \mathbf{a}, \quad (3.7)$$

$$\mathbf{c}_1 = \mathbf{t}_a, \quad (3.8)$$

$$\mathbf{c}_2 = 3(\mathbf{b} - \mathbf{a}) - 2\mathbf{t}_a - \mathbf{t}_b, \quad (3.9)$$

$$\mathbf{c}_3 = 2(\mathbf{a} + \mathbf{b}) + \mathbf{t}_a + \mathbf{t}_b. \quad (3.10)$$

The position of the additional vertex associated with the edge is given by

$$\mathbf{x}(t)|_{t=0.5} = \frac{\mathbf{a} + \mathbf{b}}{2} + \frac{\mathbf{t}_a - \mathbf{t}_b}{8}. \quad (3.11)$$

For the extra vertices corresponding to the triangle faces we use the nodes of the original simplex mesh from which the triangulation has been derived. Figure 3.6 shows the influence of the curvature interpolation procedure.

3.2.6 Tetrahedral mesh generation

The concluding step in the modelling process is to create a volume tessellation of the object to complete our model. Because of the specific requirements for finite element models of the cardiovascular system with respect to the volume representation, the mesh resolutions desired throughout the structure and the specific types of boundary conditions, we have developed our own volume mesh generation package, called Mesh Machine. The package is based on the Delaunay mesh generation technique, which has some major advantages when compared to the other existing methods. The method is fast and reliable and it is very generic since it can handle any realistic topology.

Our implementation is based on the Bowyer-Watson algorithm and its recent improvements [5, 97]. Employing the Delaunay circumscribing sphere criterion for a tetrahedron, the algorithm defines a rule for refining a mesh i.e. inserting a new vertex into the mesh domain. Elements that do not satisfy the Delaunay criterion are discarded, thus creating an open cavity in which the new vertex is inserted. Even though literature shows that this method is commonly used, it does not guarantee the quality of the generated mesh, while this is essential for the computations.

In our approach, we have developed tessellation algorithms that are able to produce very high quality meshes. The quality is controlled during the refinement process. The choice to refine an element depends on both the quality and on the size of the element. The goal is to obtain good quality elements with a good homogeneity in the volume of the elements. To quantify the quality of an element, we have tested several widely used quality measures as reported by Shewchuk [98] and Seveno [96] and chose the following one:

$$q_i = 2\sqrt{6}\frac{\rho}{h}, \quad (3.12)$$

where q_i is the quality of the i -th tetrahedron of the mesh, ρ is the radius of the inner sphere of the element and h is the length of the longest edge of the tetrahedron.

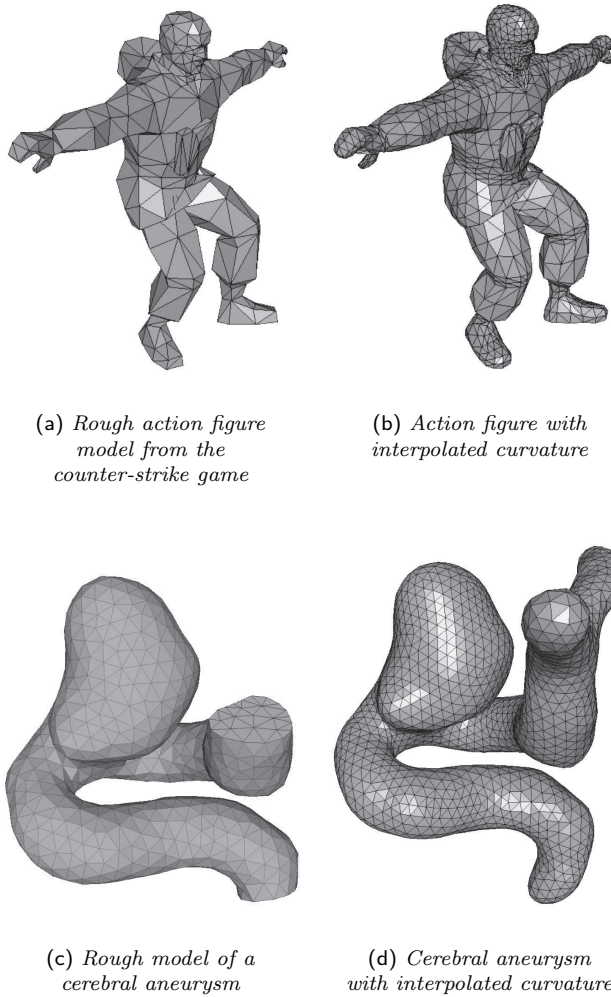


Figure 3.6: *Two meshes with interpolated curvature. On the top, a rough model from the Counter-Strike game. On the bottom, an intra-cranial aneurysm. For illustration purposes only, the additional vertices of quadratic triangles have been linearly connected, thus creating sub-triangles on the surface. The aneurysm model with interpolated curvature clearly provides a more realistic description of a smooth vascular structure.*

This quality measure has values in the range $[0,1]$ from completely degenerated elements to the regular tetrahedron. Based on the quality of mesh elements, we can restrictively generalise this measure to the quality of the whole mesh as

$$Q = \min_i q_i. \quad (3.13)$$

In other words, the quality of the mesh is the quality of its worst element. The use of this criterion ensures that not even one single bad element is allowed. This measure has the advantage that it is one of the fastest to compute while being accurate enough for our needs.

At each step of the refinement procedure, we use the quality function to choose between the several possible vertex insertion locations inside an element (e.g. element center) the one that gives the best quality. The local element size homogeneity is ensured with a size function that gives information on the optimal size of mesh elements. A value of the size function is associated to each vertex of the mesh and represents the ideal distance for which the vertex should be connected to its neighbours. The input surface gives the boundary conditions of the size function: for each surface vertex v_i we compute the average distance to its neighbours L_i . Next, the size information is propagated from the surface to the volume using a diffusion approach to initialise the size function everywhere in the 3D domain. During the refinement process, an optimal volume w_i of each tetrahedral element t_i is derived from the size function as:

$$w_i = \frac{1}{6} \left(\frac{1}{4} \sum_{i=1}^4 L_i \right)^3, \quad (3.14)$$

with L_i the size function associated to the vertex v_i of the tetrahedron. The optimal volume w_i represents the volume of a regular tetrahedron with edge sizes equal to the average of the size associated to its vertices. This optimal volume is compared to the actual volume to decide whether the element should be refined. By controlling both quality and volume of elements at the same time, we guaranty that both requirements are fulfilled when the refinement ends.

After refinement, a post-processing step improves the quality by relocating the volume vertices without changing the surface tessellation. With a steepest quality gradient-descent, we move each vertex step by step inside the valid domain. At each position, the quality of surrounding elements is updated and this process is iterated until the optimum is found. It has been demonstrated that the quality function has only one maximum inside the valid domain of the neighbour elements, so the algorithm is guaranteed to converge to the optimal solution [39].

In order to evaluate the efficiency of our mesh generation approach, we compared it with five other available packages in a benchmark test, using three criteria: the quality of the generated meshes, the overall meshing speed, and the robustness to complex geometries. The test set contains ten different meshes composed of synthetic objects (e.g. cube, sphere, torus) and real objects (e.g. vertebra, brain aneurysm).

The meshes have a wide range of geometric aspects (e.g. multiple surfaces, topologies) and quality. For the tests, the input meshes were taken as is. However, in order to provide the user the best possible quality in output, our application is able to analyse the input mesh quality and to optimise it if needed.

3.2.7 Application examples

We have applied the methods described in this chapter for solid mechanics simulations and flow simulations. To show the possible application areas we present two example simulations. The first simulation is a solid mechanics simulation of an elastic model of an end-diastolic AAA, segmented from cardiac triggered MR with a steady state free precession (SSFP) protocol. The AAA wall is modelled as a 2 mm thick neo-Hookean material with a shear modulus of 1.0 MPa [28]. The upper and lower cross-section of the structure have been clamped in all directions. On the inner wall of the aneurysm we have applied a pressure of 16 kPa (120 mm Hg) to simulate the maximum systemic load on the vessel wall, using eight equal pressure increments.

For the second application we have simulated the blood flow in a cerebral saccular aneurysm segmented from CTA. For the governing equations of the blood flow we have used the Navier-Stokes equation for an incompressible Newtonian fluid with a density of $1.08 \cdot 10^3 \text{ kg/m}^3$ and a viscosity of $5.0 \cdot 10^{-3} \text{ Pa}\cdot\text{s}$. These values are representative for human blood, when modelled as a continuum. The input signal for the cardiac flow was modelled as a plug-flow with

$$v(t) = v_o \left(1 + \frac{1}{2}(1 - \cos(\omega t)) \right), \quad (3.15)$$

with $\omega = 2\pi$, $v_o = 0.1$, and v in m/s. We simulated 5 cardiac cycles and evaluated that the periodic solution was stable in the last two periods. In this flow simulation, the vessel wall was assumed to be rigid. Both simulations have been performed with the finite element code SEPRAN (Septra analysis, Delft, the Netherlands).

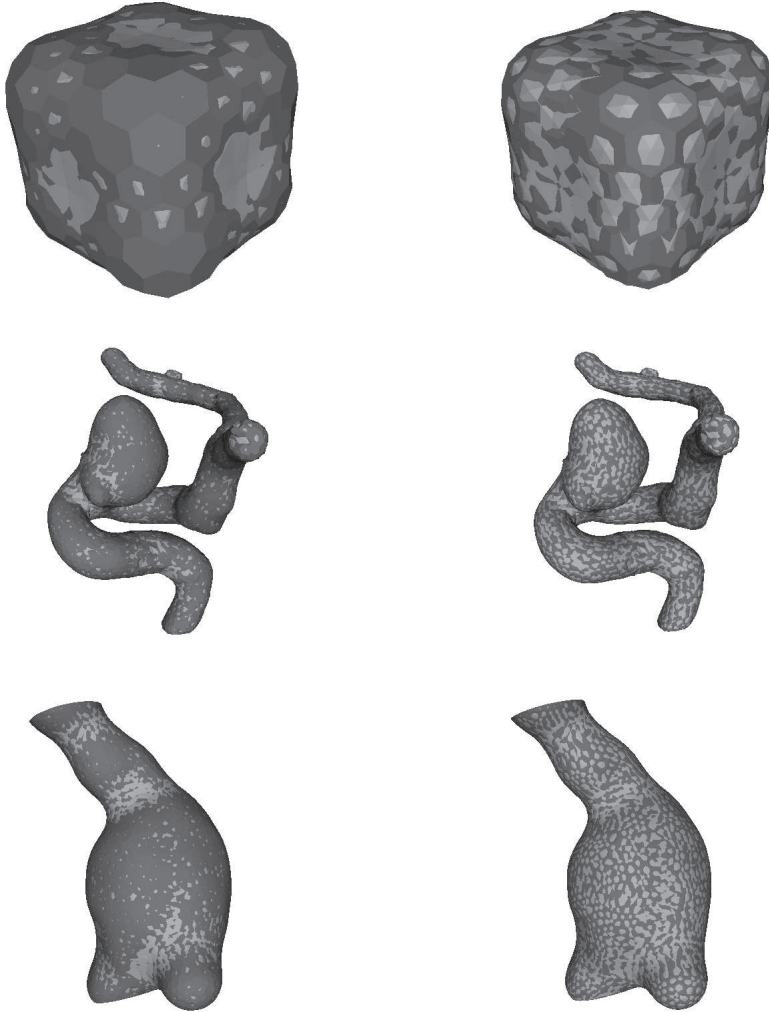
3.3 Results

3.3.1 Generation of thin-walled structures

The results of the validation of the offset procedure are listed in table 3.1. The average deviation from the desired offset distance is always below 1% of the offset distance. The maximum variation measured was approximately 6%.

3.3.2 Conversion of generalised simplex surfaces to triangulated surfaces

Figure 3.7 shows merge views of the simplex surfaces for a block, a cerebral vessel structure with an aneurysm and an AAA vessel wall with the dual triangulation and the triangulation after application of the algorithm. Clearly, the triangulation with



(a) Dark: simplex surface, light: dual triangulation

(b) Dark: simplex surface, light: corrected triangulation

Figure 3.7: Comparison of simplex surfaces with the dual triangulations and the triangulation after application of the curvature correction algorithm for a cube, a cerebral vessel structure and an AAA. The best match between the two surface representation is achieved when there is an equal distribution of dark and light regions over the surface.

| Data set | $d_{\max}^c(S, T)$ | $d_{\text{av}}^c(S, T)$ |
|----------|--------------------|-------------------------|
| AAA1 | 0.095 | 0.006 |
| AAA2 | 0.129 | 0.011 |
| AAA3 | 0.120 | 0.006 |

Table 3.1: Accuracy of the offset procedure for three AAAs for an inward offset of 2 mm. Maximum error in mm.

| data set | Volume simplex mesh (ml) | Relative error volume dual triangulation | Relative error |
|-----------------|--------------------------------|--|--|
| | | | volume triangulation with curvature correction |
| AAA1 lumen | 164 | 2.6% | 0.06% |
| AAA1 outer wall | 333 | 1.2% | 0.03% |
| AAA2 lumen | 167 | 1.4% | 0.03% |
| AAA2 outer wall | 433 | 0.6% | 0.02% |
| AAA3 lumen | 146 | 2.1% | 0.05% |
| AAA3 outer wall | 206 | 1.6% | 0.04% |

Table 3.2: Relative volumetric errors for the dual triangulation and the triangulation with curvature correction for the lumen and the outer vessel wall for three abdominal aortic aneurysms. Application of the correction algorithm significantly reduces the volumetric errors.

the curvature correction is overall closer to the initial simplex surface in all these cases. Table 3.2 shows the errors in the estimated volume for the lumen and the outer vessel wall location for three individual AAAs. The results show that the volume error is greatly diminished by application of the curvature correction algorithm. The graph in figure 3.8 shows the number of iterations necessary to match the stopping criterion for the lumen of the first AAA for different values of λ . It appears that the convergence is relatively insensitive to λ in the range (0.4, 1.0). The eventual convergence is only affected for extreme values for this control parameter. Similar results were obtained for tests with the two other AAA shapes. Finally, table 3.3 shows the number of iterations necessary for convergence for a sphere with a radius of 10 mm at several mesh resolutions. The results indicate that the optimal choice for λ is also hardly affected by the mesh resolution.

3.3.3 Tetrahedral mesh generation

The results of the benchmark are presented in table 3.4. Mesh Machine provides the best results for six of the test cases and the second best results for two of the other test cases. In terms of meshing speed, our meshing application is capable of generating up to 3000 elements per second on a Pentium IV clocked at 2GHz. In the context of the application, we use meshes with less than 100,000 elements. Over this

| Face area (mm^2) | Optimal value of λ | Minimum number of iterations |
|----------------------|----------------------------|------------------------------|
| 12.0 | 0.69 | 19 |
| 6.3 | 0.66 | 20 |
| 3.1 | 0.66 | 21 |
| 1.4 | 0.63 | 21 |

Table 3.3: Optimal value for λ for a sphere with a radius of 10 mm at several mesh resolutions. The value of the optimum is hardly affected by the mesh resolution.

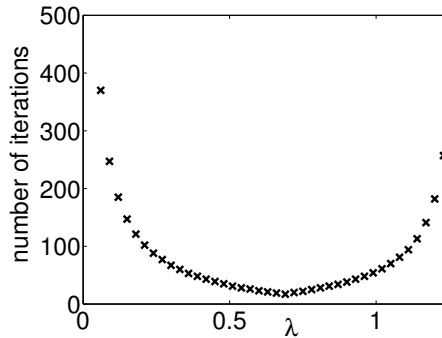


Figure 3.8: Number of iterations for the curvature correction method for AAA1 as a function of λ . Convergence is ensured in a wide range for the control parameter λ around its optimal value.

limit, the CFD computation time becomes prohibitive. Thus, in our application, the mesh generation takes less than a minute. Overall the meshing speed is similar to the average speed of the tested programs.

3.3.4 Application examples

Figure 3.9 shows the displacement, the strain and the wall stress distribution in a patient-specific model of an AAA. The image clearly shows regions with increased wall stress which are directly related to the specific shape of this aneurysm. The patient-specific wall stress for AAA may be used for rupture prediction [38].

Figure 3.10 shows the flow magnitude and the wall shear stress distribution in a cerebral vessel structure with a saccular aneurysm. Clearly, the shear stress in the aneurysm dome is significantly lower than in the parent vessel. Reduced wall shear stress can be indicative of vessel wall degradation.

3.4 Discussion

We have developed a methodology for segmentation, modelling and meshing of vascular structures from medical imaging. Every step in the chain has been tested

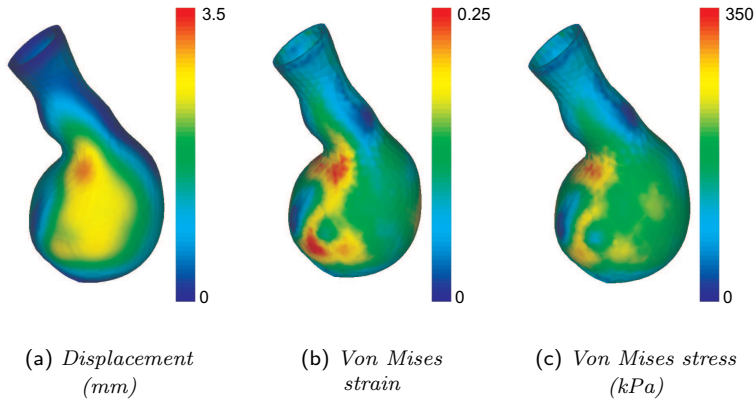


Figure 3.9: Displacement, stress and strain in the wall of an abdominal aortic aneurysm. Subfigures (b) and (c) clearly shows regions with increased wall strain and stress which are directly related to the specific shape of this aneurysm.

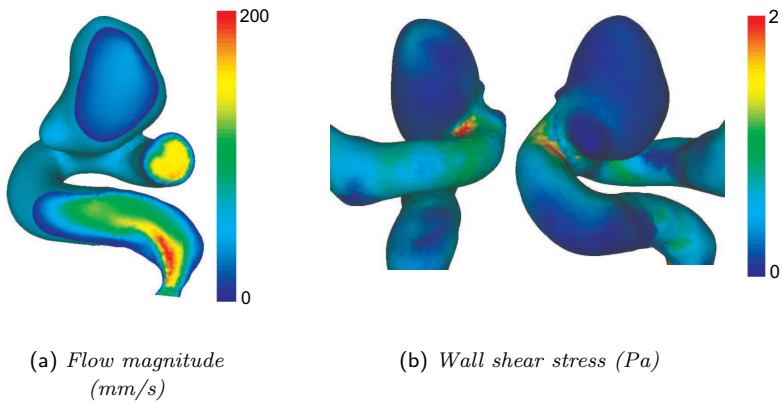


Figure 3.10: Flow and wall shear stress in a cerebral aneurysm. Reduced wall shear stress can be indicative of vessel wall degradation.

| Model | Geom-pack | Grummp | $Q_i = \min(q_i)$ | | | Mesh-Machine |
|-------------|-----------|--------|-------------------|---------|-------------|--------------|
| | | | Net-Gen | Tet-gen | Tet-Mesh | |
| Cube | 32.1 | 21.0 | 36.8 | 0.4 | 41.3 | 40.4 |
| Sphere | 28.9 | 19.7 | 37.7 | 7.0 | 39.9 | 39.8 |
| Cube 2 | 13.0 | 16.3 | 14.1 | 0.3 | 14.0 | 17.4 |
| Double Cube | 9.6 | 8.3 | 27.9 | 0.1 | 21.9 | 31.5 |
| Tore | 36.1 | 22.8 | 26.1 | 0.8 | 31.2 | 44.1 |
| Aneurysm | 26.9 | 18.7 | 21.8 | 0.8 | 20.4 | 29.0 |
| Aneurysm 2 | 5.4 | 4.1 | 6.3 | 0.0 | 6.9 | 3.0 |
| Femur | 30.9 | 19.7 | 35.0 | 0.9 | 34.5 | 38.8 |
| Tibia | 28.8 | 21.1 | 32.8 | 0.7 | 32.7 | 39.0 |
| Vertebra | 17.4 | 7.9 | 18.7 | 1.0 | 12.4 | 16.7 |

Table 3.4: Benchmark results of Mesh Machine compared to five other meshing software packages. The mesh quality as defined in equation (3.13) is presented as a percentage. Boldface figures correspond to the best results for these test cases.

and evaluated. The mean error of the offset procedure used to generate the vessel walls is very small for all three test geometries. The maximum error is approximately 6% of the offset distance. The fact that these errors are related to the curvature of the generalised simplices implies that the accuracy can be improved by refining the simplex mesh.

The curvature correction method for the dual triangulation of a generalised simplex surface produces triangulations that are very close to the original simplex surfaces. It appears that the optimal value for the control parameter λ is insensitive to the specific geometry and also to the mesh resolution. Convergence can generally be achieved in a broad range for λ around its optimal value within a limited number of iterations. The initial volume errors in table 3.2 are already relatively small. However, if the mesh resolution decreases, this underestimation of the enclosed volume will become worse. This also implies that details that are small with respect to the mesh resolution will be better retained with application of the curvature correction method. Therefore, the correction method provides an important accuracy improvement in the chain leading from a medical image to a computational mesh.

We have successfully applied the PN curved triangles method by Vlachos et al. [122], originally proposed for visualisation applications, for improved 2D meshing with quadratic elements. The high quality input surface meshes resulting from the curvature correction method, in combination with simultaneous quality and resolution control in the 3D mesh generation algorithm leads to very high quality meshes, that in general are significantly better than the meshes resulting from the other five packages that we tested.

Our prototype is very robust: it has been successfully tested on more than hundred meshes. It handles very complex mesh topologies including ones with several interconnected surfaces or non-manifold objects. Mesh Machine is also capable of

checking the validity of the input mesh by checking for self-intersection, flat triangles and holes.

In conclusion, we have developed and optimised a chain of algorithms, the combination of which allows robust, automatic generation of very high quality finite element meshes for realistic, patient-specific vascular structures, without compromising the accuracy of the segmented geometry.

Patient-specific initial wall stress in abdominal aortic aneurysms with a backward incremental method

Abstract

Patient-specific wall stress simulations on abdominal aortic aneurysms may provide a better criterion for surgical intervention than the currently used maximum transverse diameter. In these simulations, it is common practice to compute the peak wall stress by applying the full systolic pressure directly on the aneurysm geometry as it appears in medical images. Since this approach does not account for the fact that the measured geometry is already experiencing a substantial load, it may lead to an incorrect systolic aneurysm shape. We have developed an approach to compute the wall stress on the true diastolic geometry at a given pressure with a backward incremental method. The method has been evaluated for several simple test problems. The results show that the method can predict an unloaded configuration if the loaded geometry and the load applied are known. The effect of incorporating the initial diastolic stress has been assessed by using three patient-specific geometries acquired with cardiac triggered MR. The comparison shows that the commonly used approach leads to an unrealistically smooth systolic geometry and therefore provides an underestimation for the peak wall stress. Our backward incremental modelling approach overcomes these issues and provides a more plausible estimate for the systolic aneurysm volume and a significantly different estimate for the peak wall stress.

4.1 Introduction

Wall stress simulations on abdominal aortic aneurysms (AAA) have been widely recognised to provide an indication of rupture risk on a patient-specific basis [37, 38, 86, 110, 120, 125]. Fillinger et al. [38] have actually shown that wall stress can have a higher discriminatory value than the currently used maximum transverse AAA diameter.

The aneurysm shape has an important influence on the wall stress distribution [32, 123]. The correct approach for modelling the influence of intra-luminal thrombus is still controversial. Modelling the thrombus as an elastic medium leads to a diminished load on the vessel wall [27]. Clinical studies, however, indicate that the pressure at the aneurysmal wall is not affected by the presence of thrombus [95, 112].

Non patient-specific values are often used for the wall thickness and the material properties, since these model parameters cannot easily be assessed on a patient-specific basis. The value for the maximum pressure is either the monitored systolic pressure [37, 38, 86, 120, 125] or a non patient-specific systolic value [110].

All of the aforementioned patient-specific studies rely on non cardiac triggered computed tomography angiography (CTA), for which the measured AAA geometry is a non-trivial average of the dynamic aneurysmal geometry. With cardiac triggered CTA and magnetic resonance angiography (MRA) it is possible to capture the dynamic geometry at several stages in the cardiac cycle. However, medical imaging methods can never provide the unloaded aneurysmal geometry in a living subject, which would be the preferred starting geometry for a wall stress simulation load sequence.

None of the previously mentioned studies on patient-specific wall stress in AAA take into account the effects of the initial loads present in the diastolic geometry. Instead, the measured geometry is used as an unloaded starting point for a simulation in which the full systolic pressure is applied. We will refer to this modelling approach as the classical method for AAA wall stress simulations. Although this classical method will lead to a realistic range for the stress, the size of the systolic geometry may be overestimated.

There have been at least two previous publications on this subject. Raghavan et al. [87] assume that the forward deformation field is linearly related to the backward deformation field and they use a population mean for the compliance of the AAA, based on two cadavers, to estimate the volume change to the unloaded configuration. A recent paper on this subject by Lu et al. [67] uses an inverse modelling approach which is similar to our approach to compute the zero-pressure configuration for cerebral aneurysms. The paper by Lu et al. focusses on the comparison of constitutive models for the aneurysm wall. No attempts were made in this earlier publication to investigate the importance of the alternative modelling approach by a comparison to the classical approach.

The method presented in this chapter provides a means to obtain an approximation of the initial stress in the diastolic geometry by using a backward modelling approach. Although the application in this chapter is AAA, the method may be useful for stress simulations for all structures for which only a loaded configuration can be measured, as is often the case with medical applications. The method has been tested with simulations on idealised geometries for which the unloaded geometry and the reference configuration are known. We also applied our method on several realistic, diastolic AAA geometries obtained with cardiac triggered MR and compared our results with the results from the classical approach. The comparison shows that apart from the predicted overestimation of the volume, the classical

approach also provides an underestimation of the peak systolic wall stress.

4.2 Methods

The constitutive wall model and the finite element formulation that have been used for the implementation of our method have been previously described in [22, 115, 118]. However, since these papers focus on different applications and because the implementation is essential for our method, we briefly recapitulate the physics and the specific finite element method.

4.2.1 Constitutive wall model

For the AAA vessel wall we use the neo-Hookean model describing an isotropic elastic medium with large deformations. We consider an incompressible elastic medium in the time dependent domain $\Omega(t) \subset \mathbb{R}^3$, bounded by $\Gamma(t) = \partial\Omega(t)$, with outward normal \mathbf{n} . Let \mathbf{F} be the deformation gradient tensor

$$\mathbf{F} = \frac{\partial \mathbf{x}}{\partial \mathbf{X}}, \quad (4.1)$$

with \mathbf{X} the reference configuration and $\mathbf{x} = \mathbf{x}(\mathbf{X}, t)$ the current configuration. In the absence of body forces, the equations of motion and continuity from continuum mechanics theory are

$$\operatorname{div}(\boldsymbol{\sigma}) = \mathbf{0} \quad \text{in } \Omega, \quad (4.2)$$

$$\det(\mathbf{F}) = 1 \quad \text{in } \Omega. \quad (4.3)$$

The Cauchy stress for an incompressible elastic medium reads

$$\boldsymbol{\sigma} = -p\mathbf{I} + \boldsymbol{\tau}, \quad (4.4)$$

with p the hydrostatic pressure, \mathbf{I} the identity and $\boldsymbol{\tau}$ the extra stress resulting from deformations. For a neo-Hookean material, we have $\boldsymbol{\tau} = G(\mathbf{B} - \mathbf{I})$, with G the shear modulus and $\mathbf{B} = \mathbf{F} \cdot \mathbf{F}^T$ the left Cauchy-Green strain tensor (also known as Finger tensor).

The set of equations is completed with boundary conditions on each part of the domain boundary $\Gamma_k(t)$, with $\bigcup_k \Gamma_k(t) = \Gamma(t)$, and $\Gamma_k(t) \cap \Gamma_l(t) = \emptyset$, $\forall k \neq l$. The Dirichlet boundary conditions, which explicitly fix the displacement on the boundary read

$$\mathbf{x} \cdot \mathbf{n} = x_n, \quad (4.5)$$

$$\mathbf{x} \cdot \mathbf{t}_i = x_{t_i}, \quad \mathbf{n} \cdot \mathbf{t}_i = 0, i \in \{1, 2\}, \quad (4.6)$$

where \mathbf{t}_1 and \mathbf{t}_2 are linearly independent vectors. The Neumann boundary conditions, in which the surface traction $(\boldsymbol{\sigma} \cdot \mathbf{n})$ in the normal and tangential direction is

prescribed read

$$(\boldsymbol{\sigma} \cdot \mathbf{n}) \cdot \mathbf{n} = s_n, \quad (4.7)$$

$$(\boldsymbol{\sigma} \cdot \mathbf{t}_i) \cdot \mathbf{t} = s_{t_i}, \quad \mathbf{n} \cdot \mathbf{t}_i = 0, i \in \{1, 2\}, \quad (4.8)$$

A special case occurs when $s_n = 0$. This situation is referred to as a stress-free boundary condition.

4.2.2 Weak formulation

Let $W = \left\{ \mathbf{w} \in [H_o^1(\Omega)]^3 \right\}$, with $H_o^1(\Omega)$ the functional Hilbert space of functions f that satisfy the Dirichlet condition $f|_\Gamma = 0$ and let $Q = \{q \in L^2(\Omega)\}$. With substitution of the Neumann boundary conditions and partial integration, the weak formulation of equations (4.2) and (4.3) becomes

$$\int_{\Omega(t)} (\nabla \mathbf{w})^T : \boldsymbol{\sigma} d\Omega = \int_{\Gamma(t)} \mathbf{w} \cdot (\boldsymbol{\sigma} \cdot \mathbf{n}) d\Gamma, \quad \forall \mathbf{w} \in W, \quad (4.9)$$

$$\int_{\Omega(t)} q(\det(\mathbf{F}) - 1) d\Omega = 0, \quad \forall q \in Q. \quad (4.10)$$

The notation " : " is used to denote the 3D double dot product $\mathbf{A} : \mathbf{B} = \text{tr}(\mathbf{A} \cdot \mathbf{B})$.

Let $\Omega_n := \Omega(t_n)$ and $\Gamma_n := \Gamma(t_n)$. To evaluate the integrals in (4.9) and (4.10) over the domain (Ω_n, Γ_n) , we use the updated Lagrange approach, which implies that the previous configuration $(\Omega_{n-1}, \Gamma_{n-1})$ is taken as the reference configuration for (Ω_n, Γ_n) . The gradient operator is also interpreted with respect to the previous configuration. With \mathbf{F}_i^n we will denote the deformation tensor from the domain Ω_i to the domain Ω_n . Similarly, we will denote the gradient operator with respect to the domain Ω_i with ∇_i . This way the total transformation from Ω_o to Ω_n becomes

$$\mathbf{F}_o^n = \mathbf{F}_{n-1}^n \cdot \mathbf{F}_o^{n-1} = (\nabla_{n-1} \mathbf{x}_n)^T \cdot (\nabla_o \mathbf{x}_{n-1})^T. \quad (4.11)$$

It is customary in the updated Lagrange method to take the displacement field of the material points as the unknown. At time t_n , this field is defined through $\mathbf{u}_i(t_n) = \mathbf{x}_i(t_n) - \mathbf{x}_i(t_{n-1})$, where $\mathbf{x}_i(t_n)$ and $\mathbf{x}_i(t_{n-1})$ denote the position of a material point at two subsequent points in time. The updated Lagrange method is schematically depicted in figure 4.1.

When writing $\nabla_n = (\mathbf{F}_{n-1}^n)^{-T} \cdot \nabla_{n-1}$ the weak form of the system (4.9,4.10) becomes

$$\int_{\Omega_{n-1}} (\nabla_{n-1} \mathbf{w})^T : (\mathbf{F}_{n-1}^n)^{-1} \cdot \boldsymbol{\sigma} J_{n-1}^n d\Omega_{n-1} = \int_{\Gamma_{n-1}} \mathbf{w} \cdot \mathbf{s} \tilde{J}_{n-1}^n d\Gamma_{n-1}, \quad (4.12)$$

$$\int_{\Omega_{n-1}} q(J - 1) J_{n-1}^n d\Omega_{n-1} = 0, \quad (4.13)$$

where J_{n-1}^n and \tilde{J}_{n-1}^n are defined through $d\Omega_n = J_{n-1}^n d\Omega_{n-1}$ and $d\Gamma_n = \tilde{J}_{n-1}^n d\Gamma_{n-1}$. In equation (4.12), \mathbf{s} is defined by equations (4.7) and (4.8).

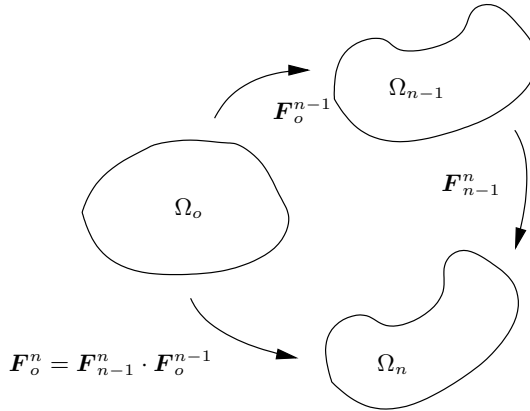


Figure 4.1: *The updated Lagrange method.*

4.2.3 Finite-element formulation and solution strategy

To obtain a finite-element formulation of the system (4.12,4.13) the domain (Ω, Γ) is divided into non-overlapping discrete elements. The discretised domains will be denoted by (Υ, Ψ) , with $\Upsilon = \{\mathbf{x}_i\}_{i=1}^m$ the complete collection of m finite element nodes and $\Psi \subset \Upsilon$ the collection of finite element nodes on the boundary of Υ . Within each element, the physical unknowns are approximated with Lagrange interpolation polynomials.

At each time step, the non-linear algebraic system rendered from (4.12,4.13) is linearised with Newton's method and we iterate to obtain a converged solution. The linearised system at each iteration step is preconditioned with an incomplete LU decomposition and solved with the Bi-CGSTAB method [117].

4.2.4 Notation conventions

To avoid any confusion about terminology that may have different meanings in the classical approach and the backward approach, we adopt a few conventions. With the *initial geometry* Υ_o we will always refer to a configuration in which the pressure is zero. In our model this configuration is assumed to be unloaded. With the *reference geometry* Υ_r , we will denote the geometry as it would be measured in a medical image, loaded with a non-zero pressure P_r . The geometry at maximum load $P_m (> P_r)$, Υ_m will be referred to as the *maximum loaded geometry*. If we write Υ with an index other than o, r or m , this index is related to the time series $\Upsilon_i := \Upsilon(t_i)$.

The deformations between two consequent time steps can be described by the collection of vectors describing the translations of the individual domain points $V_i = \{\mathbf{v}_j = \mathbf{x}_j(t_i) - \mathbf{x}_j(t_{i-1}) : \mathbf{x}_j(t_i) \in \Upsilon_i, \mathbf{x}_j(t_{i-1}) \in \Upsilon_{i-1}\}$. The total deformation from Υ_o to Υ_i can now be described by $U_i = \{\mathbf{u}_i : \mathbf{u}_i = \sum_{j=0}^i \mathbf{v}_j\}$. If a load is

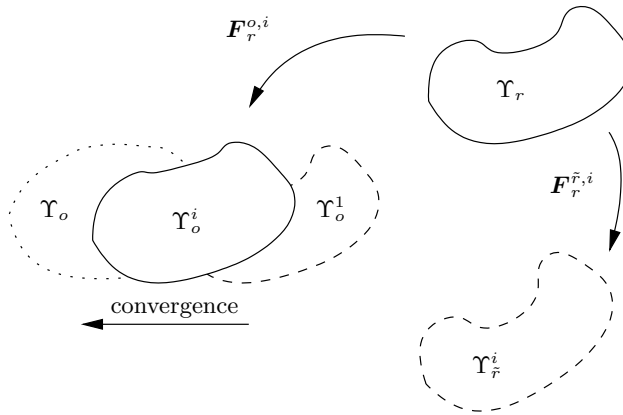


Figure 4.2: *Backward incremental modelling approach.*

applied on Υ_o , at time t_i the wall stress depends on the current shape, the pressure P_i , the deformations to the current configuration U_i and the shear modulus G , thus we can write

$$\boldsymbol{\sigma}_i = \boldsymbol{\sigma}(t_i) = \boldsymbol{\sigma}(\Upsilon_i, P_i, U_i, G) \quad (4.14)$$

to fully describe this configuration.

4.2.5 Backward incremental method

Our backward method is based on the backward application of computed forward deformations. At every iteration i , V_i is computed as before, but instead of taking $\boldsymbol{\sigma}_i = \boldsymbol{\sigma}(\Upsilon_i, P_i, U_i, G)$ as the next configuration, we take $\boldsymbol{\sigma}_i = \boldsymbol{\sigma}(\Upsilon_r, P_i, U_i, G)$, by which we implicitly update Υ_o by interpreting the computed forward deformations on the fixed reference domain. Clearly, the forward domain that can be computed by applying V_i on Υ_r will be different at every iteration. We will denote this domain by Υ_r^i and the corresponding deformation with $\mathbf{F}_r^{\tilde{r},i}$, thus explicitly indicating the dependence on i . The i -th approximation of Υ_o will be denoted by Υ_o^i , and the deformation from Υ_r to Υ_o^i with $\mathbf{F}_r^{o,i}$. The principle of the backward modelling is schematically depicted in figure 4.2. Since the computed forward deformations do generally not lead to an equilibrium between the stress and the pressure when these deformations are interpreted as deformations leading to the fixed reference domain, the system is not balanced at the start of each time step. However, if the next pressure increment would be extremely small, convergence of the iteration process at this next step will lead to an update V_i of U_i which ensures balance between the stresses and the pressure on a domain Υ_r^i that is very close to Υ_r . In the backward incremental approach, the iteration process thus serves not only to deal with the nonlinear nature of the system, but also to correct the error introduced in the previous incremental step.

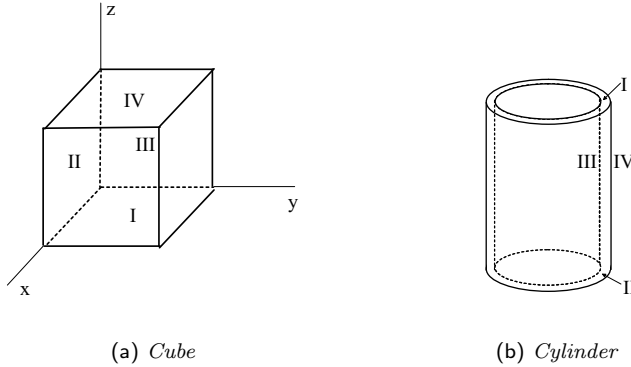


Figure 4.3: *Cube geometry and cylinder geometry.*

In the simulations we gradually increase the pressure on Υ_r in n steps to P_r , using

$$P_j = P_r \sin\left(\frac{j\pi}{2n}\right), \quad 0 \leq j \leq n, \quad (4.15)$$

thus applying large pressure increments at the beginning, and small pressure increments at the end of the process. The exact shape of the pressure-time curve is not essential as long as the final pressure increment is small and convergence is established at each step. Since $\mathbf{v}_j \rightarrow \mathbf{0}, \forall \mathbf{v}_j \in V_i$ as $P_i - P_{i-1} \rightarrow 0$, the process converges to a fixed collection $U = \{\mathbf{u}_i\}$ as $n \rightarrow \infty$. Also, since the process converges to an equilibrium at iteration $n - 1$, the error in Υ_r^n , for a finite number of increments n , will be proportional to $|P_n - P_{n-1}|$. Since the deformations and the stresses in the final solution are in equilibrium, we can compute the approximation for the unloaded geometry by applying the opposite of U on Υ_r to obtain Υ_o .

4.2.6 Simulations

We performed two simulations on the initial geometries depicted in figure 4.3. For both geometries, we first loaded the initial geometry Υ_o with a pressure P_r to obtain a deformed reference geometry Υ_r . Next, we assumed the initial geometry unknown and we applied the backward incremental method with 16 increments to reproduce it. For the cylinder (height 80 mm, inner radius 20 mm, wall thickness 2 mm) the upper and lower cross-sections (I and II) were fixed in the plane normal direction. To avoid further horizontal motion, two distinct points on face I were fixed in the x and y direction respectively. For the shear modulus we again chose a value of $G = 3.3$ MPa. The maximum load applied on face III was 1.0 MPa. The test criterion was the error in the approximation of Υ_o . To test the assumption that applying more increments in the backward method leads to an improved accuracy,

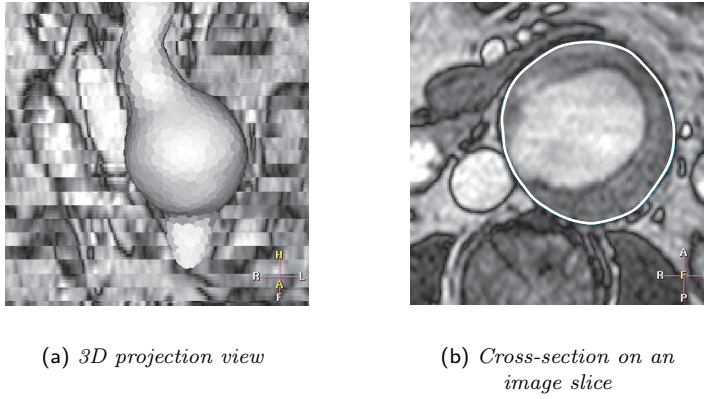


Figure 4.4: Segmentation of an aneurysm from an end-diastolic MR 2D B-TFE volume.

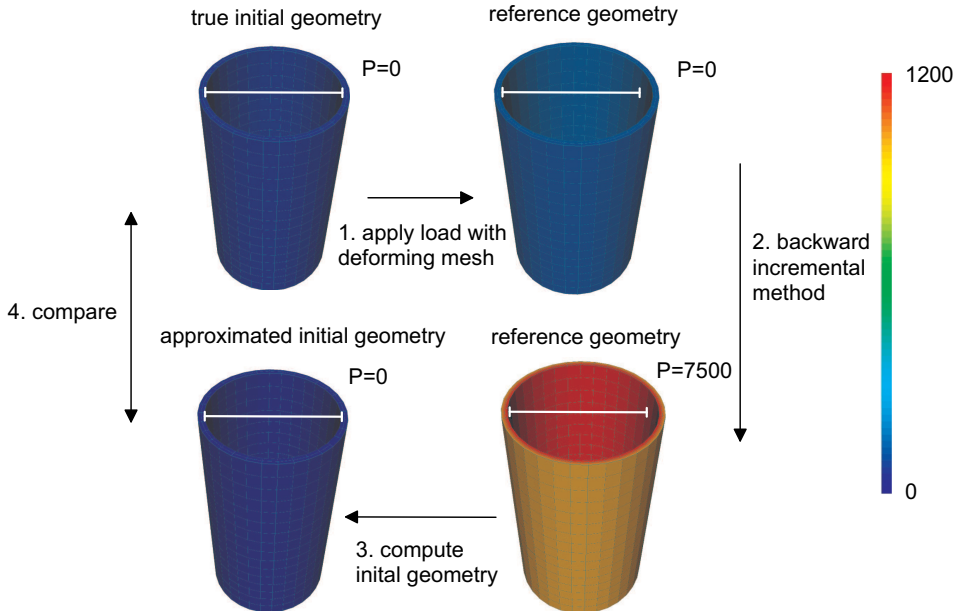


Figure 4.5: Approximation of the initial geometry of a cylinder, the colours represents the Von Mises stress in kPa. The pressures (P) are in mm Hg.

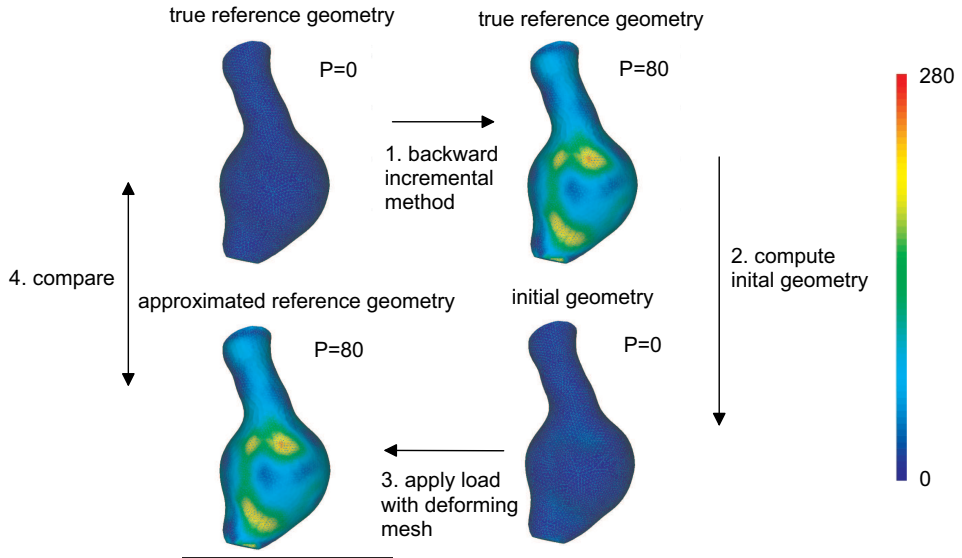


Figure 4.6: Approximation of the initial geometry of aneurysm 1, the colours represents the Von Mises stress in kPa. The pressures (P) are in mm Hg.

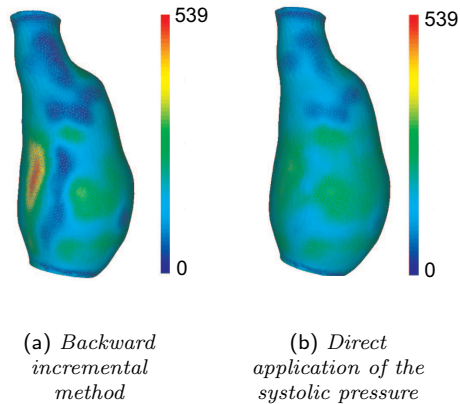


Figure 4.7: Von Mises stress (kPa) for aneurysm 2 at 120 mm Hg.

we also varied the number of increments in the simulation for the cube. The length of the principal axis of the cube is 0.5 mm. The cube's faces that coincide with the coordinate planes (I,II and III in the figure) were clamped in the normal direction. On the upper face of the cube (IV) a maximum pressure of $P_r = 1.0$ MPa was applied. The shear modulus of the material was taken as $G = 3.3$ MPa.

For the simulations on real AAAs the outer vessel wall has been segmented from the images for the end-diastolic phase from three gated 2D B-TFE MR image acquisitions using 3D active objects [25]. An example of a segmented AAA in the MR image is depicted in figure 4.4. Further details about the imaging protocol, the segmentation method and the meshing may be found in [23] (chapters 2 and 3). The assumed wall-thickness for the AAAs was 2 mm. The upper and lower cross sections of the aneurysm were clamped in all directions. For the shear modulus we used a value of 1.0 MPa, which is closely related to the measured realistic value for the Young's modulus for aneurysmal tissue of 2.7 MPa used by Di Martino et al. [28] for the working area of the stress-strain curve. For the first geometry (AAA1) we first applied the backward incremental method and computed the initial, unloaded geometry. Next, we re-applied the diastolic pressure on this geometry and checked that we obtained an accurate approximation of the measured diastolic geometry. In addition, we also compared the backward approach with the classical approach for all three AAAs. For this, we applied the backward incremental method with a reference pressure of 10.7 kPa (80 mm Hg) on the inner aneurysmal wall. Next, we increased the pressure to 16 kPa (120 mm Hg) to obtain Υ_m and compared the results with direct application of 16 kPa on the diastolic geometry. The number of increments for the backward modelling procedure in these simulations was 64, which proved sufficient for a high accuracy.

For the idealised simulations we used a $Q_2^+P_1$ hexahedral Crouzeix-Raviart element (27 nodes). The wall stress simulations on realistic AAAs were performed with a $Q_2^+P_1$ tetrahedral Crouzeix-Raviart element (15 nodes). All of the simulations have been performed with the finite element code SEPRAN (Septra analysis, Delft, The Netherlands).

4.3 Results

The initial geometries were well reproduced in the tests on the ideal geometries. The maximum displacement for the cube was $6.3 \cdot 10^{-2}$ mm, which is 13% of the principal length of the cube. The relative error of the reference diastolic maximum Von Mises stress with regard to the analytical solution was below 0.1%. The maximum mesh error in the approximated equilibrium was found to be $3.3 \cdot 10^{-5}$ for 16 iterations, which is $7 \cdot 10^{-3}\%$ of the principal size of Υ_o . The results in figure 4.8 illustrate that this error may be significantly diminished by increasing the number of increments in the backward method. Direct application of the approximated displacement field on the reference diastolic geometry gave an error of $3.7 \cdot 10^{-5}$ mm with respect to Υ_o , which is less than 0.01% of the cube's principal length.

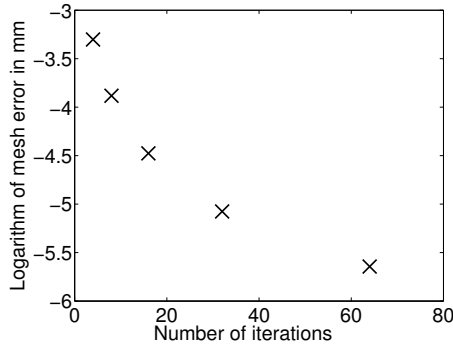


Figure 4.8: Maximum error of the approximated reference geometry against the number of iterations for the uniaxial deformation of a cube.

| Simulation | Maximum Von Mises stress (kPa) | Maximum Von Mises strain | Maximum displacement (mm) | Maximum error reference geometry (mm) |
|---------------|--------------------------------|--------------------------|---------------------------|---------------------------------------|
| AAA1 backward | 379 | 0.30 | 2.9 | $1.8 \cdot 10^{-3}$ |
| AAA1 direct | 283 | 0.23 | 1.8 | |
| AAA2 backward | 539 | 0.50 | 7.3 | $2.1 \cdot 10^{-2}$ |
| AAA2 direct | 405 | 0.40 | 3.0 | |
| AAA3 backward | 652 | 0.62 | 8.5 | $2.0 \cdot 10^{-2}$ |
| AAA3 direct | 470 | 0.45 | 2.6 | |

Table 4.1: Simulation results for the realistic aneurysm shapes as segmented from MR.

The several stages for the simulation on the cylinder are depicted in figure 4.5. The maximum displacement in this test was 4.3 mm. The maximum error in the approximation of the equilibrium reference geometry was $4.0 \cdot 10^{-3}$ mm. The error in the approximation of the original unloaded geometry was $7.3 \cdot 10^{-3}$. Both values are well below $5 \cdot 10^{-2}\%$ of the cylinder's radius, and they represent less than 0.17% of the maximum displacement.

The results of the simulation in which we used the backward incremental method to compute the initial geometry of AAA1 are depicted in figure 4.6. The maximum displacement between the diastolic and the computed reference geometry was 2.3 mm. The maximum error between the measured geometry and the reproduced geometry was $1.8 \cdot 10^{-3}$ mm. For all three realistic AAAs, the computed peak wall stress was higher when the initial diastolic loads were taken into account via the backward incremental method. Table 4.1 lists the simulation results for all three AAAs for both our backward modelling and the classical modelling of systolic wall stress. Comparisons between the Von Mises stress for AAA2 and AAA3 are shown in figures 4.7 and 4.9.

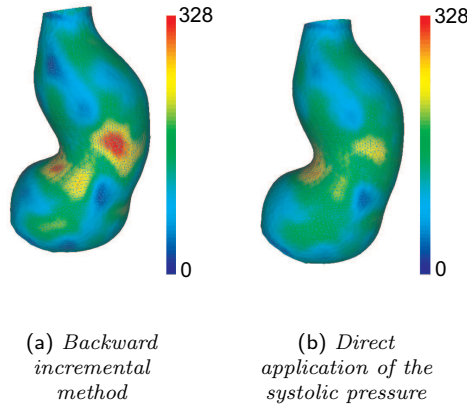


Figure 4.9: Von Mises stress (kPa) for aneurysm 3 at 120 mm Hg.

4.4 Discussion

The peak wall stress and strain via the backward modelling approach were significantly higher than in the classical approach for all three tested AAAs. The explanation is that the geometry tends to become locally smoother when a higher load is applied. In our method, the extra load applied to the measured diastolic geometry after computing the initial stress is only 40 mm Hg, whereas it is 120 mm Hg in the classical approach. This means that the high-curvature areas in the measured diastolic geometry will better retain their curvature in the backward approach than in the classical approach. It has been shown that high local curvature may lead to an elevation in the local wall stress [32, 91]. Therefore, it is likely that the higher peak wall stress with the backward approach is at least partially due to this higher curvature.

There are still several simplifications in our model. First of all, we assume that there is no residual wall stress in the unloaded AAA geometry. As yet, there is no method known that computes these residual stresses for a realistic AAA. High residual stresses might affect the accuracy of our method. We used idealised values for the material properties, the pressure and the wall thickness and we neglected the influence of the intra-luminal thrombus, which is still rather controversial.

We used a constitutive model for the AAA wall which assumes a linear stress-strain relation, while it has been reported that the true behaviour of the AAA wall is both geometrically and materially non-linear [85, 111, 119]. Other publications on material models for vascular structures have investigated the non-linear influence of fiber distributions, which may also be important for the AAA wall [30, 31, 118]. The shear modulus we used is based on the working area of the stress-strain curve

and thus to the stiffness of the deformed geometry at the diastolic pressure. With a material model with a nonlinear stress-strain relation the tissue becomes stiffer when it experiences strain. This means that the deformations that we compute between the initial geometry and the reference geometry are most probably too small, since a non-linear stress-strain relation would cause the material to be weaker in the regime between the unloaded and the reference geometry. Thus, using a more sophisticated material model would most likely lead to a smaller initial geometry. The interesting configuration is, however, the maximally loaded geometry from which the peak pressure is derived, which is the clinically important parameter for AAA. It is unlikely that the equilibrium stress in the loaded reference configuration is affected very much by the assumption of the linear stress-strain relation, since the stress for this relatively thin-walled structure will mainly be dictated by the pressure and the shape of the AAA. The displacements between the measured diastolic reference geometry and the maximally loaded systolic geometry will generally be smaller than the displacements between the reference geometry and the initial geometry. Also, in this part of the regime, the assumption of linearity of the stress-strain curve is more valid. Therefore, the expected influence of using the neo-Hookean model for the predicted peak stress is expected to be limited.

Even with the neo-Hookean material model, the influence of incorporating the initial loads will depend on the material stiffness, which inhibits a large amount of uncertainty and which is most likely not the same everywhere in the diseased vessel wall [111]. If a model based on a nonlinear stress-strain relation is employed or if fibers are included, there are even more parameters for which the exact values are unknown, which makes the outcome less predictable and less transparent. It is likely that the precise influence of incorporating the initial loads will be more dependent on the compliance of the AAA, which may vary from patient to patient, than on the material model used for the AAA wall.

Raghavan et al. [87] have previously investigated the influence of using a more realistic unloaded geometry of AAA for the wall stress. However, their model is based on the assumption that the backward deformation field is linearly related to the forward deformation field through a single factor. In our simulations we do not make such a simplification and the computed deformation fields are in fact not linearly related. Furthermore, their previous study is based on a single AAA geometry which has been obtained with ungated CT instead of a gated method, which is essential to obtain the correct diastolic geometry. Also, the volume ratio between the zero pressure configuration in this work of Raghavan et al. is a fixed input parameter of the model, which is based on a cadaver study of two AAAs. In our method we can use the patient-specific blood pressure to predict the initial geometry, so we do not rely on population means. On the other hand, the constitutive model employed in the paper of Raghavan et al. is more advanced than the linear stress-strain relation that we have assumed. The increase of the peak wall stress reported in this previous work is only 3.5%, which is less than the increase that we have witnessed in our simulations. These differences could be due to the constitutive model, the different method to approximate the initial geometry or differences in

the imaging and segmentation method. Since it appears that the local curvature becomes more important when the true initial geometry is used, the segmentation method and the amount of smoothing applied may be important for the predicted peak wall stress.

Another similar study has been presented by Lu et al. [67]. In that work the focus is on cerebral aneurysms, which is a different application area, and there is no comparison between the peak wall stress with the traditional approach and with the correct initial geometry.

A possible alternative method to compute the equilibrium stress on the diastolic geometry might be to first assume a high shear modulus and then compute the stress at the reference diastolic pressure, $\hat{\boldsymbol{\sigma}}$. Because of the high stiffness the pressurised geometry will stay approximately the same as the reference geometry. The equation of motion in the presence of body forces reads

$$\operatorname{div}(\boldsymbol{\sigma}) = \mathbf{f}. \quad (4.16)$$

The computed initial stress $\hat{\boldsymbol{\sigma}}$ can be introduced in the simulation for the maximum load, with normal stiffness, by continuously applying a body force of $\mathbf{f} = -\operatorname{div}(\hat{\boldsymbol{\sigma}})$. We have also used this approach and performed the simulations for the uniaxial deformation of a cube and the inflation of a cylinder. The resulting stress fields were found to be similar to the stress computed with the backward incremental method, but convergence was generally poor. Because of the additional disadvantage that this method does not directly provide a deformation field to Υ_o , and therefore also does not provide a simple approximation of the wall strain, we did not pursue this approach any further.

For all the test simulations that we performed, the initial geometry could be well replicated by application of the backward method on the reference geometry, indicating that this method is suitable for an improved modelling of AAA wall stress. The classical modelling approach does not only lead to an overestimation of the maximum aneurysm volume, but also to an underestimation of the wall curvature and the wall stress. The backward incremental approach overcomes these problems and leads to a more realistic systolic geometry and an assumably better estimate of the peak wall stress, which might lead to a better rupture predictor.

Sensitivity of peak wall stress in abdominal aortic aneurysm to geometrical variations

Abstract

Finite element method based simulations of patient-specific wall stress in abdominal aortic aneurysm (AAA) may provide a more accurate rupture risk predictor than the currently used maximum transverse diameter. For these simulations, the patient-specific AAA shape must be reconstructed from medical images, which may lead to uncertainties with respect to the exact geometry. In this study, we have investigated the sensitivity of the wall stress in AAA with respect to these aspects. We have acquired MR and CT images for four patients with AAA. Three individual users have delineated the AAA outer wall contours on the image slices, which were used to generate new synthetic images with ideal features for segmentation. We generated multiple segmentations based on the manual contours from one single user with a 3-dimensional active object (3DAO) at various parameter settings to estimate the influence of segmentation inaccuracies on the wall stress. The synthetic images for the different users were segmented with parameter settings allowing a sufficient level of reproducibility to investigate the influence of the user variability. We also investigated whether the variations we observed could be diminished by applying subsequent smoothing on the segmented AAA surfaces. For sufficiently smooth models of the AAA wall, the peak wall stress is reproducible for three out of the four AAA geometries. The 0.99 percentiles of the wall stress show excellent reproducibility. The variations induced by user variability are larger than the errors caused by the segmentation variability. Also, these errors can no longer be accounted to very local effects only. Although subsequent smoothing may reduce the variations caused by uncertainties in the geometry, this may also lead to new, systematic errors. We conclude that the peak wall stress in AAA is sensitive to small geometrical variations. To increase reproducibility it appears to be best not to allow too much detail in the simulations. This could be achieved either by using a sufficiently smooth geometry representation or by using a more robust statistical parameter derived from the wall stress distribution.

5.1 Introduction

Wall stress simulations on abdominal aortic aneurysms (AAA) have been widely recognised to provide an indication of rupture risk on a patient-specific basis [37, 38, 86, 110, 120, 125]. Fillinger et al. [38] have actually shown that wall stress can have a higher discriminatory value than the currently used maximum transverse AAA diameter.

The aneurysm shape, particularly the local curvature, has an important influence on the wall stress distribution [32, 123]. Other potentially important parameters are the patient's blood pressure, the local wall thickness and variations in the wall material properties. The correct approach for modelling the influence of intraluminal thrombus is still controversial. Modelling the thrombus as an elastic medium leads to a diminished load on the vessel wall [27]. Clinical studies, however, indicate that the pressure at the aneurysmal wall is not affected by the presence of thrombus [95, 112].

Non patient-specific values are often used for the wall thickness and the material properties, since these model parameters cannot easily be assessed on a patient-specific basis. The value used for the maximum pressure is either the monitored systolic pressure [37, 38, 86, 120, 125] or a non patient-specific systolic value [110].

For patient-specific wall stress simulations, the shape has to be reconstructed from medical images. So far, most studies have been based on non-cardiac triggered CTA, which implies that the geometry is a non-trivial average of the systolic and the diastolic configuration. In chapter 4 of this thesis, we have shown the importance of using the correct unloaded geometry from cardiac gated images for accurate peak wall stress estimates. Since cardiac triggered CT is not yet widely available, this method so far relies on MRA. The segmentation method and the modelling method we use for the construction of the computational model of AAA is based on deformable models and has been described in chapters 2 and 3.

In this chapter we investigate the geometrical sensitivity of the computed peak wall stress in AAA. Previous work on reproducibility and sensitivity of computational methods on patient-specific data has mostly focussed on flow and wall shear stress. Thomas et al. [108] have investigated the reproducibility of the geometry, flow rates and wall shear stress in MR-based models of the human carotid bifurcation. The results of this work indicate that even though the geometrical variation is limited, the variation in the computed time averaged wall shear stress is considerable, up to 37%. Other flow-related sensitivity studies based on MR have been conducted by Moore et al. In [71] and [73] the main conclusion is that smoothing may be essential for accurate estimation of wall shear stress. In [72] an error of up to 35% is reported in the computed wall shear stress for MR-based models of aortoiliac bifurcations in rabbits.

There are several sources for geometrical variation in reconstructed finite element meshes based on image data. First of all the choice of imaging modality and the imaging parameters can influence an object's appearance on medical images. In general, CTA has superior contrast and resolution, but suffers from a poor feature

for the outer AAA wall [79, 104]. The resolution and signal-to-noise ratio of MR is limited, resulting in significant partial volume and feature uncertainty for complex shapes such as AAAs.

A second cause of geometrical errors is the method used to segment the image and to reconstruct the object from the segmentation result. An often employed method to reconstruct computational domains from images is to first segment contours on the image slices and to fit a model of the object through these contours [37, 84, 94]. A drawback of this approach is that the influence of variations in the image features or delineated contours in the segmentation on the wall stress is affected, usually dampened, by the model representation making it impossible to truly measure the influence of these variations. To overcome this problem in our study, we have used deformable models to segment the images. This approach allows us to generate finite element meshes that are very close to the segmented object, without using any specific prior shape assumptions about the object that is being reconstructed, apart from those resulting directly from the parameter settings of the deformable surface.

The third source of variation is the uncertainty of the objects representation in the medical image, which may be judged differently by different observers. Automatic methods often use shape assumptions and operate on a limited set of features, which may also lead to errors with respect to the human observers.

Hardware phantoms can only provide realistic bounds for variations if the issues and inaccuracies involved in the segmentation, reconstruction and numerical simulations for these phantoms are similar to the ones encountered in practice. To overcome this limitation we have based our study on four realistic, very different AAA shapes by generating software phantoms based on the manual delineations of medical images by three users.

5.2 Methods

5.2.1 Curvature

First, we will briefly revisit the basic principles of the definition of a surface's curvature. The geometrical interpretation of this definition is depicted in figure 5.1. Let S be a smooth 2D manifold embedded in \mathbb{R}^3 . For any point $p \in S$, with coordinates \mathbf{x}_p and normal \mathbf{n}_p , a family of planes $\Pi(\mathbf{n}_p, \theta)$ can be constructed such that \mathbf{n}_p lies within Π . The parameter θ can be interpreted as the angulation of Π around \mathbf{n}_p with respect to a fixed reference point that is not on \mathbf{n}_p . Every plane $q_\theta \in \Pi$ defines an intersection contour $\alpha_\theta = q_\theta \cap S$, for which $p \in \alpha_\theta$. With the contour α_θ we can construct an arc $\beta_\theta(s)$ such that $\beta_\theta(0) = \mathbf{x}_p$ and $d/ds(\beta_\theta(s))|_{s=0} = \mathbf{t}_\theta$, with $\|\mathbf{t}_\theta\| = 1$. The normal curvature in the direction of \mathbf{t}_θ , $\kappa_p(\mathbf{t}_\theta)$ can now be defined through

$$\left. \frac{d^2 \beta_\theta(s)}{ds^2} \right|_{s=0} = \kappa_p(\mathbf{t}_\theta) \mathbf{n}_p. \quad (5.1)$$

The *principal curvatures* κ_p^1 and κ_p^2 are defined as the minimum and maximum normal curvature at p . The *principal directions* related to these respective curvatures, t_p^1 and t_p^2 , form an orthonormal basis for the tangent space to S at p [40, 81, 106, 109]. The principal curvatures are equal to the reciprocals of the maximum and minimum radii of the circles described by the arcs β_θ . The *Gaussian curvature* is defined as the product of the two principal curvatures and the *mean curvature* is defined as their average.

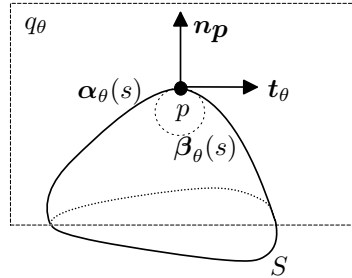


Figure 5.1: Definition of the normal curvature on a smooth manifold.

5.2.2 Images

CT and MR images have been acquired for four patients with AAA who were awaiting surgery. The time periods between the MR and CT scans were 0 days, 40 days, 16 days, and 25 days, respectively. The relevant MR imaging parameters have been described in chapter 2, section 2.2. The contrast-enhanced CT images have a resolution of $0.6 \times 0.6 \times 3 \text{ mm}^3$. Three users have manually delineated the contours of the outer vessel wall between the branching with the renal arteries and the bifurcation into the iliac arteries on both the MR and the CT images. The manual contours have been used to generate new synthetic images with a pixel value of 100 for the AAA region and 0 for the background. The partial volume effect was mimicked by first generating these synthetic images at a five times higher resolution and down-sampling these images to the original resolution by taking the average grey value of the high resolution voxels enclosed in the low resolution voxels. An example of a manual contour and a synthetic image for the MR acquisitions is shown in figure 5.2.

5.2.3 Deformable model

The 3D active objects (3DAO) implementation we used for the segmentation simulations is based on the work by Delingette [24] and has been previously used for segmentation of vascular structures, including AAA [23, 41, 79]. The 3DAO is a collection of connected non-planar simplex faces in which every 3DAO simplex node has exactly three neighbour vertices. The surface can be iteratively deformed

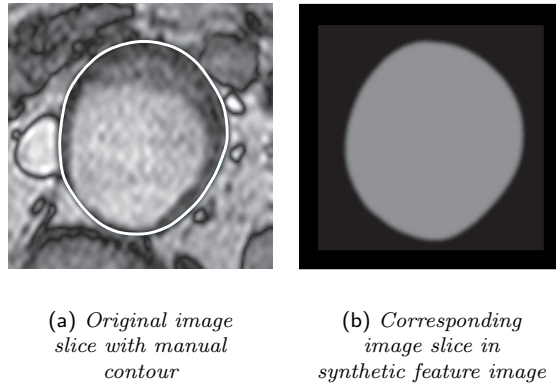


Figure 5.2: Generation of synthetic MR feature images based on manual segmentations of the AAA outer wall.

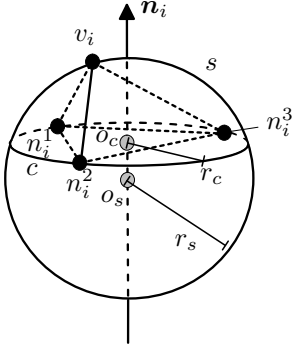
based on fictitious forces computed from the image features and shape regularisation forces. The new position for a node is determined at every iteration from the current position via a time-discretised second-order Newtonian-evolution equation

$$\mathbf{P}_i^{t+1} = \mathbf{P}_i^t + (1 - \gamma) (\mathbf{P}_i^t - \mathbf{P}_i^{t-1}) + \alpha \mathbf{F}_{int} + \beta \mathbf{F}_{ext}, \quad (5.2)$$

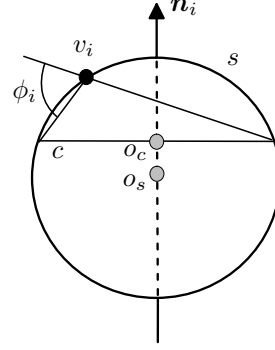
where \mathbf{P}_i^t denotes the position of the i -th simplex node at iteration t . With \mathbf{F}_{int} and \mathbf{F}_{ext} we denote the internal force (ensuring smoothness) and the external force (fitting the node to image features) respectively. The parameters α and β denote the respective weighting coefficients of these forces and γ is a damping coefficient used to stabilise the deformation process. In the segmentations presented in this chapter we used $\gamma = 0.8$.

The synthetic images described in section 5.2.2 have been segmented with 3DAO using a threshold force, which pushes a 3DAO node outwards when the local intensity value is higher than the threshold and inwards when the local intensity value is below the threshold value. To account for the highly orthotropic voxel size in the image data, the external forces are only imposed on vertices that are within a user defined distance of an imaging plane. In the segmentations presented in this chapter, this distance criterion was set to 0.25 times the slice distance. For the approximation of the local image intensity at the 3DAO vertices we used bi-linear interpolation in the closest imaging plane, thus obtaining sub-pixel accuracy. For these segmentations we used the full-width at half maximum criterion [51], resulting in a threshold of 50.

The internal forces we used for the segmentation are based on a regularisation approach that is aimed at making the estimated local surface curvature at a vertex equal to the curvatures of the three neighbouring vertices [24]. Let v_i be a simplex node with neighbours n_i^1 , n_i^2 and n_i^3 , as depicted in figure 5.3. These four nodes



(a) Construction of the sphere s and the circle c from the local tetrahedron formed by v_i and its neighbours



(b) Computation of ϕ_i within the plane defined by o_c , o_s and v_i

Figure 5.3: Computation of the simplex angle ϕ_i for the internal force calculation in the deformation process of the 3DAO.

uniquely define a sphere s , with radius r_s and center o_s . Let P_i denote the plane defined by the neighbour nodes, with normal \mathbf{n}_i , and let $c = P_i \cap s$ denote the intersecting circle of this plane and the sphere, with center o_c . The radius of this circle will be denoted by r_c . Let \mathbf{d}_i denote the vector from o_s to o_c . Let the vector from v_i to n_i^1 be denoted by \mathbf{x}_i . The simplex angle ϕ_i is defined through the relations

$$\sin(\phi_i) = \frac{r_c}{r_s} \text{sign}(\mathbf{x}_i \cdot \mathbf{n}_i), \quad \cos(\phi_i) = \frac{\|\mathbf{d}_i\|}{r_s} \text{sign}(\mathbf{d}_i \cdot \mathbf{n}_i), \quad -\pi \leq \phi \leq \pi. \quad (5.3)$$

The mean curvature h_i may be estimated from the simplex angle as

$$h_i = \frac{\sin(\phi_i)}{r_c}. \quad (5.4)$$

The 3DAO is initialised with a small tubular simplex mesh around an automatically tracked centre line in the feature image. To allow for the shape changes necessary to come from this initial shape to the larger AAA shape, the mesh is refined during the deformation process by splitting faces based on a size criterion. For the termination of the segmentation process we used the relative change of the enclosed volume of the 2-simplex surface. The deformation process is halted if the relative change in volume is below 0.001 for two subsequent iteration steps. The resampling of the faces in the iteration process may destabilise the deformation process. To come to a stable deformation in the final stages, the deformation process is restarted after the initial convergence without the refinement option until the convergence criterium is matched again.

5.2.4 Normal vector voting

For the approximation of the curvature of the segmented AAAs we have used the normal voting approach of Page et al. [81] on the curvature corrected dual triangulation of the 2-simplex mesh (see Section 3.2.3). For completeness' sake we briefly describe the essentials of this approach and our implementation choices. For a full description the reader is referred to the original article. Let n denote the number of edges in the mesh and let l_k , $1 \leq k \leq n$ denote the length of the k -th edge. For each vertex v in the triangulation, with coordinates \mathbf{x}_v , a geodesic neighbourhood N_v is determined with a fast-marching approach. The size of the geodesic neighbourhood is based on a user-defined factor f and the average edge length through

$$S_g = \frac{f}{n} \sum_{k=1}^n l_k. \quad (5.5)$$

A triangle is considered to be part of N_v if the geodesic distance of all triangle vertices is smaller than S_g . Let the triangles in N_v be denoted by t_i , $1 \leq i \leq m$, the triangles centers of gravity by c_i , with coordinates \mathbf{c}_i , and the triangle normals by \mathbf{n}_i . For each plane $p_i = p_i(\mathbf{x}_v, \mathbf{s}_{i,v})$, with $\mathbf{s}_{i,v} = \mathbf{n}_i \times (\mathbf{x}_v - \mathbf{c}_i)$, the in-plane circular arc \mathbf{a}_i is constructed, connecting c_i and v such that the tangent of \mathbf{a}_i at c_i is normal to \mathbf{n}_i . The normal vote \mathbf{w}_i for the estimated normal at v of triangle t_i is the vector that is normal to \mathbf{a}_i at v and lies within p_i , as depicted in figure 5.4. The l votes \mathbf{w}_i for the normal at v are collected in a weighted sum of covariance matrices

$$V = \sum_{i=1}^l h_i \mathbf{w}_i \mathbf{w}_i, \quad (5.6)$$

where the weight h_i is based on an exponential decay with the geodesic distance g_i between c_i and v

$$h_i = \frac{A_i}{A_m} e^{-\frac{g_i}{\sigma}}, \quad (5.7)$$

with A_i the area of triangle t_i , A_m the maximum triangle area in the mesh, and σ a parameter controlling the rate of decay. For the curvature estimates on the triangulated meshes we have used $\sigma = S_g/3$ resulting in a negligible influence of points over the geodesic boundary. The estimate for the normal \mathbf{n}_v at vertex v is the eigenvector of V corresponding to the largest eigenvalue. The original design in Page et al. [81] uses saliency maps to classify the mesh vertex in order to correctly deal with corners and creases. However, in our application we only calculate the curvature at regular parts of the AAA wall, where these structures are not expected. For the final estimation of the curvature, Page et al. have adapted the method proposed by Taubin [106] by extending it to geodesic neighbourhoods instead of 1-ring neighbourhoods. Let M_p denote the symmetric matrix defined through

$$M_p = \frac{1}{2\pi} \int_{-\pi}^{\pi} \kappa_p(\mathbf{t}_\theta) \mathbf{t}_\theta \mathbf{t}_\theta d\theta. \quad (5.8)$$

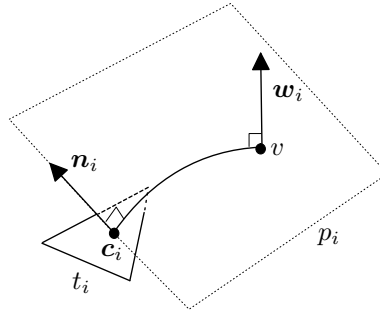


Figure 5.4: Normal voting scheme.

The eigenvectors for the non-zero eigenvalues of this matrix are in fact the principal directions \mathbf{t}_p^1 and \mathbf{t}_p^2 , and the eigenvalues m_1 and m_2 are related to the principal curvatures through

$$\kappa_p^1 = 3m_1 - m_2, \quad (5.9)$$

$$\kappa_p^2 = 3m_2 - m_1. \quad (5.10)$$

Let v be a vertex of the triangulated representation of S , with coordinates \mathbf{x}_v . For each vertex v_i , with coordinates \mathbf{x}_i in the geodesic vertex neighbourhood N_v of vertex v the vector $\mathbf{v}_i = \mathbf{x}_i - \mathbf{x}_v$ is projected onto the tangent plane of S at p and the result is normalised through

$$\mathbf{k}_i = \frac{\mathbf{l}_i}{\|\mathbf{l}_i\|}, \quad \mathbf{l}_i = \mathbf{v}_i - \mathbf{n}_v \cdot \mathbf{v}_i \mathbf{n}_v. \quad (5.11)$$

To incorporate the distance of v_i to v in the vote, again the exponential decay from (5.7) is used, but now without the area factor A_i/A_m . Furthermore, the weights w_i are constrained with $\sum_{i:v_i \in N_v} w_i = 2\pi$, in order to maintain translation invariance. The computation of the normal curvatures κ_i is based on the ratio of the changes in turning angle τ_i and the changes in arc length, which are approximated with the geodesic distance g_i between v and v_i

$$\kappa_i = \frac{\tau_i}{g_i}. \quad (5.12)$$

The changes in turning angle τ_i are based on the changes of the normal when traversing the surface over the normal curve. Let $\mathbf{p}_i = \mathbf{n}_p \times \mathbf{k}_i$ and let

$$\mathbf{n}_p^i = \frac{\mathbf{n}_i - \mathbf{p}_i \cdot \mathbf{n}_i \mathbf{p}_i}{\|\mathbf{n}_i - \mathbf{p}_i \cdot \mathbf{n}_i \mathbf{p}_i\|}. \quad (5.13)$$

Now the change in turning angle is computed from $\tau_i = \arccos(\mathbf{n}_p \cdot \mathbf{n}_p^i)$. Finally the curvature at vertex is computed by approximating the matrix from (5.8) by

$$M_v = \frac{1}{2\pi} \sum_{i:v_i \in N_v} w_i \kappa_i \mathbf{k}_i \mathbf{k}_i. \quad (5.14)$$

With an eigen analysis of M_v , providing estimates for m_1 and m_2 , the curvature estimate can be computed using (5.9,5.10).

5.2.5 Smoothing scheme

For the smoothing and regularisation of the 2-simplex meshes resulting from the segmentation process we have used the method proposed by Tohka [113]. This approach is based on the unique dependency of the position of a node in an ideal spherical 2-simplex mesh on the position of its three neighbours. Let \mathbf{s}_i , $1 \leq i \leq n$ denote the vertex positions in a spherical 2-simplex mesh S^o , and let $\hat{\mathbf{s}}_i = \mathbf{s}_i - 1/n \sum_{j=1}^n \mathbf{s}_j$. In this mesh, every vertex satisfies

$$\hat{\mathbf{s}}_i = \alpha \sum_{j \in N_i} \hat{\mathbf{s}}_j, \quad (5.15)$$

with

$$\alpha = \left(3 \cos \left(2 \arctan \left(\frac{2\sqrt{\pi\sqrt{3}}}{3\sqrt{n}} \right) \right) \right)^{-1}. \quad (5.16)$$

Based on this relation the smoothing process can be represented as the minimisation of a cost function based on the initial shape and the deviation from (5.15)

$$f(S|S^o) = \sum_{i=1}^n \left(\|\mathbf{s}_i - \mathbf{s}_i^o\|^2 + \lambda \|\hat{\mathbf{s}}_i - \sum_{j \in N_i} \hat{\mathbf{s}}_j\|^2 \right), \quad (5.17)$$

where λ balances the amount of smoothing and the accuracy of the approximation of the original shape. The minimisation problem is solved with a gradient-descent method with learning parameter η . For all the examples presented in this text we used a learning rate of $\eta = 0.4/\lambda$, providing robust convergence.

5.2.6 Wall model

Constitutive wall model

For the AAA wall we use the neo-Hookean model describing an isotropic elastic medium with large deformations. We consider an incompressible elastic medium in the time dependent domain $\Omega(t) \subset \mathbb{R}^3$, bounded by $\Gamma(t) = \partial\Omega(t)$, with outward normal \mathbf{n} . Let \mathbf{F} be the deformation gradient tensor

$$\mathbf{F} = \frac{\partial \mathbf{x}}{\partial \mathbf{X}}, \quad (5.18)$$

with \mathbf{X} the reference configuration and $\mathbf{x} = \mathbf{x}(\mathbf{X}, t)$ the current configuration. In the absence of body forces, the equations of motion and continuity from continuum mechanics are

$$\operatorname{div}(\boldsymbol{\sigma}) = \mathbf{0} \quad \text{in } \Omega, \quad (5.19)$$

$$\det(\mathbf{F}) = 1 \quad \text{in } \Omega. \quad (5.20)$$

The Cauchy stress for an incompressible elastic medium reads

$$\boldsymbol{\sigma} = -p\mathbf{I} + \boldsymbol{\tau}, \quad (5.21)$$

with p the hydrostatic pressure, \mathbf{I} the identity and $\boldsymbol{\tau}$ the extra stress resulting from deformations. For a neo-Hookean material, we have $\boldsymbol{\tau} = G(\mathbf{B} - \mathbf{I})$, with G the shear modulus and $\mathbf{B} = \mathbf{F} \cdot \mathbf{F}^T$ the Finger tensor.

The set of equations is completed with boundary conditions on each part of the domain boundary $\Gamma_k(t)$, with $\bigcup_k \Gamma_k(t) = \Gamma(t)$, and $\Gamma_k(t) \cap \Gamma_l(t) = \emptyset$, $\forall k \neq l$. The Dirichlet boundary conditions, which explicitly fix the displacement on the boundary read

$$\mathbf{x} \cdot \mathbf{n} = x_n, \quad (5.22)$$

$$\mathbf{x} \cdot \mathbf{t}_i = x_{t_i}, \quad \mathbf{n} \cdot \mathbf{t}_i = 0, i \in \{1, 2\}, \quad (5.23)$$

where \mathbf{t}_1 and \mathbf{t}_2 are linearly independent vectors. The Neumann boundary conditions, in which the surface traction $(\boldsymbol{\sigma} \cdot \mathbf{n})$ in the normal and tangential direction is prescribed read

$$(\boldsymbol{\sigma} \cdot \mathbf{n}) \cdot \mathbf{n} = s_n, \quad (5.24)$$

$$(\boldsymbol{\sigma} \cdot \mathbf{t}_i) \cdot \mathbf{t}_i = s_{t_i}, \quad \mathbf{n} \cdot \mathbf{t}_i = 0, i \in \{1, 2\}, \quad (5.25)$$

A special case occurs when $s_n = 0$. This situation is referred to as a stress-free boundary condition.

Weak formulation

Let $W = \left\{ \mathbf{w} \in [H_o^1(\Omega)]^3 \right\}$, with $H_o^1(\Omega)$ the functional Hilbert space of functions f that satisfy the Dirichlet condition $f|_\Gamma = 0$ and let $Q = \{q \in L^2(\Omega)\}$. With substitution of the Neumann boundary conditions and partial integration, the weak formulation of equations (5.19) and (5.20) becomes

$$\int_{\Omega(t)} (\nabla \mathbf{w})^T : \boldsymbol{\sigma} d\Omega = \int_{\Gamma(t)} \mathbf{w} \cdot (\boldsymbol{\sigma} \cdot \mathbf{n}) d\Gamma, \quad \forall \mathbf{w} \in W, \quad (5.26)$$

$$\int_{\Omega(t)} q(\det(\mathbf{F}) - 1) d\Omega = 0, \quad \forall q \in Q. \quad (5.27)$$

The notation " : " is used to denote the 3D double dot product $\mathbf{A} : \mathbf{B} = \text{tr}(\mathbf{A} \cdot \mathbf{B})$. Let $\Omega_n := \Omega(t_n)$ and $\Gamma_n := \Gamma(t_n)$. To evaluate the integrals in (5.26) and (5.27) over the domain (Ω_n, Γ_n) , we use the updated Lagrange approach, which implies that the previous configuration $(\Omega_{n-1}, \Gamma_{n-1})$ is taken as the reference configuration for (Ω_n, Γ_n) . The gradient operator is also interpreted with respect to the previous configuration. With \mathbf{F}_i^n we will denote the deformation tensor from the domain Ω_i to the domain Ω_n . Similarly, we will denote the gradient operator with respect to the domain Ω_i with ∇_i . This way the total transformation from Ω_o to Ω_n becomes

$$\mathbf{F}_o^n = \mathbf{F}_{n-1}^n \cdot \mathbf{F}_o^{n-1} = (\nabla_{n-1} \mathbf{x}_n)^T \cdot (\nabla_o \mathbf{x}_{n-1})^T. \quad (5.28)$$

It is customary in the updated Lagrange method to take the displacement field of the material points as the unknown. At time t_n , this field is defined through $\mathbf{u}_i(t_n) = \mathbf{x}_i(t_n) - \mathbf{x}_i(t_{n-1})$, where $\mathbf{x}_i(t_n)$ and $\mathbf{x}_i(t_{n-1})$ denote the position of a material point at two subsequent points in time.

When writing $\nabla_n = (\mathbf{F}_{n-1}^n)^{-T} \cdot \nabla_{n-1}$ the weak form of the system (5.26,5.27) becomes

$$\int_{\Omega_{n-1}} (\nabla_{n-1} \mathbf{w})^T : (\mathbf{F}_{n-1}^n)^{-1} \cdot \boldsymbol{\sigma} J_{n-1}^n d\Omega_{n-1} = \int_{\Gamma_{n-1}} \mathbf{w} \cdot \mathbf{s} \tilde{J}_{n-1}^n d\Gamma_{n-1}, \quad (5.29)$$

$$\int_{\Omega_{n-1}} q(J-1) J_{n-1}^n d\Omega_{n-1} = 0, \quad (5.30)$$

where J_{n-1}^n and \tilde{J}_{n-1}^n are defined through $d\Omega_n = J_{n-1}^n d\Omega_{n-1}$ and $d\Gamma_n = \tilde{J}_{n-1}^n d\Gamma_{n-1}$. In equation (5.29), \mathbf{s} is defined by equations (5.24) and (5.25).

Finite-element formulation and solution strategy

To obtain a finite-element formulation of the system (5.29,5.30) the domain (Ω, Γ) is divided into non-overlapping discrete elements. Within each element, the physical unknowns are approximated with Lagrange interpolation polynomials.

At each time step, the non-linear algebraic system rendered from (5.29,5.30) is linearised with Newton's method and we iterate to obtain a converged solution. The linearised system at each iteration step is preconditioned with an incomplete LU decomposition and solved with the Bi-CGSTAB method [117]. For the simulations we used $Q_2^+ P_1$ tetrahedral elements (15 nodes), yielding a quadratic approximation. All of the simulations have been performed with the finite element code SEPRAN (Septra analysis, Delft, The Netherlands).

5.2.7 Simulations

Model validation

To validate the wall modelling approach we have performed a number of wall stress simulations for a cylindrical shape with an outer radius of 20 mm, a length of 100 mm and a wall thickness of 2 mm. First, we generated a mesh with the SEPRAN native mesh generator, resulting in an ideal cylindrical shape. This model was considered the golden standard. Next we started from a regular 2-simplex representation of a cylinder and generated a wall mesh employing the modelling and meshing techniques described in chapter 3. This model is considered as a test for the modelling and the meshing scheme, without taking into account segmentation errors. The final model is based on a 2-simplex representation of a cylinder generated by segmenting a feature image of the cylindrical shape with the deformable model. The average mesh resolution was 18 mm^2 and the internal and external force weights were equal. The shear modulus for all of these models was taken as 1.0 MPa and the upper and lower cross-sections were clamped in all directions. All models were loaded from the inside with a pressure of 16 kPa (120 mm Hg). We also applied the backward

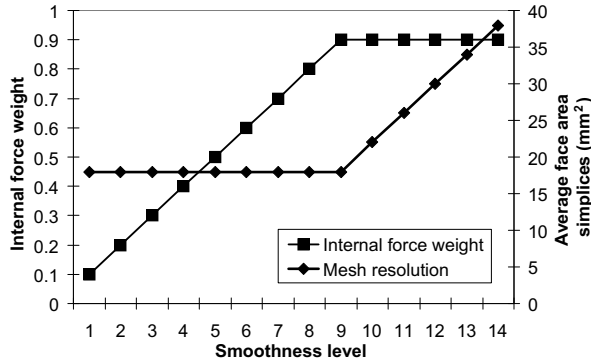


Figure 5.5: Realisation of smoothness levels through variation of the force weights balance and the mesh resolution. The external force weight equals one minus the internal force weight.

incremental method described in chapter 4 using a reference pressure of 10.7 kPa (80 mm Hg) and a final pressure of 16 kPa. Although the cylindrical shape is very basic in comparison to AAA geometries, this is a challenging test since the 2-simplex mesh structure is not well suited to approximate surfaces with a zero Gaussian curvature. To test the influence of the mesh we generated meshes at several resolutions for aneurysm 2. All resulting meshes were again used for simulations with and without the backward incremental scheme with the same settings as for the cylinders. In all representations of the results we have set the stress values to zero in a region of within 5 mm of the boundary planes to avoid any disturbance caused by unrealistic effects caused by the boundary conditions that we imposed.

Influence of segmentation inaccuracies

For the synthetic feature images, the segmentation process is performed at 14 smoothness levels, ranging from irregular simplex meshes to smooth simplex meshes. These smoothness levels were created by varying the force weight balance of the deformable surface model and the mesh resolution, as depicted in figures 5.5 and 5.6. For each of these smoothness levels, an initial segmentation has been created from the automatically tracked centre line by deforming with a threshold of 50 until the stopping criterium was met. Next we let the geometry shrink by adjusting the threshold to 95 and letting the model deform until the stopping criterium was matched again. Then, we re-segmented the AAA shape by setting the threshold to 50 again and letting the model deform again until the stopping criterium was matched. In the final stage of this last segmentation step, no mesh refinements were used to stabilise the deformation process. This shrinking and re-segmentation process was performed 10 times at each smoothness level, resulting in 140 segmentations for each of the four AAAs.

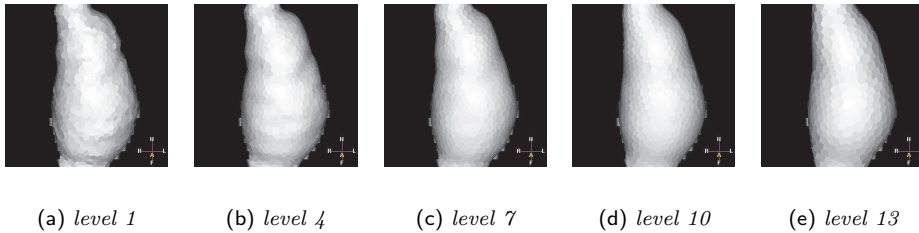


Figure 5.6: Segmentation examples for aneurysm 1 at several smoothness levels. See also figure 5.5.

We performed this variability estimation scheme for the feature images based on the manual segmentations of user 2. For each of the resulting segmentations, the 2-simplex surface was transformed to a triangulation with the curvature correction method presented in section 3.2.3. We computed the minimum and the maximum Gaussian curvature in the region delimited by the lowest and highest manually segmented slice in the feature images with the methods from Page et al., see section 5.2.4, using a geodesic distance of 2.5 times the average triangle edge length in the triangulated surface. For smoothness levels 5, 8 and 11 we selected the two segmentations with the highest variation in the Gaussian curvature, and we performed wall stress simulations both with the backward incremental method and with direct application of the maximum systemic pressure.

User-induced variability and modality induced variability

The results from the segmentation variability scheme indicated that the maximum variation in the peak wall stress was 11% for aneurysms 1, 3 and 4 at smoothness level 8, and that the variation in the 0.99 percentiles of the distribution of the stress values was small for all four aneurysms. A more detailed description of these results is provided in subsection 5.3.2. Here, these results are merely referred to as a motivation for the further methodology. We generated segmentations with these parameter settings for the input contours of the three different users both for the CT and the MR images and simulated the wall stress distribution with the backward incremental approach, again using a diastolic pressure of 80 mm Hg and a systolic pressure of 120 mm Hg.

The effect of sphere-shape based smoothing

To test the effect of subsequent smoothing of segmented simplex surfaces on the variations in the wall stress, we applied the smoothing method from [113] on aneurysms 1 and 2 at smoothness level 5 and on the image based cylinder model used for the model validation with $\lambda \in \{50, 100, 150\}$.

| Geometry source | Load method | | | |
|--------------------------|--------------------|-------|----------------------|-------|
| | Direct application | | Backward incremental | |
| | Peak wall stress | Error | Peak wall stress | Error |
| Native SEPRAN | 160 | | 154 | |
| Model simplex mesh | 166 | 4 | 166 | 8 |
| Image-based simplex mesh | 199 | 24 | 210 | 36 |

Table 5.1: Comparison of results of a load sequence on a cylinder. Maximum Von Mises wall stress in kPa and the errors as a percentage. For the model simplex mesh the errors in the estimated wall stress are limited. For the image based cylinder model, however, the errors in the peak wall stress are high.

| | Average face area | | |
|-----------------------------|--------------------|-------------------|-------------------|
| | 10 mm ² | 8 mm ² | 6 mm ² |
| Backward incremental method | 465 | 482 | 481 |
| Direct pressure application | 413 | 418 | 424 |

Table 5.2: Peak wall stress (Von Mises, kPa) in a segmented model of aneurysm 2 at several mesh resolutions. The influence of the mesh resolution is quite limited in this range.

The resulting geometries were used for wall stress simulations with the backward incremental method with parameters that were identical to those of the previous simulations.

5.3 Results

5.3.1 Model validation

Table 5.1 shows the maximum wall stress in a native SEPRAN model of a cylinder, in a 2-simplex model cylinder which has been transformed to a triangulated wall model and meshed with the methods from chapter 3, and in an image-based 2-simplex segmentation which has been modelled and meshed with the same techniques. The error in the peak wall stress for the model 2-simplex cylinder is 4% with direct application of the maximum pressure and 8% when the initial loads are taken into account. These results indicate that the errors that are directly related to the modelling approach are limited. The errors related to the geometrical errors in the segmentation of an image of a cylinder are, however, much larger. With direct application of the pressure the error is 24% and when the initial loads are taken into account, the error becomes 36%. Figure 5.8 shows the wall stress distribution on the inner cylinder wall for the three approaches. With the model 2-simplex cylinder the wall stress distribution is uniform as in the golden standard model. With the segmented cylindrical shape there are pronounced stress peaks that are most likely related to small irregularities in the segmented cylinder surface.

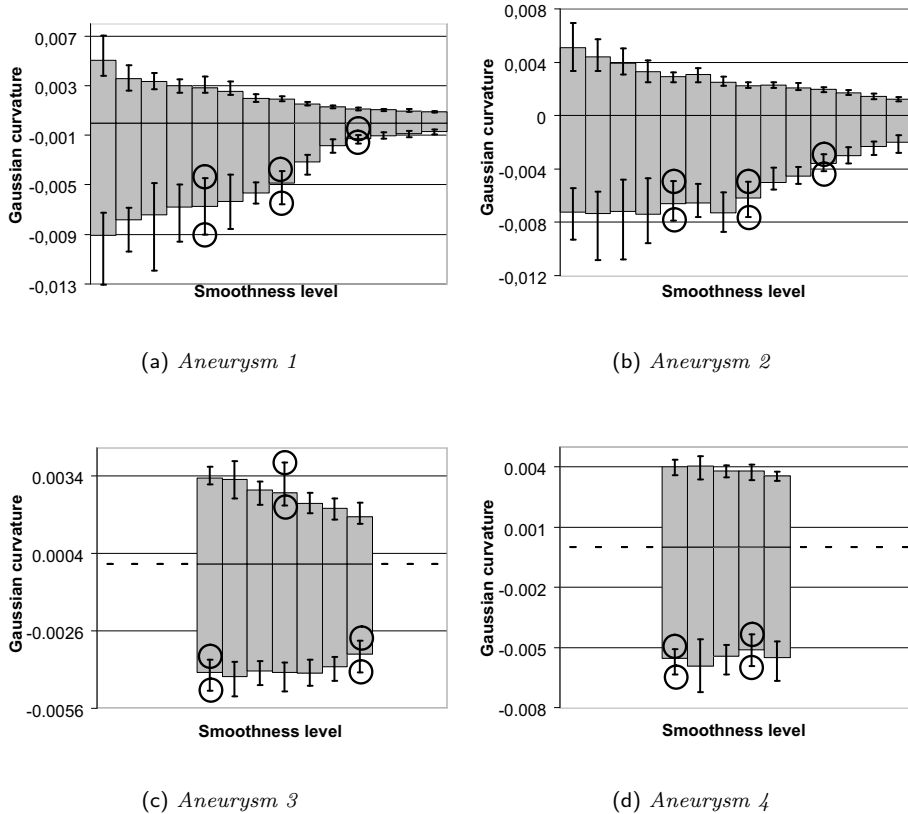


Figure 5.7: Curvature variations observed when segmenting four AAA geometries 10 times at several distinct parameter settings. The bars indicate the average minimum and maximum Gaussian curvatures. The whiskers indicate the greatest variation in the minimum and the maximum Gaussian curvature. The circles indicate segmentations that have been used for wall stress simulations.

5.3.2 Influence of segmentation inaccuracies

Table 5.2 shows the peak wall stress in a segmented model of aneurysm 2 at several mesh resolutions. The wall stress distribution on a part of the outer wall at the minimum and maximum mesh resolution is depicted in figure 5.9. The maximum variation in the peak wall stress is 4%, indicating that the mesh resolutions is sufficient, and moreover, that the mesh refinement methods and the element distribution have a very limited influence on the peak wall stress. For all of the simulations presented hereafter, we used a mesh resolution corresponding to an average face area of 6 mm^2 .

| Geometry | Smoothness level | | |
|------------|------------------|-----|-----|
| | 5 | 8 | 11 |
| Aneurysm 1 | 1.6 | 1.1 | 1.8 |
| Aneurysm 2 | 1.0 | 1.2 | 2.0 |
| Aneurysm 3 | 1.7 | 2.1 | 2.0 |
| Aneurysm 4 | 1.9 | 1.0 | - |

Table 5.3: *Maximum distances between the geometries used for the wall stress simulations for the segmentation variability study in mm.*

Figure 5.7 shows the variations in the minimum and the maximum Gaussian curvature for the segmentation variability simulations. The bars represent the average curvatures and the whiskers indicate the largest variation. For aneurysms 1 and 2 we performed the variability experiment at all 14 smoothness levels. However, for the lowest smoothness levels the resulting geometries could not be successfully used for wall stress simulations because of the highly irregular surface meshes. Therefore, for aneurysm 3 and 4 we did not perform the simulations at the lowest smoothness levels. Moreover, for aneurysm 4, the segmentation process failed for smoothness levels 11 and higher. The reason for this failure is that aneurysm 4 is smaller than the other geometries, implying that the mesh resolution is inadequate to follow the shape at this lower resolution level. The general trend for all geometries is that both the mean maximum and mean minimum Gaussian curvature, as well as the variation in these curvatures, decrease, even though this decrease is not always monotonous. In most cases the largest variation occurs in the minimum Gaussian curvature. Only for aneurysm 3 at smoothness level 8 the maximum Gaussian curvature inhibits the most variation.

Table 5.3 shows the distances between the segmentations that were selected from the segmentation variability experiment. These distances were computed by taking the distances from the nodes in one mesh to the faces in the other mesh and vice-versa. The maximum distances between the segmented surfaces are small, mostly below 2 mm, which is one third of the slice thickness.

Tables 5.4 and 5.5 respectively show the maximum and the 0.99 percentiles of the Von Mises wall stress. The 0.99 percentiles were computed by considering the distribution of the wall stress values in the mesh nodes themselves. Since the element sizes are similar over the entire wall geometry, this results in a uniform sampling of the stress values in the geometry. For aneurysms 1, 3 and 4, the variation in the computed peak wall stress diminishes as the smoothness level increases. At level 8, the variations for these geometries are 1%, 11% and 0% respectively when taking the initial loads into account and 2%, 5% and 3% respectively when not taking the initial loads into account. At smoothness level 5 these variations are significantly larger, up to 27%. The variation in the 0.99 percentile value of the Von Mises wall stress is remarkably stable. For all four AAA geometries at all three smoothness levels, the variation in this parameter is limited to 6% with both methods.

For aneurysm 2, the variations in the maximum wall stress are large at all smooth-

| | Smoothness level / segmentation number | | | | | |
|------------|--|-----|-----|-----|------|------|
| | 5/1 | 5/2 | 8/1 | 8/2 | 11/1 | 11/2 |
| Aneurysm 1 | 441 | 435 | 414 | 417 | 392 | 414 |
| Aneurysm 2 | 470 | 595 | 465 | 601 | 475 | 716 |
| Aneurysm 3 | 359 | 493 | 391 | 351 | 316 | 284 |
| Aneurysm 4 | 238 | 219 | 191 | 190 | - | - |

(a) *Maximum wall stress with the backward incremental method*

| | Smoothness level / segmentation number | | | | | |
|------------|--|-----|-----|-----|------|------|
| | 5/1 | 5/2 | 8/1 | 8/2 | 11/1 | 11/2 |
| Aneurysm 1 | 324 | 399 | 293 | 298 | 292 | 295 |
| Aneurysm 2 | 423 | 485 | 475 | 371 | 433 | 370 |
| Aneurysm 3 | 279 | 349 | 279 | 264 | 237 | 240 |
| Aneurysm 4 | 193 | 209 | 178 | 184 | - | - |

(b) *Maximum wall stress with direct application of pressure*

Table 5.4: *Simulated maximum Von Mises stress in kPa from the segmentation reproducibility study for four AAAs. For aneurysm 1, 3 and 4 the stresses are reproducible at smoothness level 8, within 11% variation. At smoothness level 11, this variation is even less. For smoothness level 5, the variations are larger. For aneurysm 2, no reproducibility could be established at any smoothness level (see also figure 5.10). The variation in the 0.99 percentiles of the wall stress distribution is very limited for all four AAAs. The sensitivity with the backward incremental method is generally slightly worse than with direct, forward application of the maximum pressure.*

ness levels both with and without the initial loads method. This aneurysm has an uncommon shape, as can be observed in figure 5.10. The vessel has kinked in the middle section, thus creating an inward folded region with strong negative Gaussian curvature, i.e. a saddle point. This region is also the region where the maximum in the wall stress occurs for all segmentations of this aneurysm, and it is also a region with relatively large segmentation errors, as indicated in figure 5.10(a). Although the saddle point region has high wall stress for all segmentations, the nature of this maximum differs for the different segmentations. In figure 5.10 we have plotted the wall stress distributions for both simulations at smoothness level 11. In figure 5.10(c), there is one single maximum with a high stress value. In figure 5.10(b) high wall stress occurs in the same region, but this time there are three distinct spots with a similar high value, which is lower than for the other segmentation. Similar behaviour occurs for the other smoothness levels.

Table 5.6 shows the distance between the location of the maxima for the different segmentations. For high smoothness levels, large distances occur between the loca-

| | Smoothness level / segmentation number | | | | | |
|------------|--|-----|-----|-----|------|------|
| | 5/1 | 5/2 | 8/1 | 8/2 | 11/1 | 11/2 |
| Aneurysm 1 | 309 | 297 | 280 | 277 | 276 | 277 |
| Aneurysm 2 | 270 | 284 | 279 | 293 | 338 | 319 |
| Aneurysm 3 | 232 | 238 | 230 | 221 | 218 | 215 |
| Aneurysm 4 | 171 | 168 | 156 | 158 | - | - |

(a) 0.99 percentiles of wall stress with the backward incremental method

| | Smoothness level / segmentation number | | | | | |
|------------|--|-----|-----|-----|------|------|
| | 5/1 | 5/2 | 8/1 | 8/2 | 11/1 | 11/2 |
| Aneurysm 1 | 263 | 258 | 249 | 251 | 249 | 249 |
| Aneurysm 2 | 255 | 265 | 263 | 265 | 272 | 268 |
| Aneurysm 3 | 212 | 213 | 203 | 203 | 196 | 195 |
| Aneurysm 4 | 160 | 162 | 154 | 153 | - | - |

(b) 0.99 percentiles of wall stress with direct application of pressure

Table 5.5: Simulated 0.99 percentiles of the Von Mises stress in kPa from the segmentation reproducibility study for four AAAs. The variation in the 0.99 percentiles of the wall stress distribution is very limited for all four AAAs. Also with this measure the sensitivity with the backward incremental method is generally slightly worse than with direct, forward application of the maximum pressure.

tions of the maxima, especially when the values of the overall maximum wall stress are similar for the two segmentations. For all cases this behaviour corresponds to situations where there are several distinct maxima with similar values. Remarkably, aneurysm 2, which shows the largest variation in the approximated maximum stress value, shows the least variation in the location of the maximum.

5.3.3 User-induced variability and modality-induced variability

Table 5.7 shows the maximum distance between the manual delineations of the different user pairs for each of the AAAs. These distances have been computed with the average contouring method [13]. In table 5.8 we have listed the maximum distances between the surfaces based on these contours and the distance between the MR and the CT based AAA surface per user. The distance between the surfaces based on the different user delineations is smaller than the distances between the contours. This could be expected because the 3D segmentation tends to diminish some of the local variations in the contours that are not in correspondence with the contours on the adjacent slices. The distances between the user based surfaces

| | Smoothness level | | | | Smoothness level | | |
|------------|------------------|----|----|------------|------------------|---|----|
| | 5 | 8 | 11 | | 5 | 8 | 11 |
| Aneurysm 1 | 11 | 20 | 47 | Aneurysm 1 | 11 | 2 | 47 |
| Aneurysm 2 | 1 | 1 | 2 | Aneurysm 2 | 1 | 4 | 11 |
| Aneurysm 3 | 30 | 4 | 31 | Aneurysm 3 | 8 | 5 | 30 |
| Aneurysm 4 | 36 | 3 | - | Aneurysm 4 | 35 | 2 | - |

(a) *Distance between maxima with direct application of pressure*

(b) *Distance between maxima with the backward incremental method*

Table 5.6: Distances (mm) between the maximum stress locations in the wall stress simulations based on the different segmentations of the four aneurysms.

| | Expert combination | | | | Expert combination | | |
|------------|--------------------|-----|-----|------------|--------------------|-----|-----|
| | 1/2 | 1/3 | 2/3 | | 1/2 | 1/3 | 2/3 |
| Aneurysm 1 | 3.4 | 2.4 | 2.3 | Aneurysm 1 | 3.6 | 3.8 | 3.5 |
| Aneurysm 2 | 5.3 | 4.1 | 5.3 | Aneurysm 2 | 4.5 | 4.2 | 3.6 |
| Aneurysm 3 | 5.8 | 3.5 | 5.6 | Aneurysm 3 | 6.6 | 3.2 | 5.9 |
| Aneurysm 4 | 3.8 | 3.1 | 3.9 | Aneurysm 4 | 5.1 | 6.2 | 4.0 |

(a) *MR*

(b) *CT*

Table 5.7: Maximum distances (mm) between the manually delineated outer AAA wall contours for the different expert combinations.

are, however, generally larger than the distances that we found between the several segmentations for user 2 (see table 5.3). The variations between the CT and MR based segmentations per user are again larger than the variations induced by the segmentation method. Also these distances are markedly higher than the variations in the segmentations based on the different users.

Figure 5.11 shows the variation between the computed wall stress for the four aneurysms with MR and CT for the three different manual delineations of the outer vessel walls. The variation in the maximum wall stress, when not taking into account aneurysm 2 for which no reproducibility could be established, is 32% for the CT images and 23% for the MR images (aneurysm 2: 42% both on MR and CT). In both cases this is higher than the variation observed in the segmentation variability study with these parameter settings, which was only 11%. Moreover, the variation in the 0.99 percentiles of the stress is now also markedly higher, 20% on CT and 18% on MR while this variation was very limited for the segmentation variability experiments (6%). The average variability in the 0.99 percentiles for the vessel wall stress is 12%, both for MR and CT.

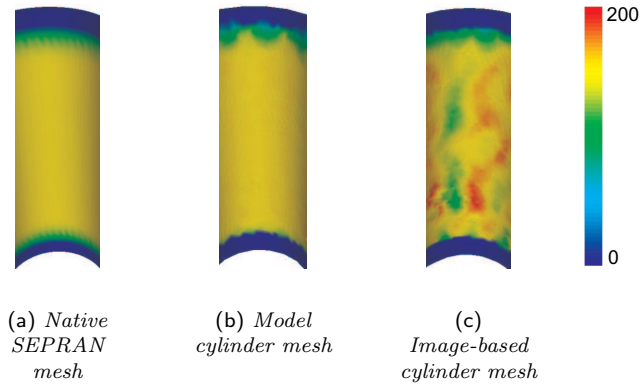


Figure 5.8: Simulation results for modelled and image-based cylinder geometries. Stress distribution (kPa) on the inner cylinder surface. For the golden standard model (a) and the 2-simplex model (b) the stress distribution in the cylinder wall is uniform. For the segmented geometry (c), local maxima occur.

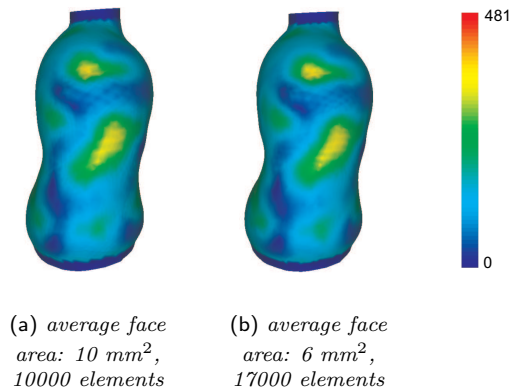


Figure 5.9: Von Mises wall stress (kPa) for the highest and the lowest mesh resolution for aneurysm 2. The wall stress distribution is similar in both cases.

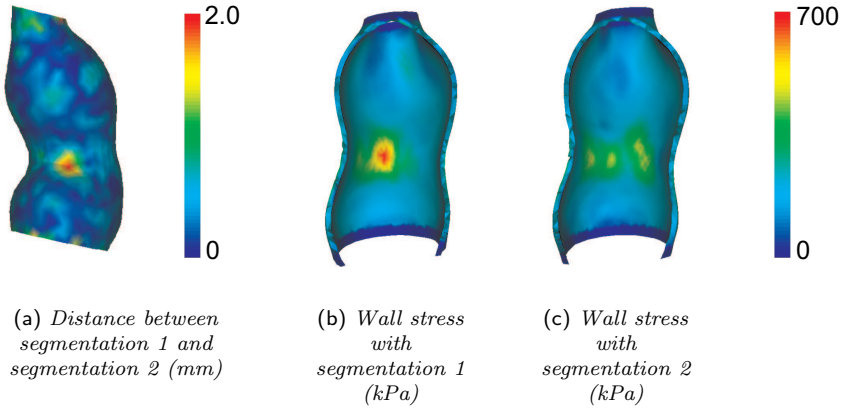


Figure 5.10: Von Mises wall stress (kPa) for the two segmentations of aneurysm 2 used in the variability study at smoothness level 11.

| | Maximum distance between segmentations for different users on MR | Maximum distance between segmentations for different users on CT | Maximum distance between MR and CT based segmentations | | |
|------------|--|--|--|--------|--------|
| | | | User 1 | User 2 | User 3 |
| Aneurysm 1 | 3.5 | 2.0 | 6.5 | 3.8 | 6.6 |
| Aneurysm 2 | 2.6 | 3.5 | 3.3 | 3.5 | 3.0 |
| Aneurysm 3 | 2.7 | 4.5 | 4.6 | 4.2 | 5.2 |
| Aneurysm 4 | 3.2 | 2.4 | 7.6 | 7.0 | 7.7 |

Table 5.8: Maximum distances (mm) between the various segmented 3D surfaces for the different users on CT and MR. The maximum distances between the different users are generally larger than the distances induced by the variations in the segmentations. The variations between the MR and CT based segmentations are generally larger than the distances induced by the user variability.

| | λ | | | |
|----------------------|------------------|----|-----|-----|
| | 0 (No smoothing) | 50 | 100 | 150 |
| Image-based cylinder | 36 | 38 | 47 | 54 |
| Aneurysm 1 | 1 | 8 | 4 | 2 |
| Aneurysm 2 | 21 | 12 | 6 | 9 |

Table 5.9: *Difference, as a percentage, in the peak wall stress for a cylinder, and two AAA shapes. For the cylinder shape the difference is computed with respect to the exact solution. For the AAA shapes the two segmentations at smoothness level 5 with maximum curvature variation were used.*

The ordering of the patients with respect to the estimated maximum wall stress is the same for MR and CT for users 2 and 3 and for the average over the three users (from large to small: aneurysm 2, aneurysm 1, aneurysm 3, aneurysm 4). Only for user 1 the order of aneurysms 1 and 3 is interchanged. Although the orders are mostly similar for the two modalities, the maximum wall stress for aneurysm 4 is highest when estimated from CT for all three users. Also, this is the aneurysm inhibiting the least variation over the users.

Figures 5.12 and 5.13 show the variations in the wall stress distributions on MR and CT for the different users. In figure 5.12 we have also plotted the differences caused by the segmentation variability for user 2. Both for MR and for CT, there are important differences between the wall stress distribution for the different manual delineations. The most notable difference is that the location and presence of local maxima tends to vary. This behaviour is also observed for the segmentation variability for user 2 on the MR images, but to a far lesser extent. This last observation is in agreement with the lower variations in the computed maximum stress for the variability experiments.

In figure 5.12, we have also plotted the maximum and the 0.99 percentiles of the wall stress computed with the automatic segmentation method previously described in chapter 2. Although the computed stresses with this model are not always within the user variability bounds, the trends are very similar, especially in the 0.99 percentiles of the wall stress. Also, the ordering of the aneurysms with respect to their maximum wall stress would be similar to the ordering derived from the other users, when aneurysm 2 is excluded. The difference in the automatically estimated wall stress for aneurysm 1 and 2 is, however, less than 1%.

5.3.4 The effect of sphere-shape based smoothing

Tables 5.9 and 5.10 show the effect of smoothing of the 2-simplex mesh on the approximated wall stress. Although the results for the AAA are not fully conclusive, it appears that smoothing does diminish the variations in the wall stress, especially for the 0.99 percentiles. On the other hand, the errors for the cylinder model increase for higher levels of smoothing.

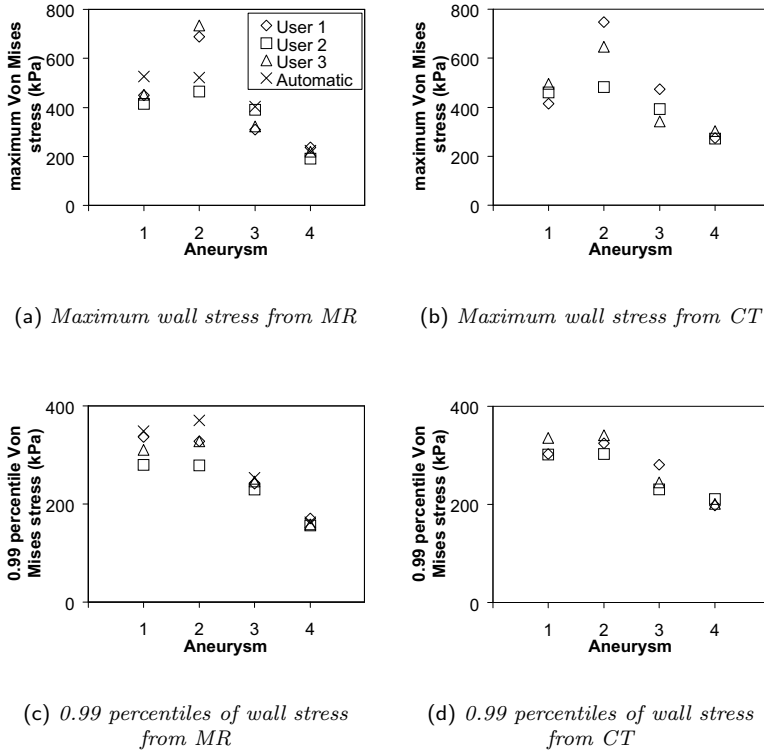


Figure 5.11: Variation in the simulated wall stress for three different manual delineations of the outer vessel wall on CT and MR images of four AAA patients.

5.4 Discussion and Conclusions

We have presented a study for the influence of segmentation errors, user variability and modality choice for wall stress simulations in abdominal aortic aneurysm. We have validated the model using a cylinder model, which is particularly challenging for the two simplex description which cannot locally accurately match a surface with zero Gaussian curvature. We have excluded the influence of the meshing methods and the mesh resolution using an aneurysm model.

The results of the segmentation variability experiment indicate that our segmentation method leads to reproducible results for the maximum wall stress for three of the four aneurysms when the influence of the internal forces in the deformable surface segmentation process is sufficiently high. The location of the maximum may shift especially when the absolute value of the maximum stress is reproducible. The influence of the segmentation error appears to be a local effect since the vari-

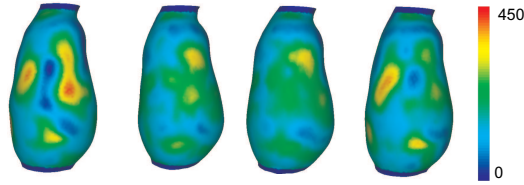
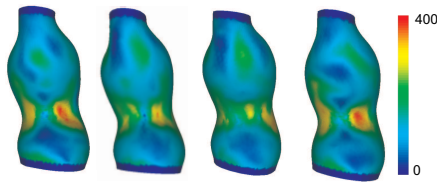
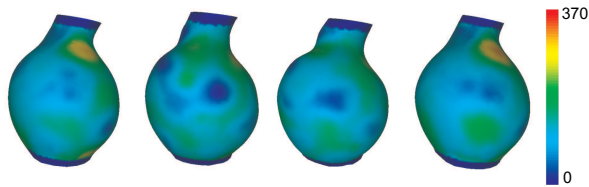
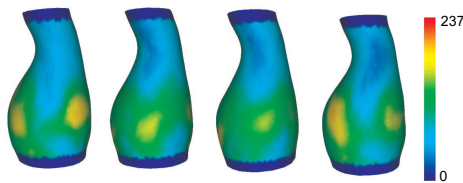
(a) *Aneurysm 1*(b) *Aneurysm 2*(c) *Aneurysm 3*(d) *Aneurysm 4*

Figure 5.12: *Approximated Von Mises wall stress (kPa) for the segmentations based on the different manual user delineations of the MR images. From left to right: user 1, user 2 segmentation 1, user 2 segmentation 2 and user 3. There are differences in the presence, the value and the location of the maxima, both for different segmentations and for different manual delineations. The variability caused by the user variation appears to be larger than the variability caused only by the segmentation errors.*

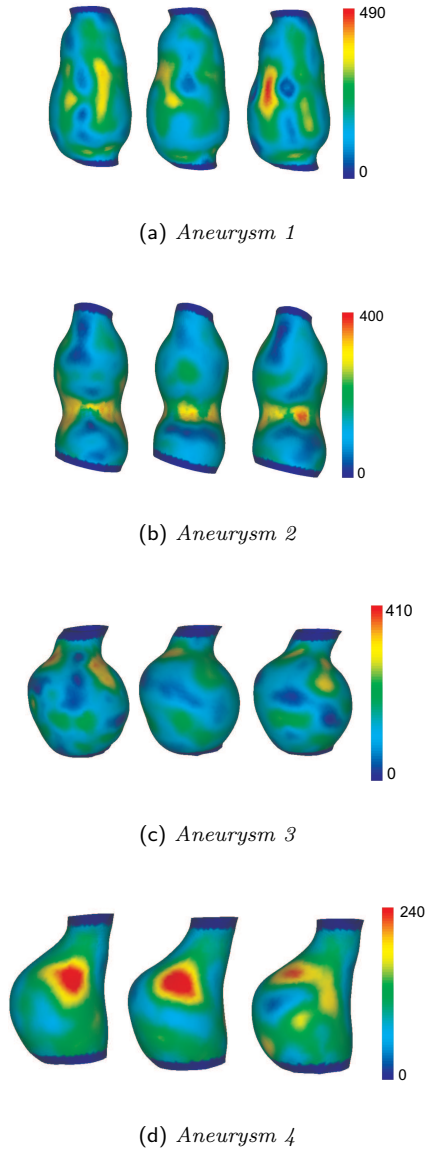


Figure 5.13: *Approximated Von Mises wall stress (kPa) for the segmentations based on the different manual user delineations of the CT images. From left to right: user 1, user 2, and user 3. There are differences in the presence, the value and the location of the maxima for the different manual delineations.*

| | λ | | | |
|----------------------|------------------|----|-----|-----|
| | 0 (no smoothing) | 50 | 100 | 150 |
| Image-based cylinder | 18 | 18 | 21 | 23 |
| Aneurysm 1 | 4 | 1 | 0 | 0 |
| Aneurysm 2 | 13 | 6 | 6 | 8 |

Table 5.10: *Difference, as a percentage, in the 0.99 percentile of the wall stress for a cylinder, and two AAA shapes. For the cylinder shape the difference is computed with respect to the exact solution. For the AAA shapes the two segmentations at smoothness level 5 with maximum curvature variation were used.*

ations caused by the segmentation errors in the 0.99 percentiles of the wall stress are very small for all four aneurysms. The reproducibility is slightly worse with the backward incremental method, in comparison to the classical forward approach. However, these variations are still of the same order as with the forward model.

The influence of the user variability is markedly higher than the influence of the variations in the segmentation. Also, the observed differences can no longer be accounted to very local effects, since the variation in the 0.99 percentiles of the wall stress distribution also increases. The influence of the user variability appears to be similar both on MR and CT. Smoothing with a sphere-shape based model might lead to better reproducibility, but, it can also introduce systematic errors as is indicated by the application of this model on a cylindrical model.

In this study, we made several assumptions. The selection of the geometries used to investigate the influence of the segmentation errors for the wall stress is based on the maximum variation in the curvature for these geometries. It has been pointed out repeatedly in literature that the main effect for the wall stress in the AAA wall, apart from the AAA size, is the local curvature caused by the specific shape of the aneurysm [32, 91]. Therefore, the assumption that the largest variation in the robustly estimated surface curvature will lead to the maximum variation in the wall stress seems reasonable. The simulation times necessary to perform wall stress simulations for all ten segmented geometries for several parameter settings are prohibitive, so this assumption was necessary in this study.

We assume that there is no residual wall stress in the unloaded AAA geometry. As yet, there is no method known that computes these residual stresses for a realistic AAA. We used non patient-specific values for the material properties, the pressure and the wall thickness and we neglected the influence of the intra-luminal thrombus, which still is rather controversial. We used a geometrically nonlinear but materially linear constitutive model for the AAA wall, while it has been reported that the true behaviour of the AAA wall is both geometrically and materially non-linear [85, 111, 119]. Although these assumptions may affect the accuracy of the wall stress approximation with respect to the real situation in the patient, they do not impose any limitations on the investigation of the sensitivity of the wall stress to geometrical errors, which was the main goal in this study.

In the segmentation for the AAA shape, we did not include the bifurcation of the

aorta into the iliac arteries. The slice distance and the slice thickness in the MR images (both 6 mm) are too large for an accurate reconstruction of the geometry in this region. We investigated only one single segmentation method. Although we cannot fully exclude that a different segmentation scheme would influence the results, the segmentation error of 2 mm found on MR is small with respect to the voxel size, making it unlikely that a different segmentation method would significantly outperform the method we used now.

It cannot be completely ruled out that a certain amount of the variation that we observed should be accounted to the limited resolution for the discretisation of the AAA surface and to inaccuracies in the geometrical modelling and mesh generation process. However, the results of the validation simulations indicate that the influence of the modelling approach on the final result is less than the variations we observed due to other influences. Also, the fact that the variations in the 0.99 percentiles of the wall stress with different manual delineations are much larger than the variations we observed in the reproducibility study indicates that these variations are most likely not caused by the modelling process.

A clear limitation of this work is that we used only four patients in this study and only had three manual delineations per patient. These numbers are too low to allow for an extensive statistical evaluation. The motivation for using only four patients is that we could not obtain more combined CT and MR data for AAA patients for whom the MR and CT scan dates were sufficiently close. The accurate manual delineation of the outer vessel wall on difficult data sets such as the ones used in this study is a time-consuming task. However, even with this small number of patients the results show that the uncertainty in the geometry may be a significant source of variation that must be taken into account even if this result does not generalise to all AAAs.

The 3DAO segmentation method that we employed has a large number of parameters. Also, different internal forces may be used to control the smoothness of the surface during the segmentation process [24]. In our study we focussed on the internal and external force weighting balance, since this directly influences the amount of variation in the curvature in the final segmentation result. We used the curvature based internal force implementation because it is directly related to the influence that is believed to dominate the local wall stress. Varying all parameters and implementation choices would have led to prohibitive simulation times. However, it may be that a different choice may lead to a less stable or more stable model.

To our knowledge there have been no previous studies on the sensitivity of the simulated wall stress in patient-specific abdominal aortic aneurysm. Therefore, we cannot compare our results to literature. Furthermore, from our results it appears that the sensitivity is highly influenced by the amount of geometrical detail allowed in the segmentation process and the geometrical modelling process. This makes it almost impossible to compare results between different simulations when the methods to approximate the AAA geometry are different. Although the wall stress caused by pressure load on the vessel wall and wall shear stress caused by the flow variations close the vessel wall do not originate from the same process and are of a completely

different order, these are both very local effects that are highly related to the local geometry. The high errors reported for patient-specific wall shear stress in vascular structures [71, 72, 73, 108] may indicate that the high sensitivity of the wall stress we observed are intrinsic for highly geometry dependent quantities derived from finite element simulations on complex domains inhibiting a certain level of uncertainty.

In conclusion, we have shown that the wall stress in patient-specific models of AAA is sensitive to geometrical variations caused by both automatic and manual segmentation errors. In most cases the variations in the estimated maximum stress caused by variations in the *automatic* segmentation result may be diminished by limiting the amount of variation allowed in the geometrical model, but this will not work for every AAA. The influence of the user variability in the *manually delineated* contours on the stress is considerable, and of a higher order and less localised than the variations caused only by the automatic segmentation errors.

For robust rupture risk prediction it appears to be best not to focus on very local geometrical effects. This may be achieved by either using a less detailed representation of the geometry or by using more stable statistical predictors derived from the overall wall stress distribution.

For future research it is important to test the influence of the segmentation method, the geometrical representation of the AAA and the user variability on larger number of data sets, preferably with known rupture history, to find the optimal balance between robustness and sensitivity for patient-specific rupture risk prediction based on AAA wall stress.

Models for local wall stress analysis in the calcified abdominal aortic aneurysm wall

Abstract

Finite element wall stress simulations on patient-specific models of abdominal aortic aneurysm (AAA) may provide a better rupture risk predictor than the currently used maximum transverse diameter. Calcifications in the wall of AAA lead to an elevated maximum wall stress. Both the reported material properties for calcifications and the material properties used for simulations show great variation. Previous studies have focussed on simplified modelling of the calcification shapes within a realistic aneurysm shape. The objective of this study is to investigate the influence of the calcification geometry, the material properties and the modelling approach for the computed peak wall stress. We scanned micro-CT images of calcified AAA wall specimens and investigated the influence of the clinical CT resolution limitations on the appearance of the calcifications. For four realistic calcification shapes from standard clinical CT images of patients with intact AAA, we performed simulations with three distinct modelling approaches, at five distinct elasticity settings. The results show how the peak wall stress is sensitive to the material properties of the calcifications. For relatively elastic calcifications, the results from the different modelling approaches agree. For stiffer calcifications, however, large deviations are observed. Also, for relatively elastic calcifications the computed wall stress in the non-calcified tissue surrounding the calcifications shows to be insensitive to the exact calcification geometry. Based on the combination of the information from the micro-CT images and the simulation results we conclude that wall stress simulations for AAA incorporating calcifications should focus on the stress in the healthy tissue, resulting from the presence of the calcifications, and not on the stress in the calcification or on the material interface. Furthermore, we conclude that also for the proper choice of the modelling approach an important challenge for future research is the accurate estimation of the material properties of the calcifications. Only then stress analysis will enable assessment of the rupture potential of the AAA wall including calcifications.

6.1 Introduction

Wall stress simulations on abdominal aortic aneurysms (AAA) have been widely recognised to provide an indication of rupture risk on a patient-specific basis [37, 38, 86, 110, 120, 125]. Fillinger et al. [38] have shown that wall stress can have a higher discriminatory value than the maximum transverse AAA diameter, which is currently used as a clinical decision parameter. The aneurysm shape has an important influence on the wall stress distribution [32, 123]. Other potentially important influences are the patient's blood pressure, the local wall thickness, variations in the wall material properties and intra-luminal thrombus formation. The value used for the maximum pressure is either the monitored systolic pressure [37, 38, 86, 120, 125] or a non patient-specific systolic value [110]. The correct approach for modelling the influence of intra-luminal thrombus is still controversial. Modelling the thrombus as an elastic medium leads to a diminished load on the vessel wall [27]. Clinical studies, however, indicate that the pressure at the aneurysmal wall is not affected by the presence of thrombus [95, 112].

The AAA vessel wall differs from the healthy vessel wall because the extracellular matrix has been degraded [9]. The inflammation and plaque formation processes related to the aorta expansion may lead to a heterogeneous wall composition. Although the constitutive models employed in the previously mentioned studies vary, these models do not take into account this heterogeneity. With an idealised model for the AAA wall the computed wall stress may provide a more advanced predictor based on the AAA geometry and the monitored pressure, but this will not necessarily be an accurate reflection of the actual stresses in the vessel wall. The local constituency of the vessel wall material may not only affect the stress values, but it is also likely to affect the amount of stress that the wall can bear locally.

Only recently, it has been shown that the presence of calcifications in the AAA wall may have a significant influence on the wall stress [69, 100]. These studies use very different assumptions for the elasticity of the calcifications. The approach in both studies is to model the influence of the calcifications by altering the material properties in a pre-defined finite element mesh of interpolation points representing the AAA wall. This will not allow an accurate representation of the local influence of the shape of the calcification geometry. Speelman et al. [100] have suggested that the material properties and the local shape of the calcifications may be of great importance.

Although there is some ongoing research that investigates the potential of imaging techniques to provide the local material properties in tissue [8, 14, 133], AAA material properties cannot yet be assessed accurately with clinical scanners. The majority of reports on material properties for calcified tissue are for the coronary arteries and the iliac arteries [50, 52, 62, 90, 129]. Reports for the material properties of calcifications in AAA are more scarce. The measured elasticity coefficient for calcified tissue in the coronary arteries varies from 1.5 MPa to 19 MPa [52, 129]. For the iliac arteries Holzapfel et al. [50] report values in the range from 7.9 MPa to 17.3 MPa. The elasticity values reported for calcifications in AAA vary from 4 MPa

[4] to 20 MPa [53]. The elasticity that is actually being used for patient-specific simulations even varies from 1.5 MPa [100] to 15 GPa [69].

There is strong variation in the material parameters used in the previous studies to model the influence of calcifications. Furthermore, the low-resolution approach of the previous studies has not been validated, implying that the results from that work depend heavily on the validity of the model assumptions. There is an evident need to investigate the best modelling approach for calcifications in 3D stress simulations for AAA and to investigate the variations that arise from the uncertainty in the model settings. In this work we aimed to deduce the best way to model the influence of calcifications in the AAA wall for wall stress simulations at the different material parameter regimes reported in literature. We have investigated the meaning of the appearance of calcification on clinical CT images and we have compared three different high-resolution modelling approaches. The results have allowed us to draw conclusions with respect to the best method to model calcifications in AAA.

6.2 Materials and methods

6.2.1 Constitutive wall model

Both for the calcifications and the vessel wall we use the neo-Hookean model that describes an isotropic elastic medium with large deformations. This is the simplest constitutive model that allows us to capture the influence of differences in material properties in the range of deformations we are interested in. We consider an incompressible elastic medium in the time dependent domain $\Omega(t) \subset \mathbb{R}^3$, bounded by $\Gamma(t) = \partial\Omega(t)$, with outward normal \mathbf{n} . Let \mathbf{F} be the deformation gradient tensor

$$\mathbf{F} = \frac{\partial \mathbf{x}}{\partial \mathbf{X}}, \quad (6.1)$$

with \mathbf{X} the reference configuration and $\mathbf{x} = \mathbf{x}(\mathbf{X}, t)$ the current configuration. In the absence of body forces, the equations of motion and continuity from continuum mechanics are

$$\operatorname{div}(\boldsymbol{\sigma}) = \mathbf{0} \quad \text{in } \Omega, \quad (6.2)$$

$$\det(\mathbf{F}) = 1 \quad \text{in } \Omega. \quad (6.3)$$

The Cauchy stress for an incompressible elastic medium reads

$$\boldsymbol{\sigma} = -p\mathbf{I} + \boldsymbol{\tau}, \quad (6.4)$$

with p the hydrostatic pressure, \mathbf{I} the identity and $\boldsymbol{\tau}$ the extra stress resulting from deformations. For a neo-Hookean material, we have $\boldsymbol{\tau} = G(\mathbf{B} - \mathbf{I})$, with G the shear modulus and $\mathbf{B} = \mathbf{F} \cdot \mathbf{F}^T$ the left Cauchy-Green strain tensor (also known as Finger tensor).

The set of equations is completed with boundary conditions on each part of the domain boundary $\Gamma_k(t)$, with $\bigcup_k \Gamma_k(t) = \Gamma(t)$, and $\Gamma_k(t) \cap \Gamma_l(t) = \emptyset$, $\forall k \neq l$.

The Dirichlet boundary conditions, which explicitly fix the displacement on the boundary read

$$\mathbf{x} \cdot \mathbf{n} = x_n, \quad (6.5)$$

$$\mathbf{x} \cdot \mathbf{t}_i = x_{t_i}, \quad \mathbf{n} \cdot \mathbf{t}_i = 0, i \in \{1, 2\}, \quad (6.6)$$

where \mathbf{t}_1 and \mathbf{t}_2 are linearly independent vectors. The Neumann boundary conditions, in which the surface traction $(\boldsymbol{\sigma} \cdot \mathbf{n})$ in the normal and tangential direction is prescribed read

$$(\boldsymbol{\sigma} \cdot \mathbf{n}) \cdot \mathbf{n} = s_n, \quad (6.7)$$

$$(\boldsymbol{\sigma} \cdot \mathbf{t}_i) \cdot \mathbf{t} = s_{t_i}, \quad \mathbf{n} \cdot \mathbf{t}_i = 0, i \in \{1, 2\}, \quad (6.8)$$

A special case occurs when $s_n = 0$. This situation is referred to as a stress-free boundary condition.

6.2.2 Weak formulation

Let $W = \left\{ \mathbf{w} \in [H_o^1(\Omega)]^3 \right\}$, with $H_o^1(\Omega)$ the functional Hilbert space of functions f that satisfy the Dirichlet condition $f|_\Gamma = 0$ and let $Q = \{q \in L^2(\Omega)\}$. With substitution of the Neumann boundary conditions and partial integration, the weak formulation of equations (6.2) and (6.3) becomes

$$\int_{\Omega(t)} (\nabla \mathbf{w})^T : \boldsymbol{\sigma} d\Omega = \int_{\Gamma(t)} \mathbf{w} \cdot (\boldsymbol{\sigma} \cdot \mathbf{n}) d\Gamma, \quad \forall \mathbf{w} \in W, \quad (6.9)$$

$$\int_{\Omega(t)} q(\det(\mathbf{F}) - 1) d\Omega = 0, \quad \forall q \in Q. \quad (6.10)$$

The notation " : " is used to denote the 3D double dot product $\mathbf{A} : \mathbf{B} = tr(\mathbf{A} \cdot \mathbf{B})$. Let $\Omega_n := \Omega(t_n)$ and $\Gamma_n := \Gamma(t_n)$. To evaluate the integrals in (6.9) and (6.10) over the domain (Ω_n, Γ_n) , we use the updated Lagrange approach, which implies that the previous configuration $(\Omega_{n-1}, \Gamma_{n-1})$ is taken as the reference configuration for (Ω_n, Γ_n) . The gradient operator is also interpreted with respect to the previous configuration. With \mathbf{F}_i^n we will denote the deformation tensor from the domain Ω_i to the domain Ω_n . Similarly, we will denote the gradient operator with respect to the domain Ω_i with ∇_i . This way the total transformation from Ω_o to Ω_n becomes

$$\mathbf{F}_o^n = \mathbf{F}_{n-1}^n \cdot \mathbf{F}_o^{n-1} = (\nabla_{n-1} \mathbf{x}_n)^T \cdot (\nabla_o \mathbf{x}_{n-1})^T. \quad (6.11)$$

It is customary in the updated Lagrange method to take the displacement field of the material points as the unknown. At time t_n , this field is defined through $\mathbf{u}_i(t_n) = \mathbf{x}_i(t_n) - \mathbf{x}_i(t_{n-1})$, where $\mathbf{x}_i(t_n)$ and $\mathbf{x}_i(t_{n-1})$ denote the position of a material point at two subsequent points in time.



Figure 6.1: A human tissue sample of an abdominal aortic aneurysm wall.

When writing $\nabla_n = (\mathbf{F}_{n-1}^n)^{-T} \cdot \nabla_{n-1}$ the weak form of the system (6.9,6.10) becomes

$$\int_{\Omega_{n-1}} (\nabla_{n-1} \mathbf{w})^T : (\mathbf{F}_{n-1}^n)^{-1} \cdot \boldsymbol{\sigma} J_{n-1}^n d\Omega_{n-1} = \int_{\Gamma_{n-1}} \mathbf{w} \cdot \mathbf{s} \tilde{J}_{n-1}^n d\Gamma_{n-1}, \quad (6.12)$$

$$\int_{\Omega_{n-1}} q(J-1) J_{n-1}^n d\Omega_{n-1} = 0, \quad (6.13)$$

where J_{n-1}^n and \tilde{J}_{n-1}^n are defined through $d\Omega_n = J_{n-1}^n d\Omega_{n-1}$ and $d\Gamma_n = \tilde{J}_{n-1}^n d\Gamma_{n-1}$. In equation (6.12), \mathbf{s} is defined by equations (6.7) and (6.8).

6.2.3 Finite-element formulation and solution strategy

To obtain a finite-element formulation of the system (6.12,6.13) the domain (Ω, Γ) is divided into non-overlapping discrete elements. Within each element, the physical unknowns are approximated with Lagrange interpolation polynomials.

At each time step, the non-linear algebraic system rendered from (6.12,6.13) is linearised with Newton's method and we iterate to obtain a converged solution. The linearised system at each iteration step is preconditioned with an incomplete LU decomposition and solved with the Bi-CGSTAB method [117]. For the simulations we used $Q_2^+ P_1$ tetrahedral elements (15 nodes) and hexahedral elements (27 nodes), yielding a quadratic approximation. All of the simulations have been performed with the finite element code SEPRAN (Septra analysis, Delft, The Netherlands).

6.2.4 Simulation of low resolution CT imaging on high resolution CT images of calcified plaque

Although the spatial resolution of CT scanners is superior to all other 3D imaging modalities used in the clinical environment, small structures such as calcifications are still sampled with only a limited number of voxels, possibly eluding important details. In order to obtain a better understanding of the true geometrical configuration of calcifications in AAA tissue and the effect of CT imaging for these lesions, we simulated the CT scanning process on ultra-high resolution images of calcifications. AAA tissue samples were obtained from two patients treated with conventional repair surgery. An example of such a human AAA tissue sample is shown in figure 6.1. Within 24 hours after harvest the tissue was stored in a 4% formalin fixation.

To exclude motion artefact during CT scanning, the samples were fixed in a 3% agarose gel. High resolution images were obtained with the Scanco μ CT 80 scanner. The isotropic image voxels were $32\mu\text{m}$. The 10% MTF resolution reported for this scanner is $16\mu\text{m}$ [93]. With the assumption that the point spread function (PSF) of the scanner is also a Gaussian [77], we can deduce that the standard deviation of the PSF is $11\mu\text{m}$.

We down-sampled the scanned images to a voxel size of $0.5 \times 0.5 \times 1.0 \text{ mm}^3$, which is representative of a clinical CT scanner, by taking the average value of the grey values of the voxels in the high resolution image within the larger voxels of the down-sampled image.

6.2.5 Comparison and evaluation of the models

To investigate the influence of the modelling approach we have used three different models. In all models we assume that the surroundings of the calcification are uniform tissue. In the first model we assume that the calcification geometry is represented by an iso-intensity surface in the clinical CT images and accurately model the material interface between the calcification and its surroundings by using distinct meshes for both areas. In the second model we use the same threshold to distinguish the calcification from its surroundings, but we model the calcifications by changing the properties in a pre-defined grid of interpolation points, based on the intensity in the image voxels, as was done in the earlier publications [69, 100]. In the third and final model we take a similar approach with a predefined grid, but here we use a linear relation between the material stiffness and the image intensity, based on the assumption that the image intensity is representative of the calcification concentration.

Model 1: iso-intensity surface based geometry

For the first modelling approach we applied the marching cubes algorithm [66] with a threshold of 200 Hounsfield units to obtain a triangulation of the iso-intensity surface of the calcified plaque. The resulting surface tessellations have been re-meshed with NETGEN (<http://www.hpfem.jku.at/netgen/>) to obtain better quality surface meshes. We have generated tetrahedral meshes for the resulting two-material structures with an in-house mesh generation application. On the material interface we used a continuous displacement field, i.e. no friction between the calcification and the tissue was allowed.

Model 2: uniform mesh with material properties based on a threshold on image intensity

In this approach we generated hexahedral meshes for the bounding box representing the tissue without taking into account the shape of the calcification for the meshing. Afterwards, we determined for every interpolation point in the mesh whether the image intensity of the original CTA images at this location was above or below

the threshold of 200 Hounsfield units. If the intensity was above this threshold, the shear modulus in this interpolation point was set to a value corresponding to calcified tissue, otherwise it was set to a value corresponding to normal AAA tissue.

Model 3: uniform mesh with material properties based on a linear relationship with the image intensity

In the final modelling approach, we assume that the stiffness of the tissue is directly related to the image intensity in the CT image. This approach is inspired by the outcome of the down-sampling of the high resolution images described in section 6.2.4, which showed that what appears as an isotropic high intensity area may actually be a complex configuration of calcified parts in otherwise normal tissue. The shear modulus is modelled as a linear function of the image intensity through

$$G(\mathbf{x}) = G_{\text{tissue}} + \frac{I(\mathbf{x}) - I_t}{I_{\text{max}} - I_t} (G_c - G_{\text{tissue}}), \quad (6.14)$$

with $G(\mathbf{x})$ the shear modulus assigned to position \mathbf{x} , G_{tissue} the shear modulus of the non-calcified tissue, and G_c the calcification shear modulus. With $I(\mathbf{x})$ we denote the intensity at location \mathbf{x} , with I_t the threshold intensity and with I_{max} the maximum image intensity.

6.2.6 Simulations

Since the influence of the calcified regions on the wall stress is assumed to be a local effect, we chose to model only a small section of the AAA wall around every calcification. The local wall curvature has been neglected and we simulated the load by applying a stretch in the circumferential direction of the vessel wall. These assumptions seem reasonable, since the size of the calcifications that we selected is small with respect to the curvature of the vessel wall. Furthermore, for vascular structures, the circumferential strain will generally be higher than the axial strain.

We selected four calcifications from two routinely acquired CT data sets of AAA. For these calcifications, we manually delineated the central axes of the calcifications along the tangential direction of the vessel wall within the central imaging plane. The CTA images were then locally resampled, such that the y-axis of the resampled image corresponds to the manually delineated axis, as depicted in figure 6.2. The surrounding, non-calcified tissue was modelled as a box with dimensions $6 \times 2l \times 2h$ mm, with l the length of the central axis and h the height of the calcified region, as shown in figure 6.3. One of the two bounding box planes perpendicular to the y axis of the calcification was clamped in all directions. On the other of the perpendicular planes we prescribed a fixed displacement of 6% of the length of the modelled tissue sample. The sharp corners of the box representing the tissue sample and the boundary conditions used to keep the tissue in place lead to an unrealistic solution at the boundary of the mesh. To clear these effects from the solutions, the stress and strain values have been set to zero in the presentation of all results in a 0.5 mm thick region inward from the bounding box of the mesh.

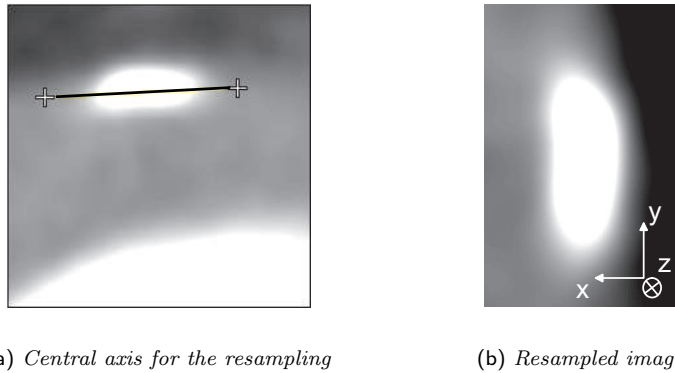


Figure 6.2: Resampling of a calcification in an AAA wall on a CTA image along the tangential direction of the intersection contour of the imaging plane and the aneurysm wall.

Mesh resolution tests have been performed to establish the resolution necessary to obtain converged solutions. The number of elements in the meshes used in the final simulations varied from 18000 to 24000. The surface meshes for the calcifications are shown in figure 6.4. For the shear modulus of the tissue we used a value of 1.0 MPa, which corresponds to the measured realistic value [28]. We performed experiments for all four calcifications with all three modelling approaches with a shear modulus for the calcification G_c of 1.5 MPa, 2 MPa, 5 MPa, 20 MPa, and 100 MPa. Stress values were computed both for the calcified region and for the surrounding, non-calcified tissue. For comparison, we also ran simulations for all geometries without any calcification present.

6.3 Results

Figure 6.5 shows the effect of the simulation of the resolution of a patient CT scanner on a high resolution image of a calcified area. It is clearly visible that the complex configuration of multiple calcified regions in the ultra high resolution image is transformed into a smaller number of high intensity regions in the normal resolution image.

The simulations without calcifications resulted in stress distributions with maximum stress values limited by 259 kPa and 269 kPa for all four geometries. The maximum stress values occurred in the center of the geometry.

Figure 6.7 shows the simulation results for the threshold based models with an iso-intensity surface based mesh and with a uniform mesh (models 1 and 2) for the lowest and highest value of G_c in an xy-plane through the tissue. In Figures 6.7(a), 6.7(c), 6.7(e) and 6.7(g) we have depicted the overall stress in both the calcification

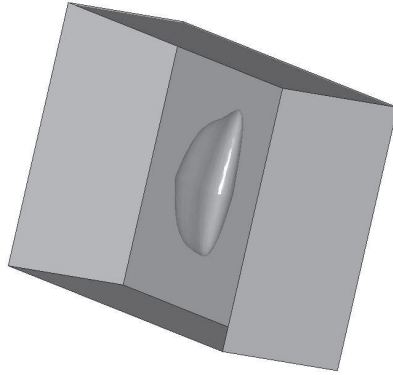


Figure 6.3: *A segmented calcification placed within a modelled strip of healthy tissue.*

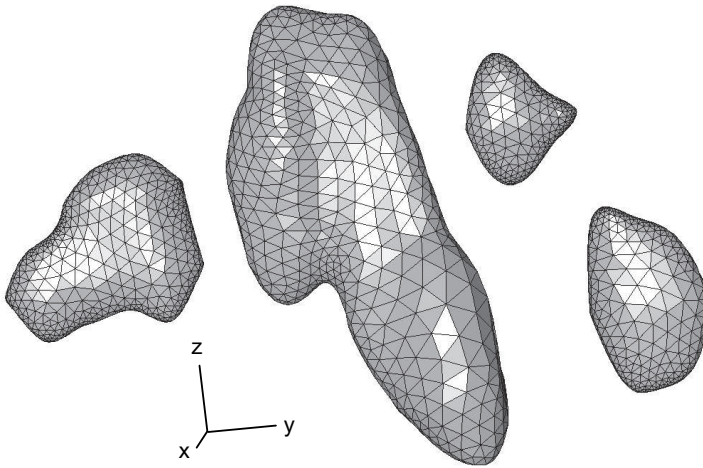


Figure 6.4: *Surface meshes for the four calcifications, segmented from clinical CT images of abdominal aortic aneurysm. The y-direction corresponds to the original tangential direction of the intersection contour of the imaging plane and the outer aneurysm wall.*

and the surrounding, non-calcified tissue. Figures 6.7(b), 6.7(d), 6.7(f) and 6.7(h) show only the stress in the non-calcified tissue. In the figures, the ranges of the stress values have been adjusted for visualisation purposes. The true maxima can be read from the graphs in figure 6.6. The results from the model with a linear relationship between the image intensity and the material stiffness (model 3) look very similar to the results from model 2, apart for a linear scaling between the ranges of the stress. Therefore we do not present any images of these stress fields. In table

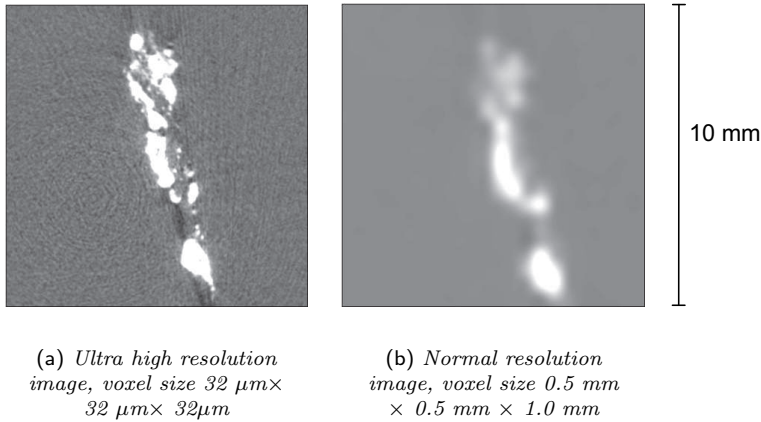
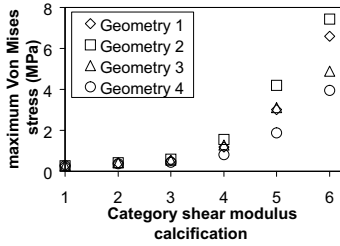


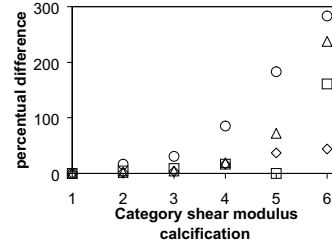
Figure 6.5: The effect of imposing the resolution of a patient CT scanner on an ultra-high resolution CT image of calcified tissue. Many of the detailed structures visible on the ultra-high resolution image are lost on the normal resolution image. Also, the outer contours of the calcified areas in the low resolution image do not correspond to the shape of the calcifications as they appear on the high resolution images.

6.1, we have listed the average of the maximum stress over the four geometries for all different modelling approaches. Figure 6.6 shows the sensitivity of the computed maximum stress for the material properties of the calcification. Figure 6.6(b) shows the differences (in percentage) between models 1 and 2.

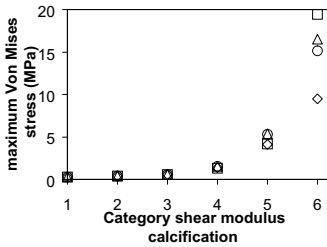
Clearly, with all models there is a strong relation between the computed stress and the shear modulus of the calcification. For lower shear moduli, there is a slight elevation in the wall stress inside the calcified regions. The wall stress in the non-calcified tissue remains relatively uniform and the maximum stress is not affected much. With the threshold based models (models 1 and 2) there is a slight elevation in the stress in the non-calcified tissue, with a linear relationship between image intensity and material stiffness (model 3) we even witness a slight decrease in the stress level in the non-calcified tissue. For these less stiff calcifications, the maximum stress value appears to be insensitive to the exact shape of the calcification, as can be clearly observed in figure 6.6. For stiffer calcifications, all models show pronounced stress peaks at the distal ends of the calcification inside the surrounding tissue. These stress peaks also occur inside the calcification itself and on the material interface, as can be clearly observed in figures 6.8 and 6.9. The values of these stress peaks are higher than the stresses for the less stiff calcifications.



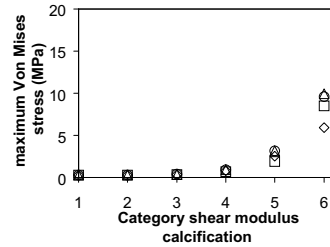
(a) Overall maximum stress with model 1



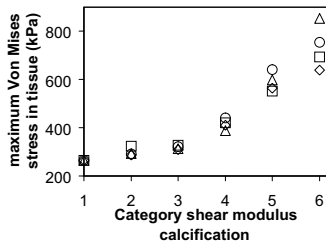
(b) Differences (%) in the overall max. stress with model 1 and model 2



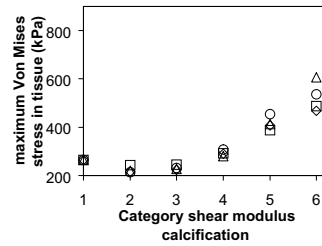
(c) Overall maximum stress with model 2



(d) Overall maximum stress with model 3



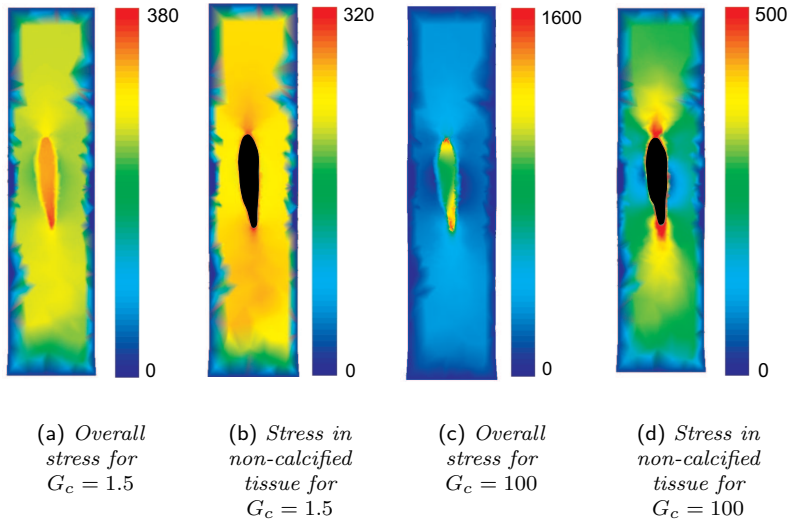
(e) Maximum stress in the non-calcified tissue with model 2



(f) Maximum stress in the non-calcified tissue with model 3

Figure 6.6: Maximum stress results with the three different models for the four calcifications. The categories of the shear modulus correspond to a respective calcification shear modulus of 1.0 MPa, 1.5 MPa, 2 MPa, 5 MPa, 20 MPa and 100 MPa. With models 1 and 2, for lower values of G_c , the exact calcification shape is of minor importance for the maximum stress in the non-calcified tissue surrounding the calcification, as can be observed in sub-figures (e) and (f).

Iso-intensity surface based mesh (model 1)



Uniform mesh with threshold based material properties (model 2)

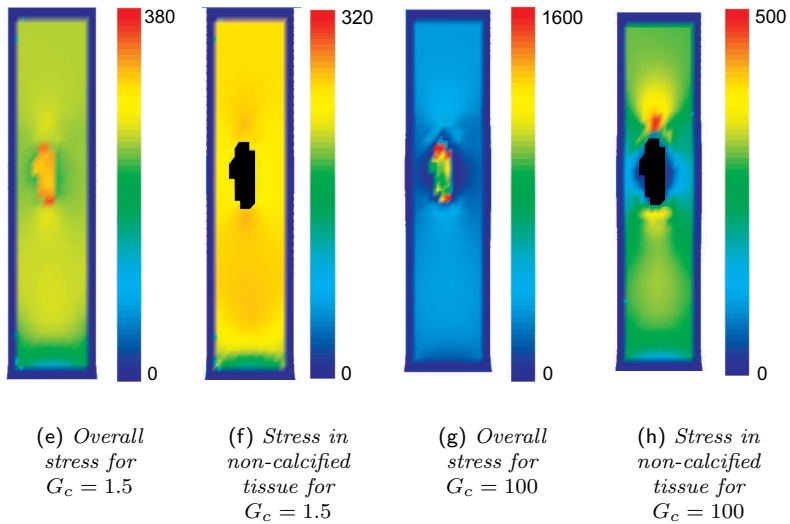


Figure 6.7: Von Mises stress (kPa) for calcification geometry 1 on an xy cross section with the iso-intensity surface based mesh (model 1) and the uniform mesh with threshold based material properties (model 2) for the minimum and maximum values of G_c . The stress distributions with the model with a linear relationship between image intensity and G_c (model 3) are similar to the results from model 2, although the stress values are lower (see also figure 6.6).

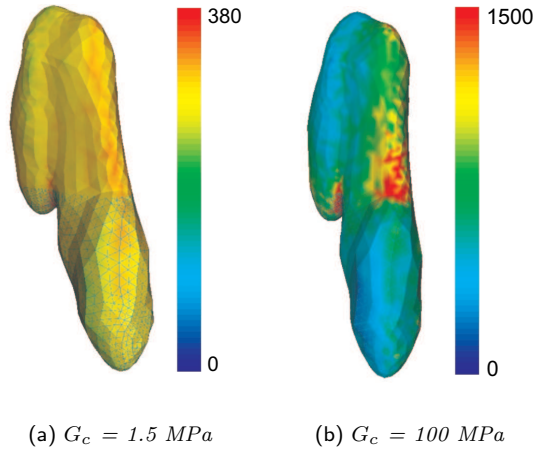


Figure 6.8: Von Mises stress with an iso-intensity surface based mesh (model 1) for geometry 2 on the calcification surface. For lower ratios of the calcification shear modulus and the tissue shear modulus the stress distribution on the material interface is uniform. For higher ratios, pronounced areas with high stress concentrations occur.

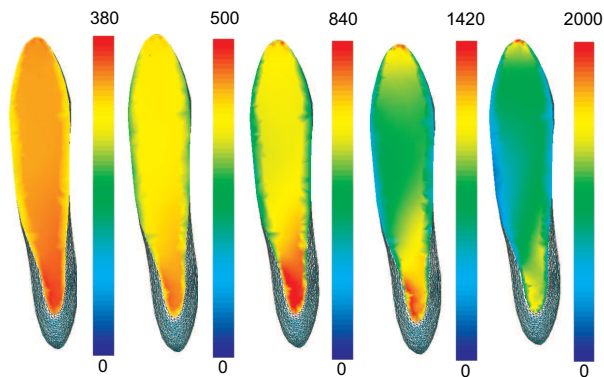


Figure 6.9: Stress distribution on an xy cross section through calcification number 2, with the iso-intensity surface based mesh (model 1) for increasing stiffness of the calcification. From left to right: $G_c = 1.5 \text{ MPa}$, $G_c = 2.0 \text{ MPa}$, $G_c = 5.0 \text{ MPa}$, $G_c = 20 \text{ MPa}$, and $G_c = 100 \text{ MPa}$. It can be observed that also inside the calcification the stress distribution becomes less uniform for high ratios of G_c/G .

| Model | Shear modulus calcification (MPa) | | | | |
|-----------------------------------|-----------------------------------|-----|------|------|-------|
| | 1.5 | 2.0 | 5.0 | 20.0 | 100.0 |
| 1, overall stress | 396 | 528 | 1210 | 3050 | 5710 |
| 2, overall stress | 410 | 561 | 1440 | 4750 | 15100 |
| 2, stress in non-calcified tissue | 299 | 317 | 415 | 589 | 735 |
| 3, overall stress | 274 | 354 | 828 | 2690 | 8510 |
| 3, stress in non-calcified tissue | 223 | 232 | 292 | 415 | 525 |

Table 6.1: Average maximum Von Mises wall stress (kPa) for the four calcifications.

6.4 Discussion

Inclusion of calcified regions in AAA wall stress simulations leads to elevated overall maximum stress values with all modelling approaches and all geometries that we considered. For small values of the ratio between the calcification shear modulus and the shear modulus of the non-calcified tissue, all models predict a uniform, slightly elevated stress within the calcified regions. Already for simulations with $G_c/G = 5$, however, the stress distribution inside the calcification becomes less uniform and stress peaks occur at the distal tips both inside the calcification and inside the non-calcified tissue. When the stress inside the calcifications and on the material interfaces is discarded, there is no strong effect on the stress for relatively compliant calcifications. For stiffer calcifications, stress peaks occur in the non-calcified tissue as well.

There are a number of differences between the results from the different models. For relatively elastic calcifications, the results from the threshold based models (model 1 and model 2) for the overall wall stress are similar. For stiffer calcifications, there are large deviations in the predicted maximum stress for these two modelling approaches which are most likely caused by the different calcification geometry representations. The model based on a uniform mesh with a linear relationship between the material stiffness and the image intensity (model 3) provides similar results as the threshold based model (model 2), but the predicted stress values are lower. This effect may be at least partly related to the fact that the integral stiffness in this model is lower, because of the high blurring caused by the CT point spread function. The apparent decrease in the wall stress in the non-calcified tissue for $G_c = 1.5$ and $G_c = 2.0$ with model 3 is most likely due to the fact that the position where the maximum wall stress occurred in the reference simulations is now occupied by the calcification, which means that this area is not taken into account when evaluating the wall stress in the tissue surrounding the calcification. Since the experiments with the micro-CT images indicate that the image intensity might be an indication of the calcification density, this model may provide an easy means to account for stiffness variations between multiple calcifications in an AAA.

Because our models focus on the detailed geometry of the calcification, we had to make several assumptions. All of the calcifications we examined were relatively small. There is, however, no obvious reason to assume that larger patches of calcified

tissue would behave differently. All tissue samples were exposed to a similar stretch. Within the AAA geometry the strain excised on the calcification is dependent on the location. However, to test the influence of the geometry, the modelling approach and the mechanical properties, it is essential to keep all other influences fixed. Still, for a true patient-specific stress prediction the AAA geometry must be taken into account. The mechanical model that we employed also has several limitations. First of all, no friction was allowed on the material interface between the calcifications and the non-calcified tissue. The true behaviour of this transition, while not known, may be of utmost importance for the rupture behaviour of the vessel wall. Furthermore, both the calcification and the surrounding tissue have been modelled as isotropic elastic media with a linear stress-strain relation, while the true behaviour of the vessel wall material may be more complicated [121]. However, the purpose in this study was to study the influence of the modelling approach and variations in the mechanical properties of the tissues for these models. Furthermore, if softer tissues are present in the non-calcified regions, this will elevate the rupture risk rather than decrease it.

Comparison of our results with earlier studies that do not take into account the precise geometry of the calcification is not straightforward since the model assumptions were different. The uniform, slightly elevated stress inside the calcifications for $G_c = 1.5$ MPa and $G_c = 2.0$ MPa appears to be in accordance with the results of Speelman et al. [100]. Marra et al. [69] use extremely stiff calcifications and the maximum stress is concentrated in two single elements, indicating that the mesh resolution in those simulations may have been too low.

There is high uncertainty in the material properties of the calcification and the different models predict different maximum stress values for different ranges of the material properties. This makes it difficult to choose an optimal model that is valid for all ranges and that can capture all effects that we witnessed. However, if we only focus on the stress in the non-calcified tissue in the vicinity of the calcification and discard the stress on the material interface and inside the calcification itself, it may be possible to choose a best model.

There are several reasons to focus on the stress inside the surrounding tissue only. The micro-CT images of calcifications indicate that what appears as a solid, uniform calcification on normal resolution CT images may in fact be a complex arrangement of smaller calcified areas. This means that it is of little use to try to accurately model the shape and the material interface of the calcification, because the imaging resolution is too low to capture these details. Therefore we feel that model 1, in which we separately meshed the segmented calcification and the surrounding tissue to capture the material interface, should be discarded.

The computed stresses are always highest inside the calcifications. However, a calcification that appears as a solid uniform region may be either exactly that, or a complex combination of calcified parts and other tissue. In the first case, it seems reasonable to assume that the calcification is not likely to rupture, so that the high stress values are of little importance for rupture prediction. In the second case, the computed stress values are not necessarily representative of the true stress inside

the calcified region, so they can also not be used for rupture predictions. Our results indicate that if we only focus on the stress in the non-calcified tissue close to the calcification, the exact geometry is less important than the material properties of the calcification and the non-calcified tissue.

If the calcifications are modelled as relatively compliant in relation to the tissue stiffness, the stress elevation is modest and uniform. In this situation it suffices to change material properties on a predefined grid as long as the grid size is related to the size of the smallest calcification. For stiffer calcifications, it will be necessary to locally refine the grid in the neighbourhood of the calcification to capture the small stress peaks at the tips of the calcification.

From the results of the down-sampling of the micro-CT images, it appears that there is a relation between the image intensity and the calcification concentration. With these considerations model 2 in which the stiffness is linearly related to the image intensity seems the most appropriate model for rupture risk analysis in AAA. Also from a practical point of view this model provides a simple relation for the model input. However, the point spread function may elude the relation between the calcification concentration and the image intensity. Therefore caution is needed when choosing G_c , which might need to be set to a higher value to compensate for the intrinsic blurring.

6.5 Conclusion

We have investigated the local influence of calcified regions in AAA. Our processing of micro-CT images indicates that the calcification geometry as it appears on clinical CTA images is not necessarily realistic, since the image resolution may be inadequate for capturing the complex structure of the calcifications. The computed peak wall stress is sensitive to variations in the material properties of the calcifications. Locally altering material properties on a pre-defined high resolution grid gives similar results as a model with a segmented iso-intensity surface for relatively elastic calcifications only. Also, for lower stiffness ratios, the exact geometry of the calcified region is of minor importance for the peak wall stress in the non-calcified tissue. For rupture risk analysis in AAA it seems best only to focus on the wall stress effects caused by the calcification in the surrounding tissue. We propose that future research should focus on accurately establishing the material properties of the calcified regions and on experimentally assessing the rupture potential of the calcification, the material interface and the surrounding, non-calcified tissue.

Summary and discussion

7.1 Summary

In *chapter 1* an introduction to the pathology and treatment of abdominal aortic aneurysm (AAA) is presented. The main imaging modalities for AAA are discussed and an overview of the automatic segmentation methods for AAA that have been proposed in literature is provided. Also, there is an overview of the evolution in the computational modelling of AAA over the past 25 years which has led to the current, geometrically patient-specific computational models for AAA, which are the central topic in this dissertation.

In *chapter 2* an automatic method for segmentation and dynamic propagation of the AAA lumen and the AAA outer vessel wall with deformable 2-simplex models is presented. This study is based on novel MR protocols for imaging of AAA. The method is validated against multiple manual expert segmentations. Results indicate that the errors in the automatic method are reasonable when the distance from the points on the contours to the 3D surface is used as a performance indicator. Statistical evaluation of performance based on a comparison of the in-slice cross sectional contours of the segmented surface with the manual contours shows that the algorithm is outperformed by the human observers.

The formulation of a computational model for AAA based on the geometries resulting from the automatic segmentation method requires a number of processing steps to come to a computational mesh. In *chapter 3* algorithms that are used for generating thin-walled structures, correcting the curvature of the dual triangulation of the 2-simplex meshes, generating planar regions, and generating and optimising tetrahedral meshes are presented. Every step in the modelling chain has been tested and evaluated. A benchmark comparison with several other mesh generation applications showed that the new application outperforms the existing methods in the majority of cases.

Chapter 4 of this dissertation introduces a backward incremental modelling approach that is used to approximate the diastolic equilibrium wall stress in abdominal aortic aneurysm. This approach leads to a more realistic systolic geometry in the

simulation process. The wall stress results from the backward incremental approach are compared with the stresses that are obtained when the full systolic pressure is directly applied on the measured diastolic geometry. Results indicate that the new, more realistic model leads to higher peak wall stress.

In *Chapter 5* an investigation into the influence of the segmentation accuracy, the variability in the location of the outer wall of the AAA and the modality choice on the computed wall stress in the aneurysm is conducted. The peak wall stress is only reproducible when a sufficiently smooth geometrical model is employed. The 0.99 percentiles of the wall stress distribution, however, show excellent reproducibility. The influence of the user variability in performing manual interaction with the segmentation is higher than the influence of inaccuracies caused by the segmentation uncertainty. This variability appears to be similar on MR and CT. For robust rupture risk prediction based on AAA wall stress it appears best not to include too much geometrical detail, either by using a sufficiently smooth surface representation, or by using a more robust statistical parameter derived from the wall stress distribution in the AAA wall.

Chapter 6 deals with the influence of wall calcifications on the AAA wall stress. The influence of the calcification shape, the modelling approach and the material properties are tested. The results show how the peak wall stress is sensitive to the material properties and the modelling approach. For the peak stress in the non-calcified tissue surrounding the calcification, the exact shape of the calcified area appears to be less important than the precise material properties of the calcifications and the surrounding tissue.

7.2 Possible improvements

The main focus of the research described in this dissertation is the modelling of wall stress in patient-specific models of AAA from MR. A clear limitation of the use of MR is its limited spatial resolution. Once the resolution can be improved, both the slice thickness and the slice distance should be brought down. The slice distance for our particular protocol and application is currently limited to 6 mm only because of hardware limitations of the scanning device. The true minimum slice thickness however, is mainly governed by the signal to noise ratio (SNR). Experiments with slice thicknesses down to 3 mm in this AAA study indicated that the SNR soon becomes too low when the field of view is not adjusted. Scanning at 3.0 Tesla instead of scanning at 1.5 Tesla will, in theory, provide a higher SNR, allowing for thinner slices. It is not clear how this will work out in practice, since higher field strengths may lead to an increase in T_1 , less uniform static MR fields and increased motion and susceptibility artifacts [35]. Still, if a higher resolution can be acquired in the through-slice direction this will lead to less partial volume, and more accurate imaging of the vessel wall. Also, at higher resolution it may very well become possible to segment the bifurcation into the iliac arteries from MR. Apart from higher resolution, the black blood vessel wall images would also

seriously benefit from an improvement of the receiver coil design. The range of the cardiac coil used for the black blood images is too low, resulting in compromised SNR at the image slices near the renal arteries and the iliac bifurcation.

The material properties used in the wall stress simulations presented in this work are fixed. However, the combination of patient-specific blood pressure with the volume variation that may be computed with the propagation technique could be used to assign a patient-specific compliance to the AAA.

The segmentation and propagation method presented in chapter 2 currently only uses the 2D B-TFE images, for which the individual slices are aligned based on the 3D B-TFE images. The 3D images may provide more accurate geometrical information because of the smaller slice distance of 3 mm. However, these images also have a slice overlap of 3 mm and suffer from limited contrast and serious artifacts. The black blood images often provide a clear outer wall feature at the spine, where the feature of the B-TFE images is very limited. However, as mentioned before, the SNR at the upper and lower sections of the imaged volume is very limited. Combination of this information in an intelligent multi-image, multi-feature segmentation algorithm that utilises the several images to obtain combined information may very well lead to an improvement of the segmentation accuracy and robustness.

The mesh generation method for vascular structures presented in chapter 3 could benefit from changes in the deformable surface algorithm. First of all, the current internal force implementation is based on the simplex angle, which is directly computed from the three neighbouring vertices. The deformation process based on the simplex angle favours locally spherical shapes, while vascular structures are often locally shaped like a cylinder. Also, the current implementation leads to a model in which mesh resolution and smoothness constraints cannot easily be controlled separately. An alternative method to compute the internal forces could for instance take into account not only the curvature magnitude, but also the curvature orientation. Also, using more robust curvature estimators such as the normal vector voting approach might lead to a more stable, smoother deformation process.

We used the backward incremental method which is used to estimate the geometry of the unloaded aneurysm from medical images with a material model that is based on a linear relationship between stress and strain, while the true stress-strain curve for AAA material is non-linear. Even though the neo-Hookean model might give a close approximation of the material behaviour in the range from diastolic load to systolic load, this is most likely not the case in the range between the completely unloaded configuration and the diastolic configuration. Using a more realistic stress-strain curve will most likely lead to higher deformations in the backward incremental method with respect to the initial geometry. The effect on the equilibrium stress in the measured geometry, however, is expected to be less, since the stress distribution is mainly dominated by the pressure on the inner vessel wall and the shape of the AAA. The main difficulty for employing a more complex material model is that the higher number of parameters in the more complex material model can only be estimated in-vivo based on the patient-specific compliance. Therefore the first research challenge would be to investigate whether the full set of parameters can

be estimated from observations based on the diastolic and systolic configurations alone.

The main limitations in the sensitivity analysis that has been performed are the limited number of users, the limited number of patients and the sometimes too large time period between the CT and MR acquisitions. These limitations do not affect the validity of the conclusion in this work that the computed wall stress is far more sensitive to the variations in the user input than to the segmentation errors. The next step in this work would be to find a geometry representation that is robust to these kind of variations. However, a study to prove the reproducibility of an even less detailed model would require a much larger number of patients and a larger number of users. Allowing too much detail will cause the peak wall stress to respond to very local variations, resulting in a predictor that is only based on a very small part of the AAA geometry. So, paradoxically, the use of more detailed patient-specific geometrical input may very well lead to a less patient-specific rupture predictor. To overcome this problem, it might be advisable to use a model of the AAA geometry with less freedom. However, using too little detail might affect the discriminatory power of the wall stress as a rupture predictor. For a fine tuning of the robustness and the accuracy of the AAA wall stress models, databases with data from patients who are followed over time until a rupture occurs are a necessity.

In the study on the influence of calcifications only a limited number of calcification shapes were used, and the boundary conditions that were imposed were similar for every shape. It cannot be excluded that imposing more complex loads on the calcification, such as the ones occurring in the AAA, might affect the conclusion that a detailed description of the calcification geometry is not needed. Therefore, the use of more realistic load models would be a clear improvement in this work. Because the current results indicate that for the stress in the non-calcified tissue the shape of the calcification is not of major importance, it may be possible to predict the stress in the healthy parts of the AAA wall without having to include that calcification in the simulation, which means a significant gain in computation time. To do this, it would be necessary to tabulate the stress resulting from the presence of a calcification under various loads. Next, the loads in the AAA wall can be computed from a simulation based on an ideal wall elasticity. Finally, for every calcification, the local loads are estimated and the expected extra stress is read from the pre-defined table. However, for this scenario, it is essential to first obtain good insight in the variations in the stiffness of calcifications in AAA.

7.3 Future prospects

The only true patient-specific influence in the wall stress models of AAA presented in this dissertation is the AAA shape. Other influences that are likely to affect the peak wall stress are the local wall thickness, the material properties and the possible influence of thrombotic sediments. The wall thickness and the material properties cannot yet be accurately determined with medical imaging devices. The correct

model for the influence of thrombus is still controversial. Although the number of patient-specific influences is thus limited, the model may still provide an important indication of the rupture potential of an AAA.

For future research it is important to distinguish between two separate research goals. From an academic point of view, it is worthwhile to try to improve the models with more patient-specific influences and to investigate the effects on the wall stress. This path, which could be characterised by the term *wall stress analysis* will eventually lead to an improved understanding of the important influences for the wall stress and the process leading to the eventual rupture. The topics discussed in chapter 4 and chapter 6 of this thesis fit this description very well. On the other hand, using more patient-specific input will also bring more uncertainty into the model and, since the model becomes more complex, may make the wall stress approximations even more sensitive to errors than is currently the case. From a clinical point of view, this is undesirable, since this compromises the use of the models for *rupture risk prediction*, which is the second major research goal. Even though these two research paths are closely related and will clearly benefit from each other's progress, they must be considered separately. For rupture risk prediction, clinical validation studies are the next big step. Every proposed improvement for wall stress analysis which makes the model more patient-specific and/or physically more accurate must be thoroughly validated clinically before it can be concluded that this extension also leads to an improved rupture risk predictor. There is no apparent reason to assume that the physically most realistic model for AAA wall stress will provide the best clinical model for rupture risk prediction.

As mentioned before, the main issue for wall stress based AAA rupture risk prediction is conducting validation studies. The classical performance measures for segmentation tasks on medical images are based on the distance to golden standard models. These measures are inappropriate for evaluating the computed wall stress in the AAA, as indicated in chapter 5. Since the wall stress itself cannot easily be compared to a golden standard solution for complex domains, the only obvious validation methodology is through statistical evaluation of large groups of patients who are followed over a long period. The main difficulty with these studies is that most patients leave the study once their aneurysm reaches 55 mm. Therefore, validation studies fully rely on rupture incidences of small aneurysms. This means that large numbers of patients will have to participate in a validation study, which almost directly implies that these will have to be multi-centre studies. A large, multi-centre trial leading to a public database is also the only method allowing comparison of the several models of the various research groups and to determine whether newly recognised influences for the wall stress analysis truly add to the clinical value of the model.

Since most patients with AAA leave the validation group once their aneurysm diameter reaches 55 mm, these studies can only show whether the wall stress provides a better rupture risk predictor for small aneurysms. Statistical evaluation of the wall stress as a selection criterion for aneurysms above 55 mm depends on the remaining group of patients who cannot be stented because of various reasons such as

uncommon aneurysm shape or because their weak health does not allow even EVAR. However, it may well be that this group does not provide a good representation of the complete AAA population since the condition of these patients has discriminated them from this population. Therefore, the selection criteria for patients in the group for statistical evaluation of wall stress in aneurysms with a diameter over 55 mm must be given careful thought. In the mean time it seems reasonable to use wall stress analysis in combination with the maximum diameter as a means to identify smaller aneurysms that are likely to rupture.

For wall stress analysis two influences that are very important to bring into the model are the wall thickness and the influence of thrombosis. The main difficulties for wall thickness assessment are that it is difficult to distinguish the vessel wall from the thrombus and that the standard scan planning methods do not allow to scan perpendicular to the vessel wall everywhere in the AAA. The latter problem also hampers accurately scanning quantitative flow images in AAA, especially in the area close to the iliac arteries. Currently, the scan planning on the MR console is fully manual, a situation which prevents the operator to use the MR technique, which can be used to scan in any direction, to its full potential. Implementation of basic image processing techniques on the scanner console could lead to a more automated scan planning, supplying a more versatile imaging modality. With these improvements, more accurate vessel wall scans and quantitative flow images could come within reach. The black blood images that have been acquired could not fulfil their intended function, i.e. local wall thickness assessment. However, these images do provide excellent contrast between several of the constituents of the thrombosis. The varying reports on the influence of thrombus on the AAA wall stress determined experimentally and by modelling could well indicate that the influence of the thrombus needs to be modelled on a patient-specific basis as well. If the material properties of these constituents and the nature of the contact between them are determined, this knowledge could be combined in a patient-specific model for thrombus in AAA.

Bibliography

- [1] MS Atkins and BT Mackiewicz. Fully automatic segmentation of the brain in MRI. *IEEE Transactions on Medical Imaging*, 17:98–107, 1998.
- [2] MA Audette, H Delingette, A Fuchs, Y Koseki, and K Chinzei. A procedure for computing patient-specific anatomical models for finite element-based surgical simulation. In *Seventh Annual Conference of the International Society for Computer Aided Surgery (ISCAS'03)*, 2003.
- [3] RA Baum, JP Carpenter, C Cope, MA Golden, OC Velazquez, DG Neschis, ME Mitchell, CF Barker, and RM Fairman. Aneurysm sac pressure measurements after endovascular repair of abdominal aortic aneurysms. *Journal of Vascular Surgery*, 33:32–41, 2001.
- [4] D Beattie, C Xu, R Vito, S Glagov, and MC Wang. Mechanical analysis of heterogeneous, atherosclerotic human aorta. *Journal of Biomechanical Engineering*, 120:602–607, 1998.
- [5] H Bourouchaki, F Hecht, E Saltel, and PL George. Reasonably efficient delaunay based mesh generator in 3 dimensions. In *Proceedings of the 4th International Meshing Roundtable*, pages 3–14, 1995.
- [6] AW Bradbury, KR Makhdoomi, DJ Adam, JA Murie, A McL Jenkins, and CV Ruckley. Twelve-year experience of the management of ruptured abdominal aortic aneurysm. *British Journal of Surgery*, 84:1705–1707, 1997.
- [7] RL Bush, PH Lin, and AB Lumsden. Endovascular management of abdominal aortic aneurysms. *Journal of Cardiovascular Surgery*, 44:527–534, 2003.
- [8] J Cai, TS Hatsukami, MS Ferguson, R Small, NL Polissar, and C Yuan. Classification of human carotid atherosclerotic lesions with in vivo multicontrast magnetic resonance imaging. *Circulation*, 106:1368–1373, 2002.
- [9] TWG Carrell, KG Burnand, GMA Wells, JM Clements, and A Smith. Stromelysin-1 (matrix metalloproteinase-3) and tissue inhibitor of metalloproteinase-3 are overexpressed in the wall of abdominal aortic aneurysm. *Circulation*, 105:477–482, 2002.
- [10] JR Cebra and R Löhner. From medical images to anatomically accurate finite element grids. *International Journal for Numerical Methods in Engineering*, 51:985–1008, 2001.
- [11] JR Cebra, R Löhner, O Soto, PL Choyke, and PJ Yim. Image-based finite element modeling of hemodynamics in stenosed carotid artery. In *Proceedings of SPIE Medical Imaging*, volume 4683, pages 297–304, 2002.
- [12] JR Cebra, MA Castro, S Appanaboyina, CM Putman, D Millan, and AF Frangi. Ef-

- ficient pipeline for image-based patient-specific analysis of cerebral aneurysm hemodynamics: technique and sensitivity. *IEEE Transactions on Medical Imaging*, 24:457–467, 2005.
- [13] V Chalana and Y Kim. A methodology for evaluation of boundary detection algorithms on medical images. *IEEE Transactions on Medical Imaging*, 16:642–652, 1997.
- [14] SE Clarke, RR Hammond, JR Mitchell, and BK Rutt. Quantitative assessment of carotid plaque composition using multicontrast MRI and registered histology. *Magnetic Resonance in Medicine*, 50:1199–1208, 2003.
- [15] TF Cootes, A Hill, CJ Taylor, and J Haslam. The use of active shape models for locating structures in medical images. *Imaging and Vision Computing*, 12(6):355–366, 1994.
- [16] M de Bruijne. *Model-based segmentation of vascular images*. PhD thesis, Utrecht University, 2003.
- [17] M de Bruijne, B van Ginneken, WJ Niessen, J Maintz, and M Viergever. Active shape model based segmentation of abdominal aortic aneurysms in CTA images. In *Medical Imaging: Image Processing*, volume 4683, pages 463–474, 2002.
- [18] M de Bruijne, B van Ginneken, LW Bartels, M van der Laan, JD Blankensteijn, WJ Niessen, and MA Viergever. Automated segmentation of abdominal aortic aneurysms in multi-spectral MR images. In *Lecture Notes in Computer Science*, volume 2879, pages 538–545, 2003.
- [19] M de Bruijne, B van Ginneken, WJ Niessen, M Loog, and M Viergever. Model-based segmentation of abdominal aortic aneurysms in CTA images. In *Medical Imaging: Image Processing*, volume 5032, pages 1560–1571, 2003.
- [20] M de Bruijne, B van Ginneken, MA Viergever, and WJ Niessen. Adapting active shape models for 3D segmentation of tubular structures in medical images. In *Proceedings of Information Processing in Medical Imaging*, pages 136–147, 2003.
- [21] M de Bruijne, B van Ginneken, MA Viergever, and WJ Niessen. Interactive segmentation of abdominal aortic aneurysms in CTA images. *Medical Image Analysis*, 8:127–138, 2004.
- [22] J de Hart, GWM Peters, PJG Schreurs, and FPT Baaijens. A three-dimensional computational analysis of fluid-structure interaction in the aortic valve. *Journal of Biomechanics*, 36:103–112, 2003.
- [23] S de Putter, M Breeuwer, U Kose, F Laffargue, J-M Rouet, R Hoogeveen, H van de Bosch, J Buth, F van de Vosse, and F Gerritsen. Automatic determination of the dynamic geometry of abdominal aortic aneurysm from MR with application to wall stress simulations. In *Proceedings of the 19th International Computer Assisted Radiology and Surgery conference, Berlin, Germany*, pages 339–344, 2005.
- [24] H Delingette. *Modélisation, Déformation et Reconnaissance d’objets tridimensionnels à l’aide de maillages simples*. PhD thesis, Ecole Centrale de Paris, 1994.
- [25] H Delingette, M Hébert, and K Ikeuchi. Shape representation and image segmentation using deformable surfaces. *Image and Vision Computing*, 10:132–44, 1992.
- [26] ES Di Martino and DA Vorp. Effect of variation in intraluminal thrombus constitutive properties on abdominal aortic aneurysm wall stress. *Annals of Biomedical*

- Engineering*, 31:804–809, 2003.
- [27] ES Di Martino, S Mantero, F Insoi, G Melissano, D Astore, R Chiesa, and R Fumero. Biomechanics of abdominal aortic aneurysm in the presence of endoluminal thrombus: experimental characterisation and structural static computational analysis. *European Journal of Vascular and Endovascular Surgery*, 15:290–299, 1998.
- [28] ES Di Martino, G Guadagni, A Fumero, G Ballerini, R Spirito, P Biglioli, and A Redaelli. Fluid-structure interaction within realistic three-dimensional models of the aneurysmatic aorta as a guidance to assess the risk of rupture of the aneurysm. *Medical Engineering & Physics*, 23:647–655, 2001.
- [29] PB Dobrin. Pathophysiology and pathogenesis of aortic aneurysms. *Surgical Clinics of North America*, 69:687–703, 1989.
- [30] NJB Driessen, CVC Bouten, and FPT Baaijens. Improved prediction of the collagen fiber architecture in the aortic heart valve. *Journal of Biomechanical Engineering*, 127:329–336, 2005.
- [31] NJB Driessen, CVC Bouten, and FPT Baaijens. A structural constitutive model for collagenous cardiovascular tissues incorporating the angular fiber distribution. *Journal of Biomechanical Engineering*, 127:494–503, 2005.
- [32] DF Elger, DM Blacketter, RS Budwig, and KH Johansen. The influence of shape on the stresses in model abdominal aortic aneurysms. *Journal of Biomechanical Engineering*, 118:326–332, 1996.
- [33] L Engellau, EM Larsson, U Albrechtsson, T Jonung, E Ribbe, J Thorne, Z Zdanowski, and L Norgren. Magnetic resonance imaging and MR angiography of endoluminally treated abdominal aortic aneurysms. *European Journal of Vascular and Endovascular Surgery*, 15:212–219, 1998.
- [34] MK Eskandari, JST Yao, WH Pearce, RB Rutherford, FJ Veith, P Harris, VM Bernhard, GJ Becker, MD Morasch, HB Chrisman, RK Ryu, and JS Matsumara. Surveillance after endoluminal repair of abdominal aortic aneurysms. *Cardiovascular Surgery*, 9:469–471, 2001.
- [35] RF Farr and PJ Allisy-Roberts. *Physics for medical imaging*. WB Saunders, 2002.
- [36] M Ferrant, A Nabavi, B Macq, FA Jolesz, R Kikinis, and SK Warfield. Registration of 3-D intraoperative MR images of the brain using a finite-element biomechanical model. *IEEE Transactions on Medical Imaging*, 20:1384–1397, 2001.
- [37] MF Fillinger, ML Raghavan, SP Marra, JL Cronenwett, and FE Kennedy. In vivo analysis of mechanical wall stress and abdominal aortic aneurysm risk. *Journal of Vascular Surgery*, 26:589–597, 2002.
- [38] MF Fillinger, SP Marra, ML Raghavan, and FE Kennedy. Prediction of rupture risk in abdominal aortic aneurysm during observation: Wall stress versus diameter. *Journal of Vascular Surgery*, 37:724–732, 2003.
- [39] L Freitag and P Plassmann. Local optimisation-based simplicial mesh untangling and improvement. *International Journal for Numerical Methods in Engineering*, 49: 109–125, 2000.
- [40] PJ Frey and P-L George. *Mesh generation*. Hermes Science, 2000.
- [41] O Gérard, A Collet Billon, J-M Rouet, M Jacob, M Fradkin, and C Allouche. Efficient model-based quantification of left ventricular function in 3-D echocardiography.

- IEEE Transactions on Medical Imaging*, 21:1059–1068, 2002.
- [42] RM Greenhalgh and the Evar trial participants. Comparison of endovascular aneurysm repair with open repair in patients with abdominal aortic aneurysm (evar trial 1), 30-day operative mortality results: randomised controlled trial. *The Lancet*, 364:843–848, 2004.
- [43] JV Hajnal, DLG Hill, and DJ Hawkes, editors. *Medical Image Registration*. CRC Press, Boca Raton, USA, 2001.
- [44] AJ Hall, EFG Busse, DJ McCarville, and JJ Burgess. Aortic wall tension as a predictive factor for abdominal aortic aneurysm rupture: improving the selection of patients for abdominal aortic aneurysm repair. *Annals of Vascular Surgery*, 14: 152–157, 2000.
- [45] U Hartmann and F Kruggel. A fast algorithm for generating tetrahedral 3D finite element meshes from magnetic resonance tomograms. In *Proceedings of the IEEE Workshop on Medical Image Analysis*, 1998.
- [46] RH Hashemi, WG Bradley, Jr, and CJ Lisanti. *MRI The Basics*. Lippincott Williams & Wilkins, Philadelphia, USA, 2004.
- [47] MS Hassouna, AA Farag, S Hushek, and T Moriarty. Statistical-based approach for extracting 3D blood vessels from TOF-MyRA data. In *Lecture Notes in Computer Science*, volume 2878, pages 680–687, 2003.
- [48] T Hatakeyama, H Shigemats, and T Muto. Risk factors for rupture of abdominal aortic aneurysms based on three-dimensional study. *Journal of Vascular Surgery*, 33: 453–461, 2001.
- [49] A Hilton and J Illingworth. Marching triangles: Delaunay implicit surface triangulation. Technical report, University of Surrey, 1997.
- [50] GA Holzapfel, G Sommer, and P Regitnig. Anisotropic mechanical properties of tissue components in human atherosclerotic plaques. *Journal of Biomechanical Engineering*, 126:657–665, 2004.
- [51] RM Hoogeveen, CJG Bakker, and MA Viergever. Limits to the accuracy of vessel diameter measurement in MR angiography. *Journal of Magnetic Resonance Imaging*, 8:1228–1239, 1998.
- [52] H Huang, R Virmani, H Younis, AP Burke, RD Kamm, and RT Lee. The impact of calcification on the biomechanical stability of atherosclerotic plaques. *Circulation*, 103:1051–1055, 2001.
- [53] F Inzoli, F Boschetti, M Zappa, T Longo, and R Fumero. Biomechanical factors in abdominal aortic aneurysm rupture. *European Journal of Vascular Surgery*, 7: 667–674, 1993.
- [54] J Jago, A Collet-Billon, C Chenal, J-M Jong, and S Makram-Ebeid. XRES: adaptive enhancement of ultrasound images. *Medicamundi*, 46:36–41, 2002.
- [55] KH Johansen. Aneurysms. *Scientific American*, 247:110–125, 1982.
- [56] CD Karkos, U Mukhopadhyay, I Papakostas, J Ghosh, GJ Thomson, and R Hughes. Abdominal aortic aneurysm: the role of clinical examination and opportunistic detection. *European Journal of Vascular and Endovascular Surgery*, 19:299–303, 2000.
- [57] R Klette, HS Stiehl, MA Viergever, and KL Vincken, editors. *Performance Characterisation in Computer Vision*. Kluwer Academic Publishers, Dordrecht, the Nether-

- lands, 2000.
- [58] CM Kramer, LA Cerilli, K Hagspiel, JM DiMaria, FH Epstein, and JA Kern. Magnetic resonance imaging identifies the fibrous cap in atherosclerotic abdominal aortic aneurysm. *Circulation*, 109:1016–1021, 2004.
- [59] B Kritpracha, HG Beebe, and AJ Comerota. Aortic diameter is an insensitive measurement of early aneurysm expansion after endografting. *Journal of Endovascular Therapy*, 11:184–190, 2004.
- [60] H Kurvers, FJ Veith, NJ Gargiulo, EV Lipsitz, T Ohki, NS Cayne, WD Suggs, CH Timaran, GY Kwon, SJ Rhee, and C Santiago. Discontinuous, staccato growth of abdominal aortic aneurysms. *Journal of the American College of Surgeons*, 199:709–715, 2004.
- [61] HM Ladak, JB Thomas, JR Mitchell, BK Rutt, and DA Steinman. A semi-automatic technique for measurement of arterial wall from black blood MRI. *Medical Physics*, 28:1098–1107, 2001.
- [62] RT Lee, FJ Schoen, HM Loree, MW Lark, and P Libby. Circumferential stress and matrix metalloproteinase in human coronary atherosclerosis. *Arteriosclerosis, Thrombosis and Vascular Biology*, 16:1070–1081, 1996.
- [63] Z Li and C Kleinstreuer. A new wall stress equation for aneurysm-rupture prediction. *Annals of Biomedical Engineering*, 33:209–213, 2005.
- [64] Rainald Löhner. Regridding surface triangulations. *Journal of Computational Physics*, 126:1–10, 1996.
- [65] A Long, L Rouet, A Bissery, P Rossignol, D Mouradian, and M Sapoval. Compliance of abdominal aortic aneurysms evaluated by tissue doppler imaging: correlation with aneurysm size. *Journal of Vascular Surgery*, 42:18–26, 2005.
- [66] WE Lorensen and HE Cline. Marching cubes: A high resolution 3D surface construction method. *Computer Graphics*, 21, 1987.
- [67] J Lu, X Zhou, ML Raghavan, W Hou, and W Yang. Prediction of aneurysm stress based on deformed geometry using inverse finite element formulation. In *Proceedings of the summer bioengineering conference, Vail, USA*, 2005.
- [68] D Magee, A Bullpit, and E Berry. Combining 3D deformable models and level set methods for the segmentation of abdominal aortic aneurysms. In *Proceedings of The British Machine Vision Conference*, pages 333–341, 2001.
- [69] SP Marra, DT Chen, MF Fillinger, JM Dwyer, and FE Kennedy. Effects of including calcified deposits in the finite element modeling of an abdominal aortic aneurysm. In *Proceedings of the Summer Bioengineering Conference, Colorado, USA*, 2005.
- [70] A Mohamed and C Davatzikos. Finite element mesh generation and remeshing from segmented medical images. In *Proceedings of the 2004 IEEE International Symposium on Biomedical Imaging*, pages 420–423. IEEE, 2004.
- [71] JA Moore, DA Steinman, and CR Ethier. Computational blood flow modelling: errors associated with reconstructed finite element models. *Journal of Biomechanics*, 31:179–184, 1998.
- [72] JA Moore, BK Rutt, SJ Karlik, K Yin, and CR Ethier. Computational blood flow modelling based on in vivo measurements. *Annals of Biomedical Engineering*, 27:627–640, 1999.

- [73] JA Moore, DA Steinman, DW Holdsworth, and CR Ethier. Accuracy of computational hemodynamics in complex arterial geometries reconstructed from magnetic resonance imaging. *Annals of Biomedical Engineering*, 27:32–41, 1999.
- [74] WR Mower, WJ Quiñones, and SS Gambhir. Effect of intraluminal thrombus on abdominal aortic wall stress. *Journal of Vascular Surgery*, 26:602–608, 1997.
- [75] JG Myers, JA Moore, M Ojha, KW Johnston, and CR Ethier. Factors influencing blood flow patterns in the human right coronary artery. *Annals of Biomedical Engineering*, 29:109–120, 2001.
- [76] TK Nakahashi, K Hoshina, PS Tsao, E Sho, M Sho, JK Karwowski, C Yeh, R-B Yang, JN Topper, and RL Dalman. Flow loading induces macrophage antioxidative gene expression in experimental aneurysms. *Arteriosclerosis, Thrombosis and Vascular Biology*, 22:2017–2029, 2002.
- [77] EL Nickolof and R Riley. Simplified approach for modulation transfer function determination in computed tomography. *Medical Physics*, 12:437–442, 1985.
- [78] WJ Niessen, CJ Bouma, KL Vincken, and MA Viergever. Error metrics for quantitative evaluation of medical image segmentation. In *Performance Characterisation in Computer Vision*, pages 275–284. Kluwer Academic Publishers, 2000.
- [79] SD Olabarriaga, J-M Rouet, M Fradkin, M Breeuwer, and WJ Niessen. Segmentation of thrombus in abdominal aortic aneurysms from CTA with non-parametric statistical grey level appearance modelling. *IEEE Transactions on Medical Imaging*, 24:477–485, 2005.
- [80] S Osher and JA Sethian. Fronts propagating with curvature dependent speed: algorithms based on hamilton-jacobi formulations. *Journal of Computational Physics*, 79:12–49, 1988.
- [81] DL Page, Y Sun, AF Koschan, J Paik, and MA Abidi. Normal vector voting: crease detection and curvature estimation on large noisy meshes. *Graphical Models*, 64:199–229, 2002.
- [82] JC Parodi, JC Palmaz, and HD Barone. Transfemoral intraluminal graft implantation for abdominal aortic aneurysms. *Annals of Vascular Surgery*, 5:491–499, 1991.
- [83] K Perktold, M Hofer, G Rappitsch, M Loew, BD Kuban, and MH Friedman. Validated computation of physiologic flow in a realistic coronary artery branch. *Journal of Biomechanics*, 31:217–228, 1998.
- [84] B Quatember and H Mühlthaler. Generation of CFD meshes from biplane angiograms: an example of image-based mesh generation and simulation. *Applied Numerical Mathematics*, 46:379–397, 2003.
- [85] ML Raghavan, MW Webster, and DA Vorp. Ex vivo biomechanical behavior of abdominal aortic aneurysm: assessment using a new mathematical model. *Annals of Biomedical Engineering*, 24:573–582, 1996.
- [86] ML Raghavan, DA Vorp, MP Federle, MS Makaroun, and MW Webster. Wall stress distribution on three-dimensionally reconstructed models of human abdominal aortic aneurysm. *Journal of Vascular Surgery*, 31:760–769, 2000.
- [87] ML Raghavan, B Ma, FE Kennedy, MF Fillingner, and ES da Silva. Determination of the zero-pressure configuration of cardiovascular structures from in-vivo configuration. In *Proceedings of the second joint EMBS/BMES conference, Houston, USA*,

- pages 1327–1328, 2002.
- [88] S Ranganath. Contour extraction from cardiac MRI studies using snakes. *IEEE Transactions on Medical Imaging*, 14:328–338, 1995.
- [89] RY Rhee, MK Eskandari, AB Zajko, and MS Makaroun. Long-term fate of the aneurysmal sac after endoluminal exclusion of abdominal aortic aneurysms. *Journal of Vascular Surgery*, 32:689–696, 2000.
- [90] PD Richardson. Biomechanics of plaque rupture: progress, problems and new frontiers. *Anal of Biomedical Engineering*, 30:524–536, 2002.
- [91] MS Sacks, DA Vorp, ML Raghavan, MP Federle, and MW Webster. In vivo three-dimensional surface geometry of abdominal aortic aneurysms. *Annals of Biomedical Engineering*, 27:469–479, 1999.
- [92] PM Sanfelippo. Abdominal aortic aneurysm - 2003: what we know, what we dont know - a review. *International Journal of Angiology*, 12:145–152, 2003.
- [93] Scanco Medical. Specifications for the μ ct 80 scanner. "URL: <http://www.scanco.ch/cgi-bin/scanco.pl>", 2005.
- [94] JA Schmidt, CT Johnson, JC Eason, and RS McLeod. *Applications of automatic mesh generation and adaptive methods in computational medicine*. Springer-Verlag, 1994.
- [95] GWH Schurink, J van Baalen, MJT Visser, and J van Bockel. Thrombus within an aortic aneurysm does not reduce pressure on the aneurysmal wall. *Journal of Vascular Surgery*, 31:501–506, 2000.
- [96] E Seveno. Towards an adaptive advancing front method. In *Proceedings of the 6th International Meshing Roundtable*, pages 349–360, 1997.
- [97] JR Shewchuk. Constrained delaunay tetrahedralizations and provably good boundary recovery. In *Proceedings of the 11th International Meshing Roundtable*, pages 193–204, 2002.
- [98] JR Shewchuk. What is a good linear element? interpolation, conditioning, and quality measures. In *Proceedings of the 11th International Meshing Roundtable*, pages 15–18, 2002.
- [99] K Singh, KH Bonnaa, BK Jacobsen, L Bjork, and S Solberg. Prevalence of and risk factors for abdominal aortic aneurysms in a population-based study: the tromsø study. *American Journal of Epidemiology*, 154:236–244, 2001.
- [100] L Speelman, A Bohra, MS Makaroun, and DA Vorp. Assessment of wall calcification in patient-specific finite element analyses of abdominal aortic aneurysm. In *Proceedings of the Summer Bioengineering Conference, Colorado, USA*, 2005.
- [101] DA Steinman, JB Thomas, HM Ladak, JS Milner, BK Rutt, and JD Spence. Reconstruction of carotid bifurcation hemodynamics and wall thickness using computational fluid dynamics and MRI. *Magnetic Resonance in Medicine*, 47:149–159, 2002.
- [102] DA Steinman, JS Milner, CJ Norley, SP Lownie, and DW Holdsworth. Image-based computational simulation of flow dynamics in a giant intracranial aneurysm. *American Journal of Neuroradiology*, 24:559–566, 2003.
- [103] DA Steinman, DA Vorp, and CR Ethier. Computational modeling of arterial biomechanics: Insights into pathogenesis and treatment of vascular disease. *Journal of*

- Vascular Surgery*, 37:1118–1128, 2003.
- [104] M Subasic, S Loncaric, and E Sorantin. 3-D image analysis of abdominal aortic aneurysm. In *Proceedings of SPIE Medical Imaging - Image Processing*, pages 1681–1689, 2002.
- [105] JM Sullivan, G Charron, and KD Paulsen. A three-dimensional mesh generator for arbitrary multiple material domains. *Finite Elements in Analysis and Design*, 25: 219–241, 1997.
- [106] G Taubin. Estimating the tensor of curvature of a surface from a polyhedral approximation. In *Proceedings of the Fifth International Conference on Computer Vision*, pages 902–907, 1995.
- [107] H Thiele, E Nagel, I Paetsch, B Schnackenburg, A Bornstedt, M Kouwenhoven, A Wahl, G Schuler, and E Fleck. Functional cardiac MR imaging with steady-state free precession (SSFP) significantly improves endocardial border delineation without contrast agents. *Journal of Magnetic Resonance Imaging*, 14:362–367, 2001.
- [108] JB Thomas, JS Milner, BK Rutt, and DA Steinman. Reproducibility of image-based computational fluid dynamics models of the human carotid bifurcation. *Annals of Biomedical Engineering*, 31:132–141, 2003.
- [109] JA Thorpe. *Elementary topics in differential geometry*. Springer-Verlag, 1979.
- [110] MJ Thubrikar, J Al-Soudi, and F Robicsek. Wall stress studies of abdominal aortic aneurysm in a clinical model. *Annals of Vascular Surgery*, 15:355–366, 2001.
- [111] MJ Thubrikar, M Labrosse, F Robicsek, J Al-Soudi, and B Fowler. Mechanical properties of abdominal aortic aneurysm wall. *Journal of Medical Engineering and Physics*, 25:133–142, 2001.
- [112] MJ Thubrikar, F Robicsek, M Labrosse, V Chervenkov, and BL Fowler. Effect of thrombus on abdominal aortic aneurysm wall dilation and stress. *Journal of Cardiovascular Surgery*, 44:67–77, 2003.
- [113] J Tohka. Surface smoothing based on a sphere shape model. In *Proceedings of the 6th Nordic Signal Processing Symposium - NORSIG 2004*, pages 17–20, 2004.
- [114] D Ulrich, B van Rietbergen, H Weinans, and P Rügsegger. Finite element analysis of trabecular bone structure: a comparison of image-based meshing techniques. *Journal of Biomechanics*, 31:1187–1192, 1998.
- [115] FN van de Vosse, J de Hart, CHGA van Oijen, D Bessems, TWM Gunther, A Segal, BJBW Wolters, JMA Stijnen, and FPT Baaijens. Finite-element-based computational methods for cardiovascular fluid-structure interaction. *Journal of Engineering Mathematics*, 47:335–368, 2003.
- [116] JA van der Vliet and APM Boll. Abdominal aortic aneurysm. *The Lancet*, 349: 863–866, 1997.
- [117] HA van der Vorst. Bi-CGSTAB: A fast and smoothly converging variant of Bi-CG for the solution of nonsymmetric linear systems. *SIAM Journal on Scientific and Statistical Computing*, 13:631–644, 1992.
- [118] C van Oijen. *Mechanics and design of fiber reinforced vascular prostheses*. PhD thesis, Technische Universiteit Eindhoven, 2003.
- [119] JP Vande Geest, MS Sacks, and DA Vorp. The effects of aneurysm on the biaxial mechanical behavior of human abdominal aorta. *Journal of Biomechanics*, In Press,

- 2005.
- [120] AK Venkatasubramiam, MJ Fagan, T Mehta, KJ Mylankal, B Ray, G Kuhan, IC Chetter, and PT McCollum. A comparative study of aortic wall stress using finite element analysis for ruptured and non-ruptured abdominal aortic aneurysms. *European Journal of Vascular and Endovascular Surgery*, 28:168–174, 2004.
 - [121] RP Vito and SA Dixon. Blood vessel constitutive models - 1995-2002. *Annual Review of Biomedical Engineering*, 5:413–439, 2003.
 - [122] A Vlachos, J Peters, C Boyd, and J Mitchell. Curved PN triangles. In *Proceedings of the ACM Symposium on Interactive 3D Graphics*, pages 159–166, 2001.
 - [123] DA Vorp, ML Raghavan, and MW Webster. Mechanical wall stress in abdominal aortic aneurysm: influence of diameter and asymmetry. *Journal of Vascular Surgery*, 27:632–639, 1998.
 - [124] DA Vorp, DHJ Wang, MW Webster, and WJ Federspiel. Effect of intraluminal thrombus thickness and bulge diameter on the oxygen diffusion in abdominal aortic aneurysm. *Journal of Biomechanical Engineering*, 120:579 – 583, 1998.
 - [125] DHJ Wang, MS Makaroun, MW Webster, and DA Vorp. Effect of intraluminal thrombus on wall stress in patient-specific models of abdominal aortic aneurysm. *Journal of Vascular Surgery*, 36:598–604, 2002.
 - [126] JJ Wever, JD Blankensteijn, JC van Rijn, IAMJ Broeders, BC Eikelboom, and WP Mali. Inter- and intraobserver variability of CT measurements obtained after endovascular repair of abdominal aortic aneurysms. *American Journal of Roentgenology*, 175:1279–1282, 2000.
 - [127] SC Whitaker. Imaging of abdominal aortic aneurysm before and after endoluminal stent-graft repair. *European Journal of Radiology*, 39:3–15, 2001.
 - [128] GW Williams. Comparing the joint agreement of several raters with another rater. *Biometrics*, 32:619–627, 1976.
 - [129] SD Williamson, Y Lam, HF Younis, H Huang, S Patel, MR Kaazempur-Mofrad, and RD Kamm. On the sensitivity of wall stresses in diseased arteries to variable material properties. *Journal of Biomechanical Engineering*, 125:147–155, 2003.
 - [130] O Wink, AF Frangi, B Verdonck, MA Viergever, and WJ Niessen. 3D MRA coronary axis determination using a minimum cost path approach. *Magnetic Resonance in Medicine*, 47:1169–1175, 2002.
 - [131] YG Wolf, BB Hill, GD Rubin, TJ Fogarty, and CK Zarins. Rate of change in abdominal aortic aneurysm diameter after endovascular repair. *Journal of Vascular Surgery*, 32:108 –115, 2000.
 - [132] BJBW Wolters, MCM Rutten, GWH Schurink, U Kose, J de Hart, and FN van de Vosse. Towards model-based rupture risk assesment of abdominal aortic aneurysms. *Medical Engineering & Physics*, 27:871–883, 2005.
 - [133] C Yuan, WS Kerwin, MS Ferguson, N Polissar, S Zhang, J Cai, and TS Hatsukami. Carotid atherosclerotic plaque: noninvasive MR characterisation and identification of vulnerable lesions. *Radiology*, 221:285–299, 2001.

Samenvatting

Een *abdominaal aorta aneurysma* (AAA) is een pathologische verwijding van de aorta ter hoogte van de onderbuik. AAA's ontstaan met name bij oudere mannen en zijn hoogstwaarschijnlijk gerelateerd aan arteriosclerose. Als een AAA scheurt is de overlevingskans voor de patiënt zeer klein. Om scheuring te voorkomen kan er een *stent-graft*, een soort prothese voor de aorta, geplaatst worden. Deze ingreep wordt meestal uitgevoerd met behulp van een kleine incisie ter hoogte van de lies. De stent-graft wordt door deze incisie met behulp van een geleidingsdraad via het vatenstelsel naar de aorta geleid en geplaatst. Het plaatsen van een stent-graft is een risicovolle operatie en bij een niet te verwaarlozen deel van de behandelde patiënten treden na de plaatsing gevaarlijke complicaties op. Om deze redenen is het van groot belang om een goede selectie te kunnen maken van patiënten die in aanmerking komen voor deze ingreep.

De huidige praktijk is dat patiënten worden geselecteerd op basis van de diameter van het aneurysma. Op het moment dat het aneurysma zover gegroeid is dat de diameter meer is dan 55 mm wordt tot behandeling overgegaan. Ofschoon de scheuringskans tot op zekere hoogte wel gerelateerd is aan het formaat van het aneurysma gebeurt het ook dat kleine aneurysmata scheuren en zijn er gevallen bekend van zeer grote aneurysmata die niet scheuren. Een nieuwe methode om tot een betere selectie van patiënten te komen is het bepalen van de wandspanning in het aneurysma met behulp van eindige elementen modellen. Het ultieme doel van het onderzoek naar wandspanning in AAA's is om met volautomatische methoden tot een robuuste, nauwkeurige schatting van het patiëntspecifieke ruptuurrisico te komen. Voor de exacte waarde van de maximale spanning zijn de patiëntspecifieke vorm van het aneurysma, de bloeddruk, de invloed van trombus en de materiaaleigenschappen van groot belang. De doelstellingen van het onderzoek dat beschreven wordt in dit proefschrift zijn om op basis van magnetische resonantie beelden een model van de specifieke vorm van het aneurysma te genereren en vervolgens een benadering te maken van de wandspanning. Tevens zijn we geïnteresseerd in de gevoeligheden van dit model.

Hoofdstuk 1 geeft een overzicht van de risicofactoren die een rol spelen voor het ontstaan van AAA's, alsmede een overzicht van de behandelingsmethoden. Verder wordt er een kort overzicht gepresenteerd van de beschikbare literatuur over het reconstrueren van de AAA geometrie op basis van medische beelden en het uitvoeren van wandspanningsanalyses in AAA's.

In *Hoofdstuk 2* wordt beschreven hoe we met behulp van nieuwe MR acquisitie protocollen een reconstructie hebben gemaakt van de patiëntspecifieke vorm van het aneurysma. De variatie tussen de drie-dimensionale geometrieën van de aneurysmata bij verschillende patiënten is dermate groot dat het lastig is om met globale aannamen over de geometrie tot een nauwkeurige geometrische beschrijving te komen. Om deze reden is de methode gebaseerd op 3D *deformable models* die een discrete beschrijving vormen van een oppervlak dat op basis van beeldinformatie en lokale vormcriteria iteratief vervormd kan worden tot het een benadering geeft van de vorm van het aneurysma. Tevens hebben we een methode ontwikkeld om met behulp van een optimalisatie van de correlatie van lokale beeldinformatie op opeenvolgende fasen binnen de hartcyclus de initiële vorm te deformeren om een dynamische beschrijving van de geometrie van het bloedvat te verkrijgen. De methodes zijn gevalideerd door de resultaten te vergelijken met 2D contouren die getekend zijn door een aantal gebruikers. Ofschoon de fouten in de automatisch gereconstrueerde vorm acceptabel zijn, presteren de gebruikers in vrijwel alle gevallen beter dan de algoritme.

Hoofdstuk 3 beschrijft de methoden die gebruikt zijn om op automatische wijze van de initiële beschrijving van de geometrie te komen tot een beschrijving die gebruikt kan worden voor eindige elementen simulaties. Hierin zijn belangrijke verbeteringen verwezenlijkt ten opzichte van de nauwkeurigheid van bestaande methoden. Ofschoon de methoden die in dit hoofdstuk beschreven worden in dit onderzoek voornamelijk gebruikt worden voor wandspanningssimulaties in AAA's, zijn ze ook direct toe te passen op andere al dan niet pathologische vaatstructuren in het lichaam. Dit laatste wordt geïllustreerd aan de hand van een voorbeeld van bloedstroming in een cerebraal aneurysma.

De bestaande methode om de wandspanning in een AAA te berekenen gaat uit van de aanname dat de vorm zoals die gemeten wordt tijdens de diastolische fase spanningsvrij is. Deze aanname is in de praktijk niet houdbaar aangezien er tijdens elke fase van de hartcyclus sprake is van een drukval over de wand van het aneurysma. In *Hoofdstuk 4* presenteren we een methode waarmee de voorspanning zoals die heerst in het aneurysma zoals het op de dynamische MR beelden zichtbaar is benaderd kan worden. Op deze wijze komen we tot een meer realistische benadering van de verplaatsingen en de spanningen in de aneurysma wand. De resultaten wijzen uit dat de piekspanning in de AAA's hoger is dan tot dusverre werd aangenomen.

In *Hoofdstuk 5* wordt de gevoeligheid van de berekende wandspanningen voor geometrische fouten onderzocht. Allereerst tonen we aan dat de maximale wandspanning alleen reproduceerbaar is als we een voldoende glad model voor het aneurysma gebruiken. Uit experimenten gebaseerd op verschillende manuele segmentaties van een aantal gebruikers op MR blijkt dat de wandspanning in het aneurysma zeer gevoelig is voor kleine variaties met betrekking tot de precieze vorm. Een vergelijkbare studie met behulp van CT beelden voor dezelfde patiënten laat zien dat deze onzekerheid ook aanwezig is voor deze modaliteit. De resultaten wijzen verder uit dat het voor ruptuurvoorspellingen wellicht beter is om zeer lokale effecten te verwaarlozen, hetzij door een niet al te gedetailleerd model te veronderstellen voor de

vorm, of door een statistische afgeleide van de wandspanningsverdeling te gebruiken in plaats van het absolute maximum.

In *Hoofdstuk 6* wordt de invloed van calcificaties in de wand van het aneurysma nader bekeken. Het is in de bestaande literatuur gesuggereerd dat calcificaties kunnen leiden tot hogere wandspanningen hetgeen aanleiding zou kunnen geven tot een hoger ruptuurrisico. De gehanteerde modellen en de aannamen voor de materiaaleigenschappen in de voorgaande studies zijn echter zeer verschillend, evenals de waargenomen fenomenen. Verder wordt in deze voorgaande studies de precieze vorm van de calcificaties buiten beschouwing gelaten. In onze simulaties gebruiken we juist een gedetailleerd model voor de calcificaties en laten we de vorm van de AAA buiten beschouwing. Door de resultaten van een aantal modelleringsmethoden onderling te vergelijken voor verschillende aannamen voor de materiaaleigenschappen laten we zien dat de spanning sterk afhangt van de materiaaleigenschappen van de calcificaties. Tevens laten we zien dat de spanningen in de calcificaties en op de overgang van de materialen nauwelijks nauwkeurig te benaderen zijn met de huidige scan-methoden en kennis over de materiaalhechting. Het lijkt dan ook het beste om vooralsnog met name de veranderde spanning in het niet gecalcificeerde deel van het weefsel te beschouwen onder invloed van de calcificaties. Deze laatste grootheid blijkt slechts in zeer beperkte mate gerelateerd te zijn aan de vorm van de calcificaties, en in veel grotere mate aan de materiaaleigenschappen.

Dankwoord

Het onderzoek dat in dit proefschrift wordt beschreven bestrijkt alle stadia van het modelleringsproces voor wandspanning in abdominale aorta aneurysmata, van beeldacquisitie via beeldsegmentatie tot het mechanische model en de evaluatie van de uiteindelijke numerieke simulaties. De voornaamste reden dat dit alles tot een goed einde is gekomen is dat ik bij al deze aspecten van het onderzoek hulp heb gekregen.

Allereerst wil ik mijn promotoren Frans Gerritsen en Frans van de Vosse en mijn co-promotor Marcel Breeuwer bedanken voor de ondersteuning die ze mij gedurende de afgelopen drie jaar hebben geboden. Ook wil ik hen bedanken voor het vertrouwen dat ze in mij hebben gehad, zelfs op de momenten dat ik er zelf wellicht iets minder sterk in geloofde.

Van mijn collega's bij de TU/e wil ik iedereen uit de CIPP groep bedanken omdat ze mijn presentaties over onderwerpen die soms wellicht iets te ver van hun bed stonden welwillend hebben doorstaan. Van de AIO's uit het Hemodyn project wil ik Berent Wolters en Tijmen Gunther bedanken voor de prettige samenwerking en David Bessems en Raoul van Loon voor de discussies en de ondersteuning met SEPRAN die vooral in het begin broodnodig was. Evelyne van Dam wil ik bedanken voor de micro-CT beelden van de wand calcificaties en de maanlandschappen uit de elektronenmicroscop die ze heeft gefabriceerd en beschikbaar heeft gesteld voor gebruik in dit onderzoek.

Bij de afdeling Healthcare IT - Advanced Development bij Philips Medical Systems wil ik iedereen bedanken voor de aangename tijd die ik hier heb doorgebracht. Met name wil ik Ursula Kose bedanken voor de samenwerking en Kees Visser voor de ondersteuning bij het gebruik van EasyScil. Bij het aanleren van C++ en Ruby was de hulp van Rutger Nijlunsing onontbeerlijk. Hoewel de wijze lessen me geregeld boven de pet gingen, heb ik dankzij zijn abstracte benadering vrij snel in de gaten gekregen dat programmeren wel leuk is, zelfs voor wiskundigen. Met behulp van Rutger's geïmproviseerde compute server heb ik mijn rekencapaciteit in de laatste drie maanden voldoende ver kunnen opschroeven om de tientallen simulaties voor hoofdstuk 5 op tijd af te kunnen krijgen. Verder wil ik Romhild Hoogeveen van de Philips Medical Systems afdeling MR Clinical Science bedanken voor zijn inspanningen bij het ontwikkelen van de specifieke MR protocollen waarmee de data voor hoofdstuk 2 is verkregen.

Bij het Catharina Ziekenhuis in Eindhoven wil ik allereerst Harrie van den Bosch bedanken voor zijn grote enthousiasme en de uiterst soepele samenwerking. Verder wil ik Jaap Buth bedanken voor het selecteren van patiënten die in aanmerking kwamen voor het Hemodyn onderzoek. Ook wil ik de scanning operators van het MR lab bedanken voor hun inspanningen bij de acquisitie van de MR data die in dit proefschrift wordt gebruikt. Ofschoon waarschijnlijk geen van hen dit boekje ooit onder ogen zal krijgen, wil ik zeker ook alle patiënten bedanken die speciaal voor het Hemodyn onderzoek naar het ziekenhuis zijn gekomen en soms meer dan een uur lang ongemakken hebben doorstaan in de MR scanner.

Je souhaite remercier Franck Laffargue de Medisys, Philips Medical Systems, qui, depuis Paris et pour mon plus grand plaisir, a contribué notablement à la réalisation de cette dissertation. Je remercie également Maxim Fradkin et Jean-Michel Rouet pour leur assistance concernant l'application 3DAO, et pour leurs développements d'extensions spécifiques à ce projet.

Verder wil ik mijn twee afstudeerders, Ellen van Nunen en Richard Vogelaars bedanken voor hun bijdragen aan dit werk. Ellen, ofschoon je waarschijnlijk geen sporen van jouw werk zult terug vinden in dit boekje, hebben je resultaten zeker bijgedragen aan de begripsvorming en dus ook aan het verloop van dit onderzoek. Richard, onze werkzaamheden aan multi-spectrale segmentatie van AAA van MR hadden absoluut goed in dit proefschrift gepast, maar helaas ligt jouw deadline iets later dan de mijne. Ik wens je veel succes met het afronden van je studie en met je verdere carrière.

Buiten de professionele kring wil ik ook mijn vrienden en familie bedanken voor hun steun in de afgelopen drie jaren. Mijn zus Marjan voor haar vermogen om elke tegenslag tot in het oneindige te relativiseren. Fouke en Berent omdat ze me als paranimf zullen bijstaan tijdens de promotie zelf. Mijn vader, die me heeft geïnspireerd om een exacte richting te kiezen en die de enige was buiten de werkkring met wie ik inhoudelijk over mijn werk heb kunnen praten. Ik weet zeker dat ik niet de enige zal zijn die zijn aanwezigheid zal missen bij de verdediging.

Tot slot wil ik Lesley bedanken voor haar uitmuntende planning die er toe heeft geleid dat onze aanstaande gezinsuitbreiding hoogstwaarschijnlijk pas net na de verdediging zal plaatsvinden. Bovenal wil ik haar echter bedanken voor het feit ze het met me heeft weten uit te houden de afgelopen drie jaar en voor de onvoorwaardelijke steun die ik al die tijd van haar heb gekregen.

Curriculum vitae

Sander de Putter was born on the 23rd of June, 1977 in Velden, The Netherlands. He obtained his MSc-degree in mathematics at Utrecht University in August 2000. His MSc-thesis, entitled "On shift selection for harmonic Ritz pairs from a restarted Lanczos process" dealt with optimal restart vector selection for solving large systems of linear equations. After a period of travelling, he was accepted into the post-graduate programme Mathematics for Industry at the Stan Ackermans Institute in Eindhoven in January 2001. In spring 2002, he stayed as a guest at the department of mathematical science at Durham university for a few months working on models for penetrative convection in porous media. The final project of the Stan Ackermans programme was performed at the X-ray Pre-Development department at Philips Medical Systems in Best and focussed on hemodynamics in brain aneurysms. After concluding this work, he started his PhD-studies at the Technische Universiteit Eindhoven in close cooperation with the Advanced Development group of the Healthcare IT department of Philips Medical Systems in Best in January 2003.

Publications

- S de Putter, F Laffargue, M Breeuwer, FN van de Vosse, and FA Gerritsen. Computational mesh generation for vascular structures with deformable surfaces. Accepted for publication in International Journal of Computer Assisted Radiology and Surgery, 2006.
- S de Putter, M Breeuwer, U Kose, J-M Rouet, R Hoogeveen, H van den Bosch, J Buth, FN van de Vosse, and FA Gerritsen. Automatic segmentation and tracking of abdominal aortic aneurysm from MR with 3D active objects. Submitted to Medical Image Analysis, 2006.
- S de Putter, BJBW Wolters, MCM Rutten, M Breeuwer, FA Gerritsen, and FN van de Vosse. Initial wall stress in patient-specific abdominal aortic aneurysms with a backward incremental method. Under review at Journal of Biomechanics, 2006.
- S de Putter, M Breeuwer, FN van de Vosse, U Kose, and FA Gerritsen. Patient-specific models of wall stress in abdominal aortic aneurysm - a comparison between

- MR and CT. Accepted for publication in Proceedings of SPIE Medical Imaging - Image Processing, San Diego, USA, 2006.
- S de Putter, FN van de Vosse, M Breeuwer, and FA Gerritsen. Local influence of calcifications on the wall mechanics of abdominal aortic aneurysm. Accepted for publication in Proceedings of SPIE Medical Imaging - Image Processing, San Diego, USA, 2006.
 - S de Putter, M Breeuwer, U Kose, F Laffargue, J-M Rouet, R Hoogeveen, H van de Bosch, J Buth, F van de Vosse, and F Gerritsen. Automatic determination of the dynamic geometry of abdominal aortic aneurysm from MR with application to wall stress simulations. In *Proceedings of the 19th International Computer Assisted Radiology and Surgery conference, Berlin, Germany*, pages 339–344, 2005.
 - S de Putter, M Breeuwer, and F Laffargue. High quality accurate surface triangulations from a simplex mesh. European patent application PHNL041437EPP, Dec 17 2004.
 - S de Putter, M Breeuwer, and M Quist. System and method for registration of medical images. European patent application PHNL041248EPP, Nov 10 2004.
 - U Kose, S de Putter, R Hoogeveen, and M Breeuwer. CFD of abdominal aortic aneurysms with patient-specific inflow boundary conditions. Accepted for publication in Proceedings of SPIE Medical Imaging - Image Processing, San Diego, USA, 2006.
 - M Breeuwer, U Götte, K Visser, FA Gerritsen, R Hoogeveen, B Wolters, S de Putter, T Gunther, FN van de Vosse, H van de Bosch, and J Buth. Patient-specific hemodynamic modeling of abdominal aortic aneurysms. In *Proceedings of the Congress of the European Society of Biomechanics (ESB2004), 's-Hertogenbosch, The Netherlands*, 2004.
 - M Breeuwer, U Götte, R Hoogeveen, BJBW Wolters, S de Putter, H van de Bosch, J Buth, J-M Rouet, and F Laffargue. Assessment of the rupture risk of abdominal aortic aneurysms by patient-specific hemodynamic modeling - initial results. In *Proceedings of the 18th international Computer Assisted Radiology and Surgery conference, Chicago, USA*, pages 1090–1095, 2004.
 - M Breeuwer, U Götte, K Visser, R Hoogeveen, F Laffargue, J-M Rouet, BJBW Wolters, and S de Putter. Assessment of the rupture risk of abdominal aortic aneurysms by patient-specific hemodynamic modeling - initial results. Proceedings ISMRM, Kyoto, Japan (abstract), 2004.
 - M Carr and S de Putter. Penetrative convection in a horizontally isotropic porous layer. *Continuum Mechanics and Thermodynamics*, 15:3–43, 2003.
 - S de Putter. Simulating blood flow in cerebral saccular aneurysms. Final report Stan Ackermans institute, Eindhoven, ISBN 90-444-0269-2, 2002.

